Coherent EUV Light from High-Order Harmonic Generation: Enhancement and Applications to Lensless Diffractive Imaging

by

Ariel J. Paul

B.A., University of Pennsylvania, 1999

A thesis submitted to the

Faculty of the Graduate School of the

University of Colorado in partial fulfillment

of the requirements for the degree of

Doctor of Philosophy

Department of Physics

2007

This thesis entitled:
Coherent EUV Light from High-Order Harmonic Generation: Enhancement and Applications to Lensless Diffractive Imaging
written by Ariel J. Paul
has been approved for the Department of Physics

Prof. Henry C. Kapteyn

Prof. Margaret M. Murnane

Date

The final copy of this thesis has been examined by the signatories, and we find that both the content and the form meet acceptable presentation standards of scholarly work in the above mentioned discipline.

Paul, Ariel J. (Ph.D., Physics)

Coherent EUV Light from High-Order Harmonic Generation: Enhancement and Applications to Lensless Diffractive Imaging

Thesis directed by Profs. Henry C. Kapteyn and Margaret M. Murnane

The first half of this thesis presents the first demonstration of quasi-phase matching in the coherent high-order harmonic conversion of ultrafast laser pulses into the EUV region of the spectrum. To achieve this quasi-phase matching, a novel method of fabricating hollow waveguides with a modulated inner diameter was developed. This technique lead to significant enhancements of EUV flux at wavelengths shorter than were previously accessible by known phase-matching techniques. In the second half of this thesis, the first tabletop demonstration of lensless diffractive imaging with EUV light is presented using HHG in a gas-filled hollow waveguide to provide coherent illumination. This tabletop microscope shows a spatial resolution of ~ 200 nm and a large depth of field. Furthermore, the technique is easily scalable to shorter wavelengths of interest to biological imaging.

Dedication

To my grandmother Josepha Ligon

Acknowledgements

Foremost, my family, especially my parents, Philip & Genia Paul, for the knowledge and support to pursue a successful graduate career. Profs. Margaret Murnane and Henry Kapteyn for my unique research path. Pre-CU: Jeff Klein (amazing mentor), Kane Bros., Dave Weitz, UPPSMS, Darin Rhodes, Brad Baker, Jen Close, NOAA coworkers. Early: Charles Bailey, Tim Black, Joe Britton, Kevin Holman, Dustin Hoover, Chris Kelso, Jason Schmidt, James Walker. TA: amazing students, Jerry Leigh, Mike Dubson, John Cumalat, Tom DeGrand. Early work: Randy Bartels, Sterling Backus, Emily Gibson. Instrument Shop: Dave Alchenburger, Todd Asnicar, Leslie Czia, Hans Green (awesome friend/teacher), Kim Hagen, Blaine Horner, Andy Hytjan, Tracy Keep, Alan Pattee, Lee Thornhill, Seth Weiman. Support staff: Sam Jarvis, Pam Leland, Rachel Tearle, Lisa Roos, the supply office, electronics shop. Lab: Luis Miaja-Avilla, Oren Cohen, Etienne Gagnon, David Gaudiosi, Erez Gershgoren, Mike Grisham, Steffen Haedrich, Jim Holtsnider, Nathan Lemke, Amy Lytle, Daisy Raymondson, Richard Sandberg, Guido Sartoff, Arvinder Sandhu, Ra'anan Tobey, Adrienne Van Allen, Nick Wagner, Andrea Wuest, all K/M group past & present. Jilans: Ashley Carter, Manuel Castellanos, Konrad Lehnert, Brandon Smith, Oliver Monti, Mark Notcutt. Boulder High & tutoring students. Other Friends: Mike Alessi, Kathe Baker, Jessica Bedwell (lv/sp), Adrienne Bentley, Corey Dickerson, Craig Emrich, Aaron Fortner, Halston Hoverstein, Amy Johnson, Heidi Metzler, Mark Morlino, Dione Rossiter, Michael Urban. Companions: Dixie, Macie, Dani, George, Zoey, Lilly.

Contents

Chapter

Figures

Figure

Chapter 1

Introduction

My graduate career has been somewhat unique in the types of problems to which I have devoted much of my time and effort. The problems on which I have thrived the most have required hands-on mechanical answers that were motivated and solved through an understanding of the underlying physics. Additionally, whereas students are generally most concerned with experimental difficulties that affect their individual experiments, I took great pleasure in developing elegant solutions to several experimental issues faced regularly in our research. Of course, the somewhat unique nature of the Kapteyn/Murnane group, with many students making use of similar technologies and sharing equipment, allowed me these opportunities, and meant that such solutions quickly benefited many experiments. My advisors allowed me a tremendous amount of autonomy and freedom to pursue several of these types of projects, and the results have been some of the more rewarding moments of my research.

Most of the results presented in this thesis appear (or will appear) in the scientific literature. So, I have made a special effort to include not only experimental results, but also technical details that will help a student continue the work to which I have contributed. In particular, I have included detailed sections describing the process of making modulated waveguides, the construction and benefits of a v-groove fixturing system for hollow waveguides, the development of light-tight fixtures for holding EUV filters, as well as alignment and data acquisition details for our lensless diffractive imag-

ing experiments. Whenever appropriate, I have used a 'conversational' approach. This approach allows me to interweave some of my personality with the scientific discussion, as well as giving the reader information on the scientific *process* I used to obtain the result, in addition to the result itself.

In Chapter 2, I present a basic introduction to high harmonic generation (HHG) and discuss the relevance of phase matching to nonlinear optical frequency conversion. The low-order process of second harmonic generation is used to motivate the fundamental theory of phase matching, and then the method of pressured-tuned phase matching of HHG in a gas-filled hollow-waveguide is explored. This chapter concludes with a description of the original 3-section hollow waveguide fixture used by our group to phase match HHG.

Chapter 3 describes the world's first demonstration of quasi-phase matching (QPM) in the realm of extreme nonlinear optics using periodically-modulated hollow gas-filled waveguides [1]. In a similar fashion to my approach towards discussing traditional phase matching, I begin with a treatment of QPM in the context of second harmonic generation. The implications of QPM are extended to the process of HHG, and I explain the motivations for attempting to fabricate waveguides with a periodically modulated inner diameter. After discussing the demonstration of QPM in such waveguides, I present an in-depth account of the glass-blowing process used to fabricate the modulated waveguides, as well as of the manner in which this process evolved.

Since I exerted a significant portion of my research efforts to improving the use of hollow waveguides, Chapter 4 is devoted to a discussion of these waveguides. The basic issues of coupling and losses for a hollow waveguide are treated, after which I delve into the details of modifying the 3-section design and the development of a specialized v-groove fixturing system. A simple optical set-up for accurately comparing the transmission characteristics for different hollow waveguide arrangements is also shown. My work on hollow waveguides, which improved the consistency and modes of the coherent

extreme ultraviolet light (EUV) we produce through HHG, ties together my early work with the coherent imaging work presented after this chapter.

Chapter 5 introduces the topic of coherent imaging in the extreme ultraviolet (EUV) region of the spectrum and details some of the unique aspects of imaging at this wavelength range as compared to the visible end of the spectrum. I briefly review the idea of coherence and its relevance to imaging, after which I present some of the common methods of imaging in the EUV. The background of the relatively new method of lensless diffractive imaging, which we chose to attempt with our EUV source, is detailed. This imaging method replaces traditional optics with a computerized algorithm that retrieves phase information from a measured diffraction pattern subject to constraints. Although we do not perform the phase retrieval ourselves, understanding the theory of this process is highly relevant to grasping the experimental requirements for successful lensless imaging. To conclude the chapter, I enumerate and clarify these various experimental requirements.

The experimental details and results from the world's first demonstration of lensless diffractive imaging with a tabletop high harmonic source are presented in Chapter 6. The suitability of this technique for our unique EUV source is made clear, and its advantages are explored. I also describe in detail the experimental geometry and its components, as well as the improvements that were made to produce success of the imaging technique. The imaging results definitively show that we have built and demonstrated a tabletop lensless diffractive microscope with resolutions in the range of 200 nm using coherent $\sim$ 30 nm illumination. In addition, I describe some of the novel devices used to ensure a good signal-to-noise ratio in our data, including a magnetically-coupled vacuum compatible filter wheel. Finally, I discuss the scalability of our microscope to shorter wavelengths and its promising future.

Chapter 2

High-Order Harmonic Generation and Hollow Gas-Filled Waveguides

2.1 Introduction

In July of 1960, Theodore Maiman demonstrated the first laser [2]. This light source could be focused to higher intensities in the laboratory than any other light sources previously available, and opened the door to the new and remarkable field of nonlinear optics. After the birth of the laser, the demonstration of nonlinear optical phenomena revolutionized the science of optics, bringing new understanding to the interactions of light and matter.

More recently, high-power ultrafast laser amplifiers have been developed that produce high energy pulses with durations in the femtosecond (fs) regime [3]. These systems rely on some version of the chirped pulse amplification (CPA) scheme to avoid nonlinear effects and optical damage during the amplification process; the pulse is stretched in time before amplification and then compressed afterwards using gratings or other means [4, 5]. The phenomenally short pulse widths and high powers of such lasers not only allow time-resolved pump-probe experiments, but have also allowed researchers to push the limits of high harmonic generation (HHG) [6]. HHG represents a most extreme realm of nonlinear optics in which 10's or even 100's of photons from a visible laser are combined together in a frequency upconversion process that can extend into the x-ray region of the spectrum. Much of my experimental work has revolved around increasing the efficiency of this process, and using the coherent short-wavelength light that results.

2.2 Basic Principles of High Harmonic Generation

2.2.1 Extreme Nonlinear Optics

The very high brightness of lasers allowed researchers to obtain large optical fields that were not previously accessible. Before the advent of the laser, optical systems were traditionally analyzed according to a theory in which a linear relationship between the applied electric field E and a material's response to this field, the polarization P, was assumed. This relationship is given by

$$P = \epsilon_0 \chi E \tag{2.1}$$

where χ is the susceptibility tensor. However, when tightly focused, a typical laser beam can produce electric field strengths in excess of 10^{10} V/m. These field strengths are on the order of atomic Coulomb fields, and possess the ability to drive a material's response past the linear regime. In many cases, we can understand the nonlinear response using a perturbative approach in which we describe the relationship between P and E with a power series:

$$P_i^{\omega} = P_i^0 + \sum_j \chi_{ij} {E_j}^{\omega} + \sum_{j,l} \chi_{ijl} \nabla_l {E_j}^{\omega} + \sum_{j,l} \chi_{ijl} {E_j}^{\omega_1} {E_l}^{\omega_2} + \sum_{j,l,m} \chi_{ijlm} {E_j}^{\omega_1} {E_l}^{\omega_2} {E_m}^{\omega_3} + \sum_{j,l} \chi_{ijl} {E_j}^{\omega_1} {B_l}^{\omega_2} + ... \tag{2.2}$$

This approach explains numerous phenomena, including sum- and difference-frequency mixing, the Pockels effect, the Raman effect, and the Kerr effect, to name a few of the more frequently used nonlinear processes [7]. However, for some extreme nonlinear processes, such as high harmonic generation (HHG), even the perturbative approach fails. HHG represents a most extreme version of nonlinear optics. In lower-order harmonic processes, the optical field perturbs the atom. In contrast, the laser field strengths required to drive HHG are so enormous that the atom effectively perturbs the field, and the perturbative approach can no longer be relied upon to yield accurate predictions.

2.2.2 3-Step Model

Although the most accurate description of HHG involves numerical integrations of the nonlinear Schrödinger equation, a quasi-classical three-step model exists that accurately predicts the general features of HHG and provides a physical picture of the interactions involved [8, 9]. In the three-step model, the laser field ionizes a valence electron, which proceeds to follow a trajectory determined by the laser field until it recombines with its parent ion. Essentially, in this model, the powerful deceleration of the electron during recombination produces bremsstrahlung radiation.

In the first step, the intense laser field suppresses the Coulomb potential of the atom, allowing the electron to ionize by absorbing multiple photons, or by tunneling through the Coulomb barrier. For very strong fields, tunneling becomes the more probable ionization mechanism. In addition, the intensity dependent rate of ionization may be accurately predicted by incorporating a quantum mechanical calculation known as the ADK rate (named for its inventors Ammosov, Krainov, and Delone) [10]. Once the electron ionizes, the second step involves its evolution in the laser field. Since the laser field dominates the Coulomb potential, we consider the electron as 'free' during this step. As the optical field oscillates, it first propels the electron away from the ion, and then, when the field reverses, the field accelerates the electron back toward the ion. We see that ionization or recombination can occur on every half-cycle of the driving field. In addition, we note that only linearly polarized fields lead to electron trajectories that return the electron to the ion [11]. During the second step, the electron gains a time-averaged kinetic energy, associated with being subjected to a sinusoidal field, known as the ponderomotive energy. The ponderomotive energy U_p is given by

$$U_p = \frac{e^2 E^2}{4 m_e \omega_0^2} \tag{2.3}$$

where e the electron charge, m_e is the electron mass, E is the electric field of the driving laser and ω_0 is its frequency. For a given laser frequency, U_p is directly proportional

to the square of the electric field. Therefore, U_p scales linearly with the driving laser's intensity. Finally, in the third step, the electron recombines with its parent ion, and in so doing, releases its kinetic energy and the ionization potential of the atom as a high harmonic photon. Considering this third step, an accurate prediction of the highest achievable photon energy can be made and is given by this simple cutoff rule

$$(\hbar\omega)_{max} = I_p + 3.2U_p \tag{2.4}$$

where I_p is the ionization potential of the gas species being used, and the factor of 3.2 relates to the optimum phase for the ionization of the electron with respect to the oscillating electric field [8,9]. From the single atom point of view, the cutoff rule suggests that to increase the highest obtainable photon energies, we should use atoms with high ionization potentials, like the noble gases, and ionize them with the most intense laser pulses available. Of course, maximizing the flux of high energy photons is a much more complicated matter, that requires navigating the effects of many radiating atoms under dynamic conditions.

2.3 Phase-Matched Frequency Upconversion in Hollow Waveguides

2.3.1 Phase Matching in Nonlinear Optical Frequency Conversion

In the summer of 1961, P.A. Franken et. al. at the University of Michigan realized the possibility of exploiting the extraordinarily intense electric fields of focused laser beams to produce optical harmonics [12]. They reported the first nonlinear optical signal in the form of second harmonic generation (SHG). The generation of optical harmonics represents one of the most important applications of nonlinear optics, and has lead to the development of many novel coherent light sources. However, to efficiently produce optical harmonics, the process must be *phase matched*: i.e. the phase relationship between the fundamental and signal light must be maintained throughout the nonlinear medium.

In nonlinear optical frequency conversion, this concept of phase matching remains one of the most fundamental challenges. Looking at the issues associated with phase matching in the context of SHG provides a useful introduction. In the SHG process, two photons of a fundamental driving field are combined in a nonlinear crystal to produce a single photon that possesses twice the frequency of the fundamental light. From a more classical electromagnetic perspective, the fundamental wave with frequency ω induces a polarization wave at frequency 2ω via an interaction with the materials second-order nonlinear susceptibility. Driven by the fundamental wave, this polarization wave travels with an identical phase velocity that depends on $n(\omega)$. However, the second-harmonic wave radiated by the polarization wave propagates at a speed determined by $n(2\omega)$ [7].

In general, in SHG, the fundamental and second harmonic waves will travel at differing phase velocities. Thus, the two waves will possess a time evolving phase relationship. The relative phase difference between the two waves determines the direction of power flow between the waves [13]. So, maintaining the proper phase relationship proves essential for efficient SHG. In the case of SHG, the process of ensuring zero phase slip between the fundamental and harmonic fields is referred to as phase matching. When phase matched, the generated second harmonic at any point in the medium always adds in phase with that generated earlier in the medium. When the conversion process is not phase matched, the coherence length equals the distance in a crystal over which the phase slip between the fundamental and second harmonic equals 180° [7]. Therefore, unless an SHG process is phase-matched, the coherence length is the longest length over which a macroscopic output signal can be generated.

Phase matching is not automatic in most media. In general, the fundamental beam and the second harmonic beams, with angular frequencies ω and 2ω respectively, travel at differing speeds as they propagate through a material. This effect arises from classical dispersion; the phase velocity is given by $v_\omega = c/n_\omega$, and n_ω is frequency dependent. In terms of **k**-vectors, where $k_\omega = \omega/v_\omega = \omega n_\omega/c$, for second harmonic

generation we have

$$\omega + \omega = 2\omega \tag{2.5}$$

which is a statement of the conservation of energy, since the energy of a photon is given by $E = \hbar\omega$. Furthermore, we have

$$\Delta\mathbf{k} = \mathbf{k}_{2\omega} - (\mathbf{k}_\omega + \mathbf{k}_\omega) = \frac{2\omega}{c}(n_{2\omega} - n_\omega) \tag{2.6}$$

which is a statement of the conservation of momentum, since the momentum of a photon is given by $\mathbf{p} = \hbar\mathbf{k}$. Since $n_\omega \neq n_{2\omega}$ due to dispersion, clearly, $\Delta\mathbf{k} \neq 0$ in general. Furthermore, if we assume a lossless nonlinear medium, the Poynting vector $\mathbf{S}$ is given by

$$\mathbf{S}_{2\omega} = \frac{(2\omega)^2}{2n_\omega n_\omega n_{2\omega}} \left(\frac{\mu}{\epsilon_0}\right)^{\frac{3}{2}} \mathbf{d}^2 L^2 \mathbf{S}_\omega \mathbf{S}_\omega \left[\frac{\sin(\Delta\mathbf{k}L/2)}{(\Delta\mathbf{k}L/2)}\right]^2 \tag{2.7}$$

where L is the distance traveled in the material, and $\mathbf{d}$ is known as the nonlinear optical coefficient and describes the strength of the nonlinearity. This equation shows that when no phase matching occurs, the energy in the second harmonic varies as $\mathrm{sinc}^2(\Delta\mathbf{k}L/2)$, and it will be maximum at a distance

$$L = L_c = \frac{\pi}{\Delta\mathbf{k}} \tag{2.8}$$

known as the coherence length. After the second harmonic wave propagates over a coherence length, energy begins to return to the fundamental wave [7].

Employing some actual values to calculate a typical coherence length reveals an immediate obstacle to efficient SHG. Suppose we wish to frequency double a wavelength of 1 μm to a wavelength of 500 nm in the visible region of the spectrum using a KDP crystal as the nonlinear medium. For SHG,

$$L_c = \frac{\lambda}{4(n_{2\omega} - n_\omega)} \tag{2.9}$$

So, in this case, n_ω=1.50873, $n_{2\omega}$=1.529833, and the coherence length is a meager 11.8 μm [12]. Most nonlinear materials exhibit similar coherence lengths. So, the

second harmonic signal only grows for a small number of optical cycles, leading to extremely low conversion efficiencies. Clearly, from the definition of L_c given in Equation 2.8, decreasing $\Delta\mathbf{k}$ increases the coherence length. Moreover, from Equation 2.7 for the Poynting vector, as $\Delta\mathbf{k}$ approaches zero, the second harmonic signal will grow proportionally to L^2 [7]. The general features of phase-matched versus unphase-matched signal growth are illustrated in Figure 2.1.

2.3.2 Phase Matching of HHG in Gas-Filled Hollow Waveguides

Unfortunately, the nature of HHG presents several significant obstacles to phase matching. Perhaps the most daunting, is that the process takes place in a gas. As such, the nonlinear medium is optically isotropic, and does not afford the possibility of traditional phase-matching techniques based on differing source and signal polarizations encountering separate indices of refraction. Additionally, the most straightforward manner of producing high harmonics involves focusing high intensity laser light into a pulsed gas jet. A pulsed gas jet minimizes the gas load on a vacuum system, and the driving laser merely needs to be focused with sufficient intensity into the jet to produce harmonics. However, when traversing a focus, a laser beam undergoes a π phase shift, known as the Guoy phase shift [14]. This intrinsic phase shift destroys the possibility of phase matching in the gas jet method over extended propagation distances (over short distances, the Guoy phase actually can be used to compensate for other sources of phase mismatch).

Still, with the innovation of a hollow-waveguide geometry, phase-matched HHG was realized in the late 1990's [15]. The hollow waveguide approach to phase matching relies on several important features of the waveguide. First, when laser light is coupled into the guide, it does not go through a focus and travels instead as a plane wave. Second, the light experiences a frequency dependent dispersion while propagating through the waveguide. Finally, since the waveguide confines the gas in which the HHG takes place,

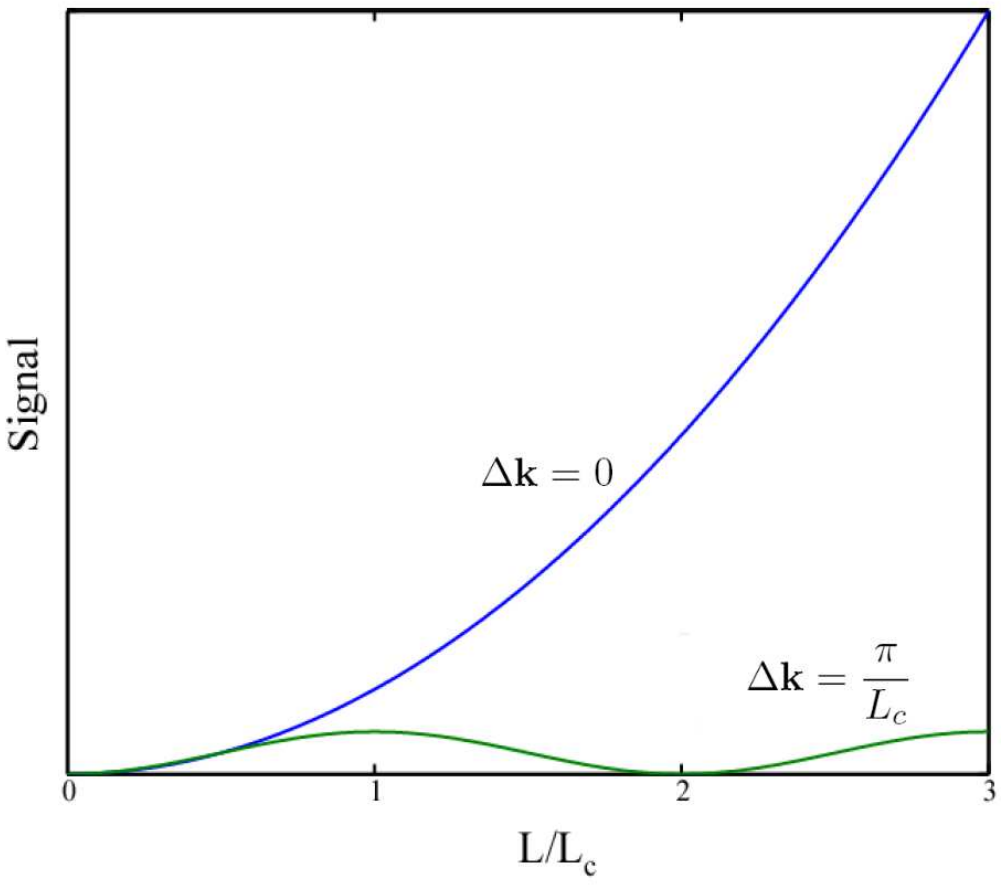

Figure 2.1: Phase-matched signal growth (blue) compared to unphase-matched signal (green) for several coherence lengths

the pressure of the gas may be controlled, allowing the strength of the dispersion caused by the gas to be tailored. The k-vector for the fundamental light propagating through a hollow waveguide in the lowest loss mode can be written as

$$\mathbf{k} \approx \frac{2\pi}{\lambda} + \frac{2\pi P(1-\eta)\delta(\lambda)}{\lambda} + (1-\eta)n_2 I - P\eta N_{atm} r_e \lambda - \frac{\mu_{11}^2 \lambda}{4\pi a^2} \tag{2.10}$$

where λ is the wavelength in the guide, N_{atm} is the number density of neutral atoms at atmospheric pressure, $\delta(\lambda)$ is a function corresponding to the dispersive characteristics of the gas species being used, P is the gas pressure, η is the ionized fraction, r_e is the classical electron radius, μ_{11} is the first root of a Bessel function of zeroth kind J_0 corresponding to the lowest loss mode, and a is the radius of the waveguide [16]. Factoring out the pressure term from Equation 2.10 and neglecting the small contribution of the nonlinear index of refraction gives

$$\mathbf{k} \approx \frac{2\pi}{\lambda} + P\left[\frac{2\pi(1-\eta)\delta(\lambda)}{\lambda} - \eta N_{atm} r_e \lambda\right] - \frac{\mu_{11}^2 \lambda}{4\pi a^2} \tag{2.11}$$

In the case of the EUV wavelengths of interest, the waveguide has a negligible effect on the phase velocity, which is then slightly greater than c for the harmonics at ionization levels where the pressure dependent term remains positive. For phase matching, we need

$$\Delta\mathbf{k} = \mathbf{k}_q - q\mathbf{k}_0 \tag{2.12}$$

where q is the harmonic order so that $\mathbf{k}_q$ is the k-vector of the qth harmonic and $\mathbf{k}_0$ is the k-vector of the fundamental driving laser. Clearly, $\mathbf{k}_q$ and $\mathbf{k}_0$ for light traveling in the waveguide will be given by Equation 2.11 but with λ replaced by λ_q or λ_0 respectively. So, for the HHG process taking place in a waveguide, and using the knowledge that for high-order harmonics $q\lambda_q = \lambda_0$ and that $q\lambda_0 \gg \lambda_q$,

$$\begin{aligned} \Delta\mathbf{k} \approx \frac{q\lambda_0\mu_{11}^2}{4\pi a^2} \quad &+ \quad P\left\{\eta N_{atm} r_e (q\lambda_0 - \lambda_q) - \frac{2\pi(1-\eta)[\Delta(\delta)]}{\lambda_q}\right\} \\ where, \qquad &\Delta(\delta) = \delta(\lambda_0) - \delta(\lambda_q) \end{aligned} \tag{2.13}$$

Looking at Equation 2.13, the pressure dependent term will have an opposite sign than the waveguide term for low levels of ionization. Thus, by tuning the gas pressure in the waveguide for a given ionization fraction, we can achieve the phase-matched condition for a wide range of experimental parameters [16].

One of the main limitations of the pressure-tuned phase-matching technique in a hollow waveguide is the level of ionization at which the technique still works. Clearly, if the gas is fully ionized, the overall sign of the pressure dependent term in Equation 2.13 will be the same as the waveguide term, and pressured-tuned phase matching is no longer possible. So, the pressure dependent term can be solved for the ionization fraction at which the overall term value equals zero. We refer to this ionization as the critical ionization and label it η_{cr}. Discarding the λ_q term, we find that

$$\eta_{cr} = \left[1 + \frac{N_{atm} r_e \lambda_0^2}{2\pi(\Delta\delta)}\right]^{-1} \tag{2.14}$$

Typical values of η_{cr} limit pressure-tuned phase matching to ionization levels $< 5\%$, and in turn, to photon energies of ~ 100 eV [11]. Methods of quasi-phase matching to overcome this limitation are discussed in the following chapter.

2.4 3-Section Hollow Gas-Filled Waveguide Design with Outer-Capillary Fixture

When I first began my research, the 3-section hollow waveguide design using an outer-capillary fixture was well established in our group. The HHG process must take place in a tenuous gas. However, the EUV light produced must travel through vacuum so as not to be absorbed. The most popular method of overcoming this experimental dilemma involves using a pulsed gas jet. The gas jet allows a high pressure region to exist within the vacuum for a short time without putting a continuous high gas load on the pumping apparatus. However, as discussed earlier in the beginning of Section 2.3.2, a gas jet does not allow phase matching over a long interaction region.

The 3-section design solves the basic experimental dilemma of confining a low pressure gas to a waveguide in an otherwise evacuated environment via differential pumping, and maintains a constant and tunable gas pressure within the central section [15]. The design consists of three pieces of fused silica capillary held in place by vacuum compatible epoxy in a larger outer capillary that serves as an alignment and gas handling fixture. Fused silica is used as the waveguide material as it provides excellent properties in terms of resistance to thermal and laser damage, and does so in a cost-effective manner. The three smaller capillary pieces are referred to as the inner capillary, and have a typical outside diameter of 1.20 mm. The outer capillary has a 0.250" outer diameter and an inside diameter that only slightly exceeds the outside diameter of the inner capillary (typically by $\sim 10\ \mu m$). The inner capillary can be obtained in several inside diameters, but in the experimental work discussed in this thesis, all inner capillary pieces have an inside diameter of 150 μm. In general, the length of the waveguide is referred to by the length of the central inner capillary, since the HHG process occurs within this region. The length of the waveguide generally varies between 2.5 cm and 10 cm, depending on the gas being used, since the short absorption lengths of some noble gases in the EUV limit the useful interaction length supplied by the waveguide. The central inner capillary has a further piece of capillary at each end, referred to as an end piece. These end pieces are typically 5 mm long, and are placed within the outer capillary such that they maintain a 0.5 mm gap from the ends of the central inner capillary. Figure 2.2 displays a to-scale 3-d rendering of one end of the 3-section hollow waveguide design and shows the relative placement and geometry of the inner and outer capillary components. The 3-section hollow capillary assembly is designed to be pumped from each end of the outer capillary fixture while gas flows into the gaps separating the central inner capillary and its end pieces. Since the end pieces are small apertures with low conductance, a differential pressure can be maintained on each side of them, allowing the central inner capillary to achieve a constant gas pressure while

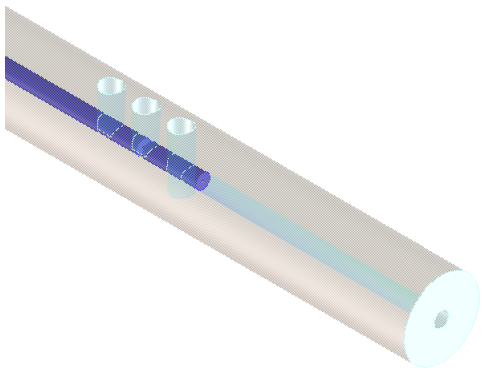

Figure 2.2: A to-scale 3-d rendering of one end of the 3-section design

the outer capillary ends are held at vacuum pressures. The gaps between the central inner capillary and its end correspond to radially drilled holes in the outer capillary that provide the passageways for positive gas flow. The outer capillary is made such that its ends are $\sim$ 3.5 cm from these gaps and a standard $\frac{1}{4}$" Ultra-Torr® fitting can be seated over each end and leave room for a $\frac{1}{4}$" Ultra-Torr® tee to form a seal over the gas input holes. The other two radial holes straddling the gas input holes at each end of the outer capillary serve as gluing ports. A picture of an outer capillary for holding a 10 cm inner capillary is shown in Figure 2.3, and a schematic with the relevant measurements is shown in Figure 2.4 . Using a thinned down q-tip end, epoxy is pushed into these holes to cement the inner capillary pieces into position. Note that Figure 2.2 and Figure 2.4 show that the axial hole centered on the end piece goes slightly deeper than the inner bore; the idea being that epoxy can be forced all the way around the end piece ensuring that the gas flow only occurs through the small conductance of the end piece inner bore.

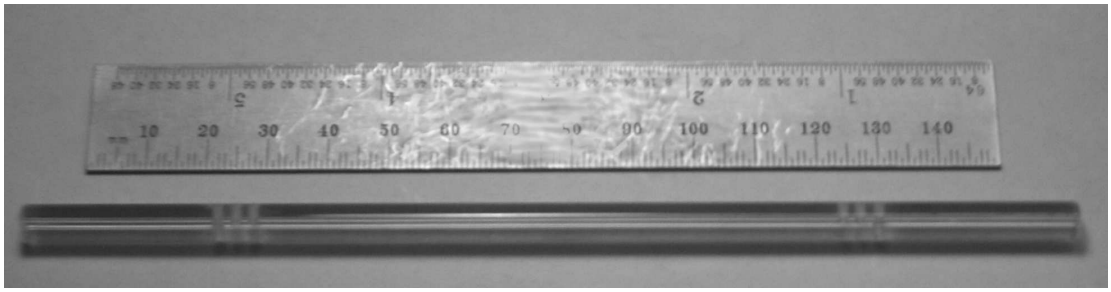

Figure 2.3: A picture of an outer capillary for the 3-section design

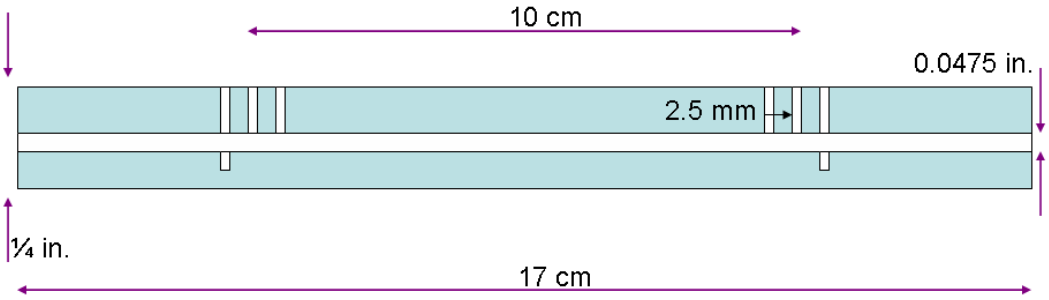

Figure 2.4: A schematic diagram of an outer capillary for the 3-section design

Chapter 3

Quasi-Phase Matching in Modulated Hollow Waveguides

3.1 Introduction

The extension of frequency conversion techniques leads to novel light sources and consequently new scientific tools. One of the main themes of HHG research is extending the tunability of this source, and the flux it produces, especially as the process is pushed towards shorter wavelengths. As discussed in Chapter 2.3.2, phase matching greatly increases the efficiency of this source, but pressure tuned phase matching faces serious limitations as the ionization of the gas in the waveguide exceeds a critical ionization level. However, we have demonstrated techniques for quasi-phase matching (QPM) of HHG that overcome this limitation. To make a clear intuitive picture of the QPM process, I first explore a theoretical approach to QPM for SHG, and then extend this picture to a basic approach to QPM for HHG in a hollow waveguide. Afterwards, the motivations for using structural changes to a waveguide to achieve QPM are discussed along with the successful implementation of this idea.

3.2 Quasi-Phase Matching for Nonlinear Optical Frequency Conversion

Under conditions not conducive to traditional phase matching, or where tailoring the nonlinear response is desirable, the method of quasi-phase matching (QPM) may be used. In the QPM scheme, a structural periodicity integrated into the nonlinear

medium corrects the phase relationship between the fundamental and signal light at regular intervals.

Since the pioneering work of Franken, nonlinear optical frequency conversion has grown into an immensely powerful scientific tool, as evidenced by the prolific use of such equipment as frequency doubled pump lasers and optical parametric oscillators. The most popular methods of achieving frequency conversion rely on birefringent phase matching. For all crystals not exhibiting the cubic class of symmetry, the index of refraction becomes a function of wavelength, propagation direction, and polarization. Such optically anisotropic crystals are referred to as birefringent, since, for a given direction of propagation, a light beam can interact with two different indices of refraction, depending on the beam's polarization [17]. This special property allows the possibility of perfect phase matching for SHG. If the fundamental and second harmonic light propagate collinearly in a birefringent crystal, but with mutually orthogonal polarizations, a condition can often be found wherein both beams experience the same index of refraction, and so, propagate at identical phase velocities. Ironically, the idea for QPM, devised independently by Armstrong et. al and Franken and Ward, predates the use of birefringent phase matching [18, 19]. However, the realization of QPM did not occur until the technologies associated with accurately manufacturing structured materials came of age. As demonstrated by nonlinear materials such as periodically poled $LiNB0_3$ (PPLN) that have been used for quasi-phase matched SHG, QPM continues to gain importance and utility [20].

In the QPM scheme, the relative phase mismatch between the driving and signal fields is corrected at regular intervals by the use of a periodic modification integrated into the nonlinear medium. Modifications useful for QPM alter the nonlinearity of the material, either by changing its strength, reversing its sign, or eliminating the nonlinearity altogether [13]. Figure 3.1 provides a useful introduction to this idea. This figure represents an alternating stack of crystals used for the QPM of an arbitrary SHG pro-

cess. Each slab has a thickness equal to the coherence length, and we assume that the index of refraction as a function of wavelength remains the same throughout the stack. However, every other slab lacks a nonlinear response. In this idealized arrangement, the SHG signal builds in the first slab. Then, just before energy begins to flow back to the fundamental field, the pump and signal waves enter the second slab. Energy transfer ceases at this point since no nonlinear response is present. However, the phase relationship between the pump and signal waves continues to evolve in the second slab. When the waves are back in phase, they encounter the third slab. This slab has a nonlinear response, so energy proceeds once again to flow to the harmonic wave. Moreover, since the correct phase relationship exists, the signal produced in the third slab adds constructively with the signal produced in the first slab, and so on [7]. A more

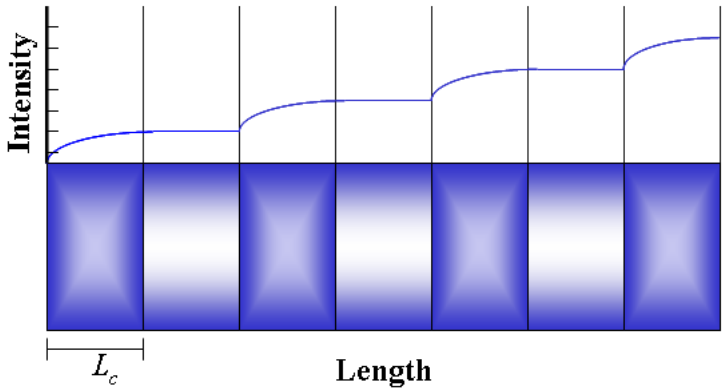

Figure 3.1: An idealized QPM geometry wherein each slab of crystal is a coherence length thick and every other slab of crystal lacks a nonlinear response

mathematically rigorous analysis of QPM SHG that closely follows the logic of Fejer et. al. shows some important insights into the QPM process [13]. Working under the assumptions of low conversion efficiency, weak focusing, long-pulse interactions, and a lossless medium, the slowly varying amplitude equation that describes the development

of the second-harmonic field is given by

$$\begin{aligned} \frac{dE_{2\omega}}{d\mathbf{z}} &= \Gamma \mathrm{d}(\mathbf{z}) e^{-i\Delta\mathbf{k}'\mathbf{z}} \\ \Gamma &\equiv \frac{i\omega E_{\omega}^2}{n_{2\omega}c} \end{aligned} \tag{3.1}$$

where $E_{2\omega}$ is the amplitude of the second-harmonic field, $\mathbf{z}$ is the distance along the direction of travel, $\mathrm{d}(\mathbf{z})$ is the spatially dependent nonlinear coefficient for SHG, and $\Delta\mathbf{k}'$ is the wave vector mismatch. To find the strength of the second harmonic field after traversing a material of length L, equation 3.1 is integrated with respect to z, giving

$$E_{2\omega} = \Gamma \int_0^L \mathrm{d}(\mathbf{z}) e^{-i\Delta\mathbf{k}'\mathbf{z}} d\mathbf{z} \tag{3.2}$$

Considering this integral as a Fourier transform leads to a transparent interpretation of the effect of QPM. Let

$$g(\mathbf{z}) \equiv \frac{\mathrm{d}(\mathbf{z})}{\mathrm{d}_{eff}} \qquad where \;\; -1 \leq g(\mathbf{z}) \leq 1 \tag{3.3}$$

then the Fourier transform of $g(\mathbf{z})$ is

$$G(\Delta\mathbf{k}') = \frac{1}{L} \int_0^L g(\mathbf{z}) e^{-i\Delta\mathbf{k}'z} d\mathbf{z} \tag{3.4}$$

Furthermore, assuming $g(\mathbf{z})$ is a function periodic in z, with period Λ expressed by

$$g(\mathbf{z}) = \sum_{-\infty}^{\infty} G_m e^{i\mathbf{K}_m\mathbf{z}} \qquad \text{where } \mathbf{K}_m = \frac{2\pi m}{\Lambda} \tag{3.5}$$

For all $\mathbf{K}_m$ far from the value $\Delta\mathbf{k}'$, the integrand will be a rapidly oscillating function averaging to zero. However, if $\mathbf{K}_m$ is near $\Delta\mathbf{k}'$, the integral is given by

$$E_{2\omega} \approx i e^{-\Delta\mathbf{k}\cdot L/2} \Gamma \mathrm{d}_Q L \mathrm{sinc}(-\Delta\mathbf{k} \cdot L/2) \tag{3.6}$$

where $\mathrm{d}_Q = \mathrm{d}_{eff} G_m$ and $\Delta\mathbf{k} \equiv \mathbf{k}_{2\omega} - 2\mathbf{k}_{\omega} - \mathbf{K}_m$. This approach yields an especially simple interpretation of QPM; i.e. the structure may be viewed as adding an effective wave vector to the phase-matching conditions.

3.3 Motivations for a Modulated Waveguide

As discussed in Chapter 2, HHG performed in a hollow waveguide lends itself to phase matching through pressure tuning of the gas filling the waveguide. Still, this method encounters limitations when attempting to reach higher energy harmonics. The driving laser generates higher EUV photon energies at high intensities that correspond to higher levels of ionization. At these high levels of ionization, the phase velocity of the driving laser beam exceeds the limit of pressure tuned phase matching. As the ionization approaches a certain level, which we call the critical ionization, the effect of neutral atoms grows smaller while the plasma dispersion increases. Thus, an asymptotically increasing pressure is required for phase-matching. Above the critical ionization level, phase-matching cannot be achieved in the hollow waveguide geometry. However, to overcome this obstacle, the concepts of QPM may be applied to HHG.

To induce QPM of the highest accessible harmonics, Christov et. al. proposed using a hollow waveguide with a periodic modulation of the inner diameter [21,22]. The primary assumption behind this idea is that the laser mode adiabatically follows the waveguide. Under this assumption, the laser mode expands or shrinks to fill the periodically varying cross-sectional area of the waveguide. Therefore, the waveguide regularly modulates the intensity of the driving field. The phase and the cutoff of the HHG emission depends on the laser intensity with extreme sensitivity, so the modulations in the waveguide effectively change the nonlinear interaction, allowing QPM to occur. Calculations by Christov suggested that significant enhancements at higher harmonic orders were possible with the correct modulation conditions [21].

Extending the formalism presented in the preceding section to the realm of HHG reveals that introducing a QPM k-vector, $\mathbf{\Delta k}$ in a waveguide under the influence of a QPM mechanism will be Equation 2.13, but with an extra term arising from QPM, and

having the form

$$\Delta\mathbf{k} \approx \left[\frac{q\lambda_0\mu_{11}^2}{4\pi a^2} - \mathbf{K}_m\right] + P\left\{\eta N_{atm} r_e(q\lambda_0 - \lambda_q) - \frac{2\pi q(1-\eta)[\Delta(\delta)]}{\lambda_q}\right\} \tag{3.7}$$

[23]. First-order QPM corresponds to modulating the waveguide (and harmonic emission) every coherence length and we will assume here that $m = 1$. Also, a critical periodicity, Λ_{cr}, can be defined where the QPM k-vector is equal to the k-vector of an evacuated unmodulated waveguide. This critical periodicity and its ratio to the actual periodicity (Λ)are given by

$$\Lambda_{cr} = \frac{8\pi^2 a^2}{q\lambda_0\mu_{11}^2} \qquad \beta = \frac{\Lambda_{cr}}{\Lambda} \tag{3.8}$$

where the dimensionless quantity β has been introduced to help characterize the general effect of the modulations.

To obtain a general illustration that summarizes the modifications to the phase-matching pressure due to the presence of a modulated waveguide, we introduce several dimensionless quantities. For a given set of experimental conditions, an optimum pressure for phase matching can exist. Calling this pressure P_{opt}, we define P_0 as the value of P_{opt} when $\eta = 0$ in the absence of any QPM k-vector. Solving Equation 2.13 for P_0 we find that

$$P_0 = \frac{\lambda_0\lambda_q\mu_{11}^2}{8\pi^2 a^2[\Delta(\delta)]} \tag{3.9}$$

Now, the ratio of P_{opt} to P_0 can be thought of as a normalized and dimensionless pressure, and the ratio of η to η_{cr} (defined in Equation 2.14) gives a normalized and dimensionless ionization level. Figure 3.2 shows a plot of P_{opt}/P_0 versus η/η_{cr} for several different ranges of β. The dotted line is where $P_{opt}/P_0 = 1$, and curves falling below the dotted line are not physical. For the blue curve, $\beta = 0$, and the trend of pressure-tuned phase matching in an unmodulated waveguide appears; i.e. an asymptotically increasing pressure is needed to achieve phase matching as the ionization level approaches the critical ionization. For the green curve, $\beta < 1$, and the waveguide modulations actually

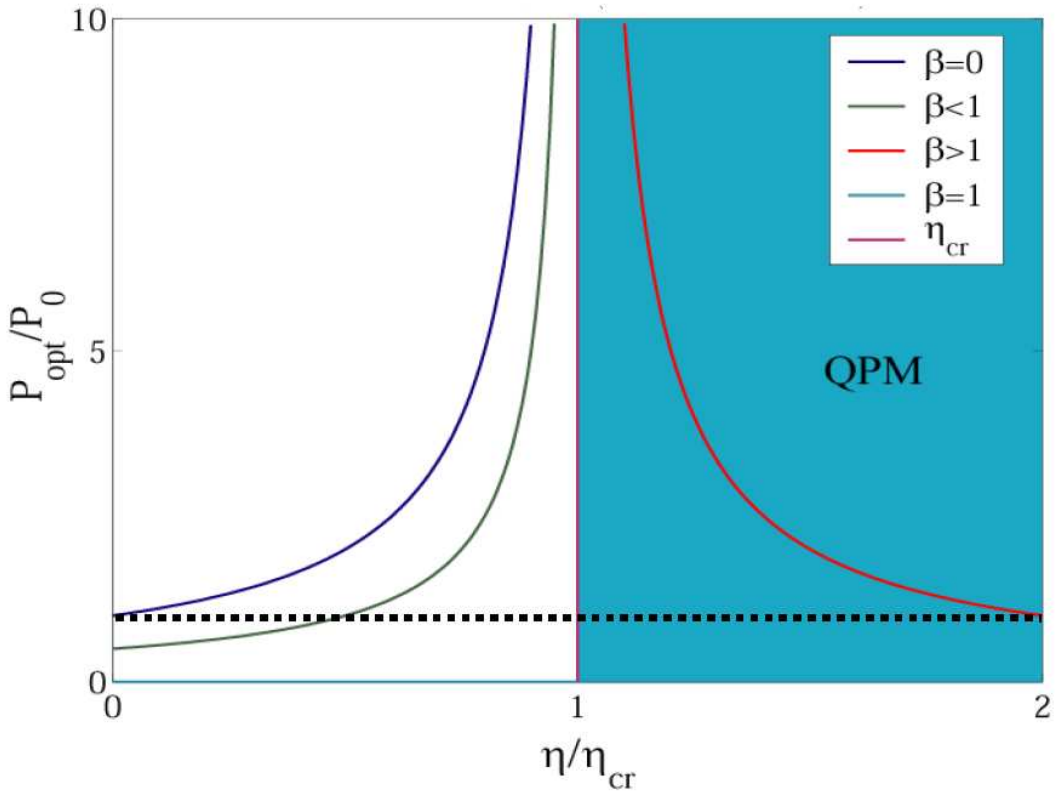

Figure 3.2: A graph plotting normalized pressure for phase matching versus normalized ionization fraction (courtesy Randy Bartels)

serve to decrease the range of ionization for which phase matching can be obtained. The most interesting curve is plotted in red, and it shows the situation for $\beta > 1$. This curve suggests that the useful range for which QPM operates is actually *above* the critical ionization! Thus, since higher photon energy harmonics are created at higher levels of ionization, adding a modulation to the waveguide that introduces a sufficiently large k-vector to Equation 3.7 should allow us to find a pressure at which we can quasi-phase match the HHG process for harmonic orders that were not accessible for the pressured-tuned phase-matching scheme in a unmodulated waveguide. In fact, as is shown in the following section, this QPM scheme is successful.

3.4 Using Modulated Waveguides for High-Order Harmonic Generation

3.4.1 The First Demonstration of Quasi-Phase Matching with High-Order Harmonics

Although developing fabrication techniques to produce modulated waveguides took considerable effort (described in Section 3.5), the use of modulated waveguides for high-order harmonic generation immediately generated a number of impressive results. The description of the first experimental results from these waveguides that follows relies heavily on a paper I wrote with Randy Bartels, "Quasi-phase-matched generation of coherent extreme-ultraviolet light" Nature, vol. 421, pp. 51-54, 2003 [1].

As mentioned previously, pressure-tuned phase matching in unmodulated hollow waveguides is limited to relatively low EUV photon energies. HHG can produce photons in this high ionization regime with energies of several hundred eV up to > 1 keV [24–26]. However, efficient phase-matched HHG had only been demonstrated at photon energies of between $50-100$ eV prior to the work presented here [15]. This limitation prevents the use of this source for applications such as *in vitro* imaging of small cellular structures,

which requires EUV light in the water window ($\sim$ 300 eV) region of the spectrum. Coherent sources in the 13-nm wavelength of interest to EUV lithography would also benefit from increased efficiency.

This flux limitation can be partially overcome by applying QPM techniques to HHG. Using a hollow waveguide with a periodically modulated diameter, the energy range over which we efficiently generate high harmonics can be increased significantly. In the experiment, 25-fs-duration pulses from a high-repetition rate (25 kHz, 1mJ per pulse) Ti:sapphire laser system operating at 760 nm were focused into 150μm inner diameter hollow waveguides filled with various noble gases [27]. The spectrum of the high harmonic radiation from these waveguides was recorded using a glancing incidence EUV spectrometer. The inner diameter of some of the waveguides was periodically modulated to alter the laser intensity traveling inside the waveguide. As represented in Figure 3.3, the modulations were approximately sinusoidal, with a period of 10.5 mm, and a radial depth of the order of 10μm, corresponding to a 13% modulation of the waveguide inner radius. The periodic structure modulates the generation of high harmonics and appears to restrict HHG to regions with favorable constructive interference. This work shows that sophisticated concepts of nonlinear optical photonics and engineered structures can be applied even to the extreme nonlinear optics of HHG. The highly nonlinear nature of the HHG process, though complicated, allows for new control mechanisms that do not exist in conventional nonlinear optics.

To interpret our results, we use previous theoretical predictions of the potential utility of QPM frequency conversion in the EUV [21, 28]. HHG is extremely sensitive to intensity; thus, a periodic modulation in the intensity of the driving laser will modulate the HHG emission. Generation of the highest harmonic orders is turned off when the waveguide bulge increases the mode diameter in the waveguide, thus preventing back-conversion of the EUV light. Therefore HHG will be quasi-phase matched when the period of the modulation matches the period of the phase mismatch between the

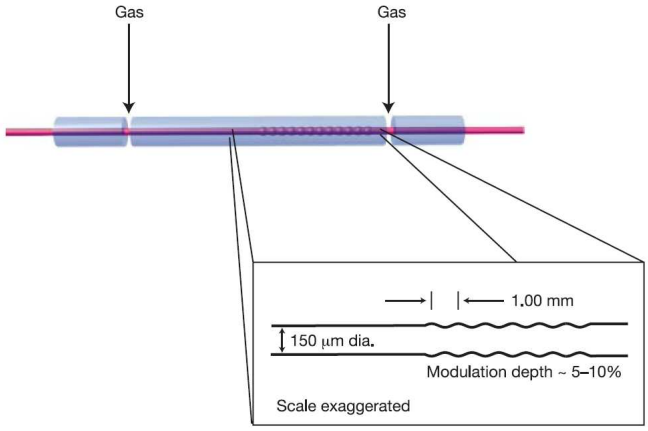

Figure 3.3: A schematic of the partially modulated waveguide in the 3-section configuration

pump and signal (that is, twice the coherence length). We also note that two other experimental works used QPM in low-order harmonic generation in gases [29,30]. However, these approaches are not applicable to the EUV. Other proposed schemes, such as suppressing HHG with interfering beams, were first demonstrated with gas jets in the EUV [31]. More recently, work in our own group has shown remarkable enhancements using counter-propagating light in unmodulated hollow waveguides to quasi-phase match the HHG process [32,33].

An intuitive picture of our experimental results can be obtained in the perturbative approach. The signal corresponding to the qth harmonic ($E_{q_\omega}(L)$) after propagation through a generation medium of length L is given by:

$$E_{q_\omega}(L) \approx \int_0^L E_\omega^q(z) d(z) e^{i\Delta k z} \mathrm{d}z \tag{3.10}$$

where $E_\omega(z)$ is the laser field, *d(z)* is the effective nonlinear coefficient for HHG, and $\Delta k = qk_\omega - k_{q_\omega}$ is the net phase mismatch between the fundamental and harmonic field. In the absence of phase matching or quasi-phase matching, the rapid $e^{i\Delta k z}$ phase term will cause the integral in Equation 3.10 to average to zero. This integral will be non-zero if either $\Delta k = 0$, corresponding to traditional phase matching in the visible or EUV, or

if $d(z) \approx \cos(\Delta K_M z)$; corresponding to traditional QPM in the visible. For the latter, the sign on the nonlinear coefficient *d(z)* is modulated periodically using periodically poled materials [13, 34–36]. The modulation period Λ (where $\Delta K_M = 2\pi/\Lambda$) is chosen to be equal to the coherence length of the signal, that is, the distance over which the fundamental and harmonic fields undergo a phase slip of π, to ensure that the harmonic signal from different regions in the interaction length always adds in phase.

In this work, a new type of QPM can be implemented in the EUV where the signal wave itself is modulated periodically, that is,

$$E_\omega^q \approx \cos(\Delta K_M z) \tag{3.11}$$

and d is independent of z. The periodic QPM structure can modulate the generation of high harmonic orders in several ways. Harmonics near cut-off that require higher laser intensity for generation can be turned on and off by the modulation. However, other effects (such as the periodic evolution of the phase of the driving pulse) can also contribute to a periodic modulation of the harmonic generation process. In fact, virtually any periodic change in the character of the harmonic emission can allow QPM to operate, particularly in a very-high-order nonlinear process where very small phase changes can dramatically change the output [37].

The significance of the quasi-phase matching discussed here is that it permits phase matching of HHG at higher ionization levels and hence higher photon energies than previously possible. This can be made apparent by calculating the coherence length that results from ionization of the gas. The plasma-induced change in index of refraction corresponds to a phase mismatch in Equation 3.10 of

$$\Delta k_{plasma} \approx \frac{q n_e e^2 \lambda}{4\pi m_e \epsilon_0 c^2} \tag{3.12}$$

where λ is the driving laser wavelength, e is the charge of the electron, m_e is the mass of the electron, ϵ_0 is the vacuum permittivity, and n_e is the electron density.

For fully ionized argon at a pressure of 1 torr, and for $q = 29$, $n_e = 3.3x10^{16}cm^{-3}$ and $\Delta k \approx 23cm^{-1}$. Therefore, the coherence length, L_c, given by $L_c = \frac{\pi}{\Delta k}$, is 1.4 mm. Thus, very substantial levels of ionization can be compensated for using the QPM technique demonstrated here, with experimentally realizable modulation periods in the millimeter range. In our experiments, because we could modulate at most a 2.5-cm-long section of capillary, we used higher pressures (30 torr). This higher pressure implies that the 1 mm modulation period compensates approximately for an additional 4% fractional ionization at harmonic order 29, and can be compared with a unmodulated waveguide where phase matching occurs at ionization levels of 24%. Thus, QPM more than doubles the allowable level of ionization in this case. For He, the effect of the QPM is greater, because the fractional ionization at which high harmonics are efficiently generated is much lower (<0.6% for $q = 61$, for example). Therefore, a small change in allowable ionization results in a large change in the energy of the highest phase-matched harmonic order.

Figure 3.4 shows the HHG spectrum from He, Ne and Ar gas for unmodulated (blue) and modulated (red) waveguides. These spectra were taken in the phase matched regime of the unmodulated waveguide. For all cases, the flux measured from the modulated waveguides is significantly greater (by factors of 25) than that measured from unmodulated waveguides. In this case, the modulated section was 1 cm in length, with a 1 mm periodicity, placed near the end of the waveguide. The measured flux corresponds approximately to 1 nJ per harmonic per pulse for Ar, and 20 pJ per harmonic per pulse for He at repetition rates of 2 kHz. Most significantly, the modulated waveguide increases the brightness of higher harmonic orders by at least two orders of magnitude. In the case of He, for the unmodulated waveguide the comb of harmonics spans an energy range from 60 to 80 eV, with a spectral peak at 68 eV (Figure 3.4a, blue trace). For the modulated waveguide, the spectral peak shifts by 27 eV, from 68 to 95 eV (Figure 3.4a, red), while the QPM harmonic comb also spans a broader energy range from 63 to 112

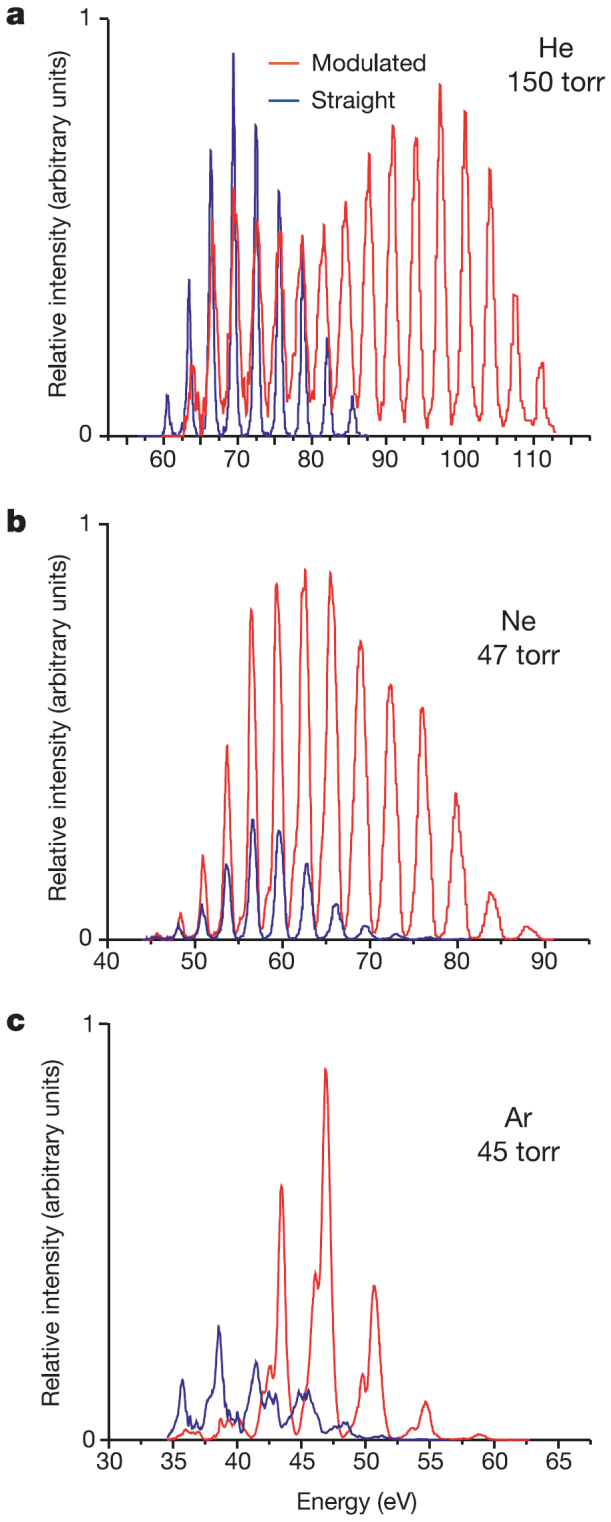

Figure 3.4: Experimentally measured HHG spectra for unmodulated (blue) and modulated (red) waveguides. Data are shown for He gas (a), Ne gas (b) and Ar gas (c), at pressures of 150 torr, 47 torr and 45 torr, respectively. From [1]

eV. Note that the wavelength region over which we achieve QPM easily includes the 94-eV (13 nm wavelength) region of interest for the next generation of EUV lithographies. In the case of Ne, use of a modulated waveguide extends the observed high-harmonic emission from 70 to 90 eV, while significantly increasing the flux (Figure 3.4b). In the case of Ar, the HHG spectrum from a unmodulated waveguide consists of a comb of phase-matched harmonics, peaked around 37 eV (Figure 3.4c, blue). For the modulated waveguide (Figure 3.4c, red), the HHG output spectral peak shifts to 47 eV, while the flux increases significantly.

We also investigated HHG from longer (2.5 cm) modulated waveguides with different modulation periods. Figure 3.5 shows the experimentally measured HHG spectra from He for three different periodicities of the modulated waveguides. All spectra were taken through two 200 nm zirconium filters, each of which transmits EUV in this range with $\sim 50\%$ efficiency, while reflecting or absorbing visible light [38]. The gas pressure was 111 torr, and the laser intensity was about $5\text{x}10^{14}$ W/cm^2. The different curves were taken at different positions of the grating in the EUV spectrometer, because of the finite spectral region that can be captured simultaneously on the CCD. Therefore, the cut-off at low energy is artificial, limited by the spectral window. The high-energy cut-off is limited by the available laser intensity. The spectra were also normalized to highlight the trend of increasing harmonic energy with decreases in the modulation period. As the modulation period is reduced from 1 mm, to 0.75 mm, to 0.5 mm, the high-energy cut-off increases from 112 to 175 eV. This cut-off was limited by the available laser intensity, and it increased in later experiments (see Section 3.4.2) when longer modulated sections, shorter laser pulses, and higher laser intensities were implemented.

Finally, by decreasing the modulation period from 1 to 0.5 mm (Figure 3.5), the amount of ionization that can be compensated increases, allowing for even higher harmonic orders to be phase matched. Furthermore, by increasing the length of the modulated waveguide and reducing the pressure, very high levels of ionization might

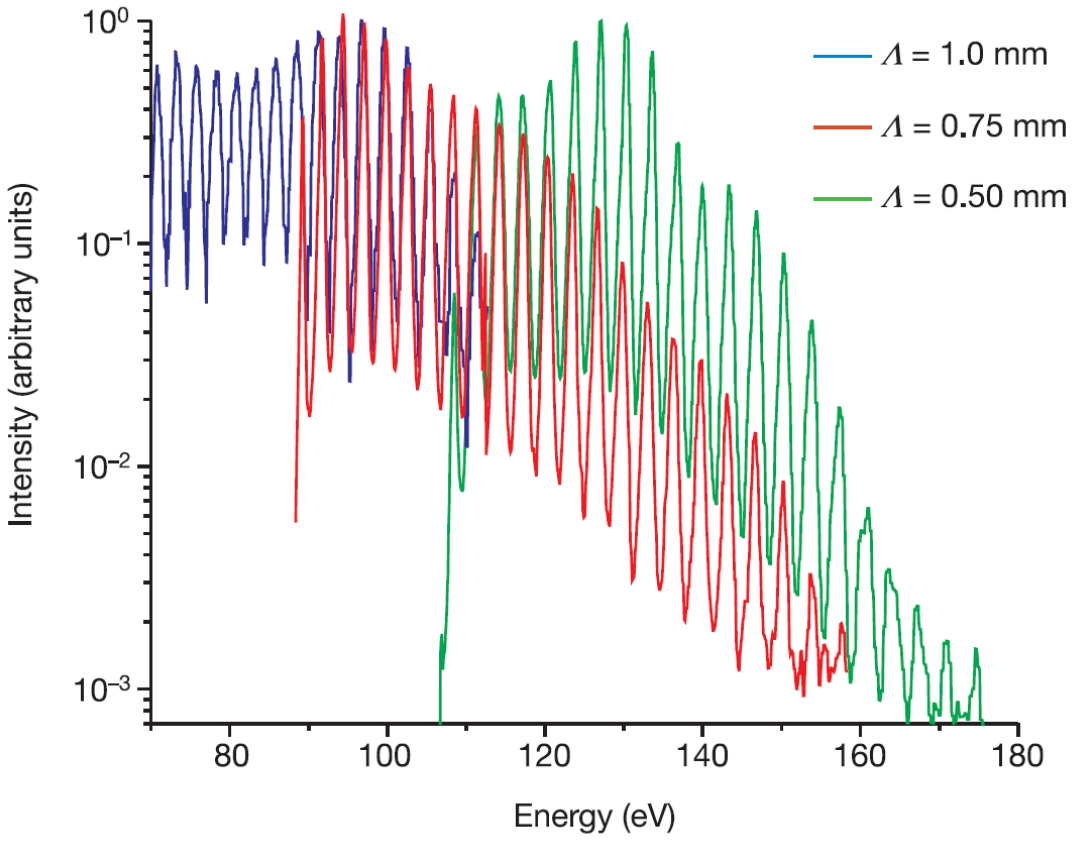

Figure 3.5: Experimentally measured HHG spectra (log scale) from He for three different periodicities of the modulated waveguides, each 2.5 cm in length. Blue, 1 mm periodicity; red, 0.75 mm periodicity; green, 0.5 mm periodicity. From [1]

be compensated for, leading to the generation of very-high-order harmonics, perhaps even from fully ionized gasses. This approach also leads to a significant increase in output flux, because the transparency of the gas is increasing with increasing photon energy over the range we investigate, while the effective nonlinearity is not changing rapidly. For He and Ne, for example, the absorption length is increasing with increasing harmonic photon energies. Therefore, we observed both higher harmonic orders and increased overall flux in the data of Figure 3.4.

3.4.2 Further Results

After the initial results presented in the preceding section, I performed further explorations of modulated waveguides with Emily Gibson, who was at the time a senior graduate student in our group. A thorough treatment of the results and interpretations of those experiments already exists in her thesis entitled "Quasi-Phase Matching of Soft X-Ray Light from High-Order Harmonic Generation Using Waveguide Structures" [39]. The reader is referred to this reference and the corresponding scientific papers for a detailed account [40, 41].

3.5 Producing Modulated Waveguides

When I first arrived in the Kapteyn/Murnane group, I was assigned to work with Dr. Sterling Backus. Ster, as he is known, is one of the world's experts on high power amplifiers for ultrashort laser pulses, and at that time was the senior leader of the labs. Although quite busy with his own duties and research, he was an excellent mentor, and recognized that he could suggest tasks to me that would require independent work and creativity. Still, being a young graduate student, I required guidance, and I wanted to make sure that at times when Ster was unavailable I could focus my efforts on a 'back burner' type of project. I had noticed that an interesting device for modifying the central inner capillary of the 3-section hollow waveguide consisting of a custom

miniature glass-blowing lathe built by Seth Weiman in the JILA Instrument Shop had been sitting idle in our lab together with a compact CO_2 laser operating at a 10 μm wavelength as a heat source.

The basic idea was to implement simple glass-blowing techniques to achieve a periodic modulation of the inner diameter of the inner capillary. The major differences between a glass-blowing lathe and a standard lathe are that a glass-blowing lathe has two headstocks whose motion is made synchronous through mechanical couplings, and one headstock generally accommodates a freely rotating feedthrough for gas pressure control. Glass-blowing lathes find their main application in scientific glass blowing, making glassware from custom test tubes and vessels, to specialized vacuum cells and flow controls. The primary advantages of such a lathe are that it allows cylindrically symmetric application of heat from a focused heat source, as well as a much higher degree of accuracy than manual rotation of the workpiece. However, if a cylindrical piece of glass is held in such a lathe and the headstocks do not rotate synchronously, a torque will be placed on the piece about the axis of rotation. As the glass is heated and begins to yield, it will twist about the soft point. Similarly, radial stresses will deform the glass with the application of heat, so a glass-blowing lathe must be accurately aligned and run true to avoid unwanted kinks in the workpiece. For a tube of glass placed in the glass-blowing lathe, the internal gas pressure must be controlled to create the desired effect; positive pressures will create a bulge, while negative pressures will constrict the tube. When heated in a glass-blowing lathe at slow rotation speeds for a given diameter, where the centripetal acceleration of the glass is less than the acceleration due to gravity, glass tubes tend to sag radially inward. Controlling the gas pressure compensates for this sag, increases it, or in the case presented here, can be used to bulge the inner diameter radially outward.

As mentioned in Chapter 2.4, the capillary that forms the 3-section waveguide is made of high purity fused silica. High purity fused silica glass is the noncrystalline or

amorphous equivalent of quartz. It possesses some unique characteristics that make it useful for high intensity laser waveguides. However, these characteristics must also be understood in order to yield the desired results from the glass-working processes. As compared to Pyrex glass, fused silica has some remarkable properties; a much higher softening point of nearly 1700° C, and nearly an order of magnitude smaller coefficient of thermal expansion. Whereas normal pyrex can be worked with a propane and oxygen flame, fused silica requires the heat of a hydrogen and oxygen flame. Although quite transparent in the visible part of the spectrum, fused silica is completely opaque for wavelengths above 7 μm for any reasonable thickness (i.e., several wavelengths) [42]. Therefore, a CO_2 laser operating in the far IR with sufficient power constitutes an ideal heat source for precision glass-blowing of fused silica. Amazingly, due to its low coefficient of thermal expansion, a piece of fused silica remains remarkably robust under thermal stress, as it can be heated white hot and then quenched in cold water without cracking. The high transmittance of fused silica at visible wavelengths, coupled with its resilience to thermal stress, combine to give it a high damage threshold for the ultrafast amplified pulses used in HHG. However, this material also possesses a low thermal conductivity, much like regular glass, that must be carefully taken into account in the glass-blowing processes.

When approaching the question of how to perform accurate glass-blowing on our delicate fused silica waveguides, I wanted to settle on the minimum number of adjustable parameters. Heat deposition, the area over which this heat acts, net force on the inner capillary wall, and the time this force acts while the glass is soft are the heart of the problem. However, rotation speed, convective cooling, thermal conductivity, cooling time, incident laser power, laser focal spot size, exposure time, and gas pressure all affect the final result of the glass-blowing operation. Although some literature exists describing the process of tapering capillaries with a CO_2 laser, it would appear that the type of glass-blowing I performed was novel to some extent [43,44]. With such a large parameter

space, and mainly trial and error as a guide, I decided to settle on a fixed rotation speed, internal gas pressure, output laser power, and focal spot size. Therefore, laser exposure time became the main adjustable parameter. For a complicated set of thermal transport conditions, I reasoned that an exposure time could be found that would create the desired modulation depth. The laser power was chosen using an optical pyrometer viewing a heated piece of capillary to verify that I could reach and maintain the softening temperature; I settled on around 6 W as a starting point. For pressurizing gas, I chose dry nitrogen, as I was concerned with maintaining the cleanliness of the capillary's inner bore. After some back-of-the-envelope calculations, I chose 50 psi as a working pressure, believing that once the fused silica had reached its softening point a pressure above 10 psi would produce a several micron change in the inner diameter within a couple of seconds. The original set-up focused the CO_2 laser with a single 10 cm focal length Zn-Se lens to an approximately 0.75 mm spot diameter. Nominally, considering heat transport and the Gaussian intensity distribution of a focused beam, a focal spot 75% the width of desired modulation period produces the correct, approximately sinusoidal, modulation.

When initially testing the apparatus, I quickly found that a high rotation speed produced the best results, which compelled me to begin the first in a series of modifications of this set-up. When I took on the capillary modulation project, the set-up was almost entirely hand operated and mostly untested. The rotary motor was coupled to the lathe drive shaft with an o-ring, and the drive shaft was coupled to the headstocks with miniature chains. To accurately create a periodic effect, the original glass-blowing lathe was mounted on a long-throw linear translation stage and driven by a micrometer screw. Moreover, the laser power and exposure time were also manually adjusted. The CO_2 laser pulses at a repetition of 5 kHz, and its power is adjusted by changing the pulse duration of the individual pulses from between 5 and 195 μs, with a maximum power of around 10 W; the percentage of the 200 μs pulse window used is referred to

as the duty cycle of this laser. The very first modulated waveguides made on this setup required me to fire the laser, time the exposure, time the cooling period during which I would translate the lathe to the next location, and then refire the laser. I settled on 3000 rpm as the rotation speed, which can be calibrated with a strobe light or a precision rpm indicator. The reasons for the success of a high rotation speed were twofold. First, the capillary must be convectively cooled in between laser exposures, or else the residual heat will cause a steadily increasing modulation depth. To this end, I added a fan to the set-up, but the high rotation speeds aided tremendously. Furthermore, to obtain consistent results, the heating of the capillary wall must be quite even. The laser is only interacting with slightly less than half the capillary perimeter at any given time, so ideally the time it takes for the heat to transfer to the inner wall will be on the order of half the rotation period, the rotation period being 0.02 s for 3000 rpm in this case. Although the thermal conductivity, denoted K, of fused silica varies with temperature, it will begin with a value of ~ 2 W$m^{-1}C^{-1}$ [45]. As a rough estimate, the time it takes for a given quantity of heat to transfer through a rectangular solid is given by

$$t = \frac{QL}{K(\Delta T)A} \tag{3.13}$$

where Q is the heat, L is the thickness of material, T is the temperature, and A is the area [42]. Considering a patch of fused silica exposed to 6 W for 0.01 s, 0.5 mm thick, with a temperature gradient of 1500° C, 0.75 mm on a side, the time for heat transfer will be about 0.02 s. Of course, this time can be increased by convective cooling, but it suggests the need for a high rotation speed. Miniature drive chains were not well suited to this application due to large vibration, nor was the original rotary gas coupling for pressurizing the capillaries. So, I refitted the lathe with miniature timing belts, a low-friction rotary coupling, and special clamps and mounts for reducing vibration.

The initial sets of modulated waveguides that I produced had been made with long exposure times at moderate laser powers. This ‘slow roasting’ approach was prob-

lematic in terms of laser power drift and the deformation of the outside diameter of the capillary. The CO_2 laser power is quite sensitive to its operation temperature, and the temperature of the building cooler water changes subtly over the day. More importantly, as the inside diameter of the capillary expands and the capillary wall moves outward, the outside diameter also increases. Since the 3-section outer capillary fixture relies on a tight fit between the inner and outer capillary components, I was forced to hand polish the modulated inner capillary to the correct outside diameter. The polishing was an extraordinarily delicate task that required a great deal of patience and a pragmatic acceptance that attrition of capillaries would inevitably occur during the process. To accomplish this task, I retrofitted a commercial glassblowing lathe with precision miniature chucks. With the capillary held in these chucks and the lathe rotating at less than 100 rpm, I would hold a diamond file gingerly to the underside of the capillary and slide it horizontally back and forth until the outside diameter had been ground down enough to fit into the outer capillary fixture. During this procedure enough pressure had to be applied for effective cutting action of the file, but too much pressure would easily snap the capillary. I finished by smoothing the outside with a ruby stone and cleaning off any residual glass dust.

Considering that the original paper suggested using a modulated waveguide calling for a change to the the inner diameter on the order of 1%, I originally focused my efforts on devising an accurate active measurement of the modulation depth. I considered capacitive methods, differential absorbtion of gas, interference, and imaging. However, at the time, the most straightforward approach turned out to be inspecting capillaries subject to various laser exposure times, and iterating the exposure time until the desired modulation appeared as judged by eye. Eventually, Amy Lytle perfected a nondestructive measurement technique, whereby the modulated capillaries were immersed in index matching fluid and photographed with a CCD camera mounted to a high-quality microscope. From the CCD image, and knowing the correspondence of

CCD pixel size to actual measurements at a given magnification, the difference in inner diameter between modulated and unmodulated sections of capillary can be judged to within $\sim 1\ \mu m$. In part, I originally decided to use the rather unsophisticated microscope inspection technique because I received a challenge from my advisors that went something to the effect of "You know that 'back burner' project of yours, well we have a grant review coming up...think you could make it work in two weeks?" At this point, I had improved the set-up and had a general feel for the modulation process, as well as the polishing technique necessary to incorporate the capillary into the 3-section design. Surprisingly, one of the first fully functional modulated capillaries I produced and incorporated successfully into a 3-section fixture generated notably unique spectra when used for HHG. The section of modulated capillary shown in Figure 3.6 is an example of one of the first successful modulated capillaries, made by the hand operated lathe described earlier. The results obtained from these initial efforts are described in the preceding section 3.4.1.

Clearly, as the utility of making modulated waveguides became apparent, more precision, flexibility, and automation was necessary in the glass-blowing apparatus. With the help of Randy Bartels, we added computer control to the laser exposure settings and the cooling time. The original apparatus had a limited travel range of 1 cm, so the lathe was reattached to a larger translation stage and precision realigned. In addition, I fitted a stepper motor and lead screw to the apparatus such that the lathe position could be automatically and accurately driven. This second-generation apparatus is shown in Figure 3.7. This set-up included two lenses, a 25 cm focal length for making the heating laser beam approximately the diameter of the capillary at its focus, and a 5 cm ZnSe cylindrical lens for creating a tight line focus along the axial direction of the capillary so that the period of modulations could be made as small as 0.5 mm. I should note that the optics were aligned such that the capillary would intersect the heating laser beam at the focus for the smallest periodicities and before the focus for

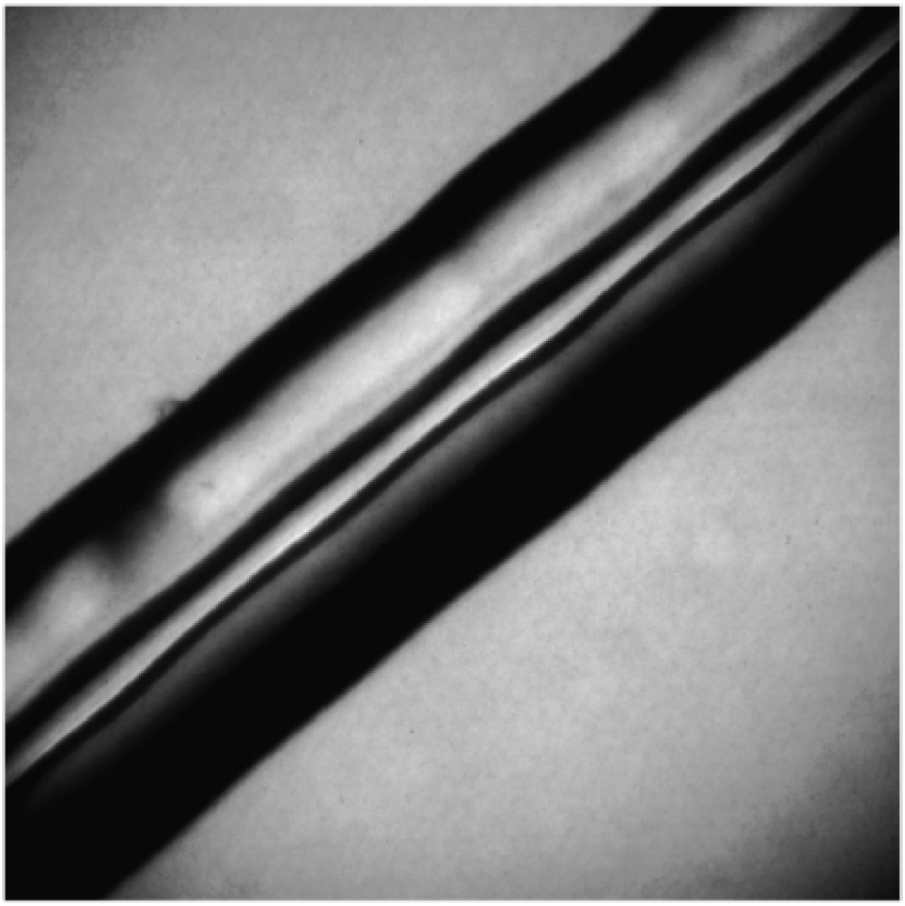

Figure 3.6: A short section of capillary with a 1 mm modulation period, note the deformation of the capillary's outside diameter

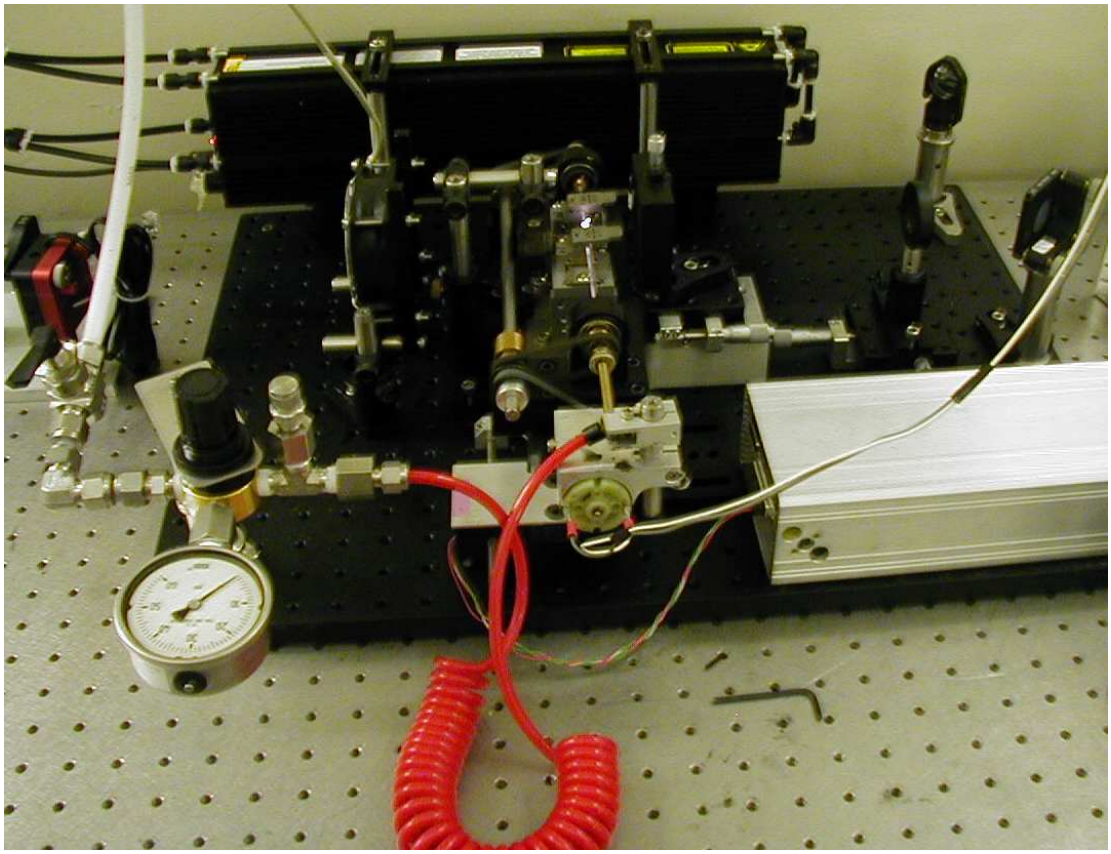

Figure 3.7: The second-generation glass-blowing set-up

longer periodicities; the idea being that the laser beam characteristics would be less affected if dust particles could fall through the focus during heating. The miniature timing belt drive configuration can also be seen in Figure 3.7, along with the motor mount and rotary coupling clamps.

Progressively, we were interested in extending the utility of the modulated waveguides, and wanted a glass-blowing system that would be flexible in terms of both the length of capillary that could be modulated and the periodicity of modulation. The eventual solution came in the form of the third-generation glass-blowing apparatus shown in Figure 3.8. The desire to modulate sections of capillary over 10 cm in length made mounting the entire lathe on a large translation stage impractical. Henry Kapteyn suggested that we build a new custom lathe, and mount the entire CO_2 laser on a moveable rail, with completely in-line optics. For this project I collaborated with Lee Thornhill of the JILA Instrument Shop, and he designed and built the first version of this third-generation set-up. Along with members of the shop, I have subsequently modified many of its components to optimize the design.

Since a 10 μm wavelength is not visible to the naked eye, nor to standard IR viewers, precise alignment of this far-IR laser beam becomes challenging, but a linear array of optics highly simplifies matters. The optics train consists of three cylindrical ZnSe lenses. For clarity, I will refer to the direction parallel to the capillary axis as the horizontal dimension, and the direction perpendicular to this as the vertical dimension. The first lens has a divergent -5 cm focal length and expands the beam in the horizontal dimension of the capillary to increase the f-number on the third lens, which has a 5 cm focal length. This geometry can focus the beam as tightly as 75 μm in width, as measured in the horizontal direction. I should note that despite the tighter focus available in this optics arrangement, the functional limit of this apparatus remains around 0.2 mm periodicity, most likely due to the difficulty of confining heat conduction when the periodicity becomes considerably shorter than the wall thickness of the capillary.

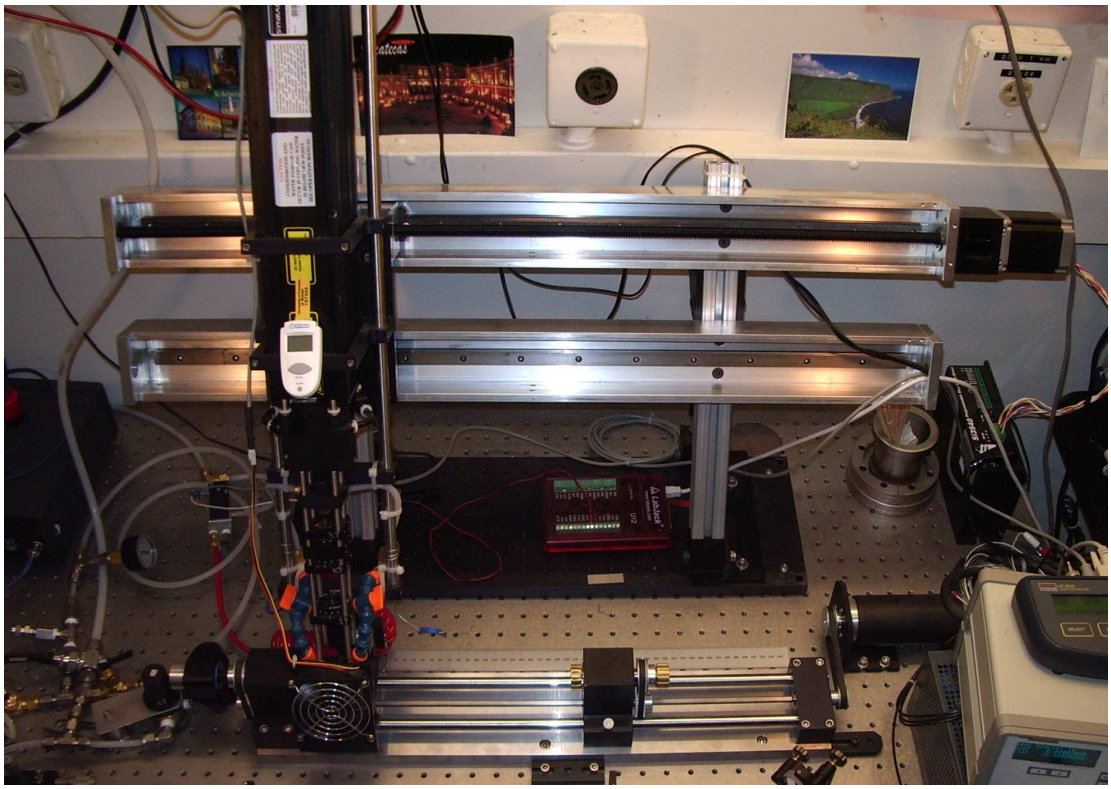

Figure 3.8: The current third-generation glass-blowing set-up

The second lens controls the beam size in the vertical dimension. The divergent lens is kept fixed, but the other two lenses can move along an optics rail to change the beam conditions depending on the operation being performed. For various modulation periodicities, the third lens can be moved such that the capillary intersects the beam at different points from the focus. During modulation operations, the second lens is set such that the beam size in the vertical direction matches the capillary diameter. During hole poking applications, as will be discussed later in this section and in Section 4.3.3, the second lens is set such that it generates a round focal spot.

In addition to the laser and optics being made into a mobile monolithic subassembly, the apparatus shown in Figure 3.8 incorporates several other major upgrades. The laser in the current set-up is a Synrad series J48-1W with an optional closed-loop power stabilizing head that provides a feedback loop for establishing an output power that fluctuates less than 1% during each exposure. The CO_2 laser does not provide an absolute power control, but for a given duty cycle, the power will remain quite steady for each exposure as long as the temperature of the laser remains constant. An IR temperature sensor is mounted to the laser body, and I adjust the cooling water flow such that a constant temperature of around 14° C is maintained during operation. Furthermore, the timing is accurately controlled with a digital delay generator (Quantum Composers Model 9512 pulse generator).

Great care has also been taken in the alignment of the lathe. The metal rods on which the lathe components sit are precision ground solid rods of hardened stainless steel that have been selected for straightness. Furthermore, the lathe is mounted on a hardened plate of ground tool steel. The lathe is carefully aligned using dial indicators and precision pin gauges, as shown in Figure 3.9, such that the components have a mutual run out of less than 0.0005". With the help of Mark Siemens, a set of gas jets for convective cooling were attached to the optics mounting rail, so that a rush of gas could flow over the heat affected zone after each laser exposure. Since they are attached

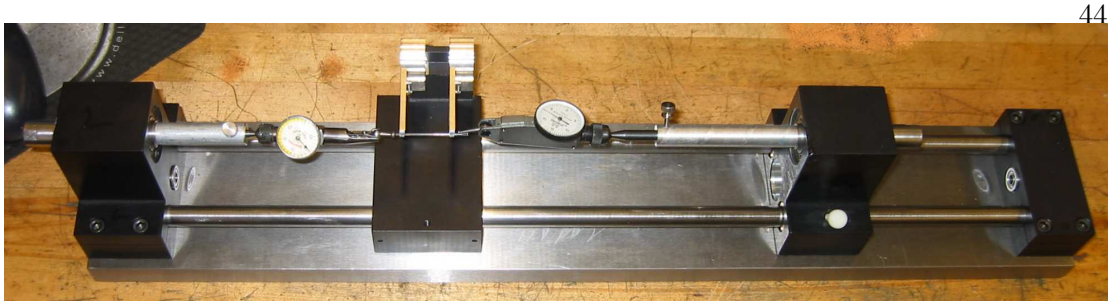

Figure 3.9: The third-generation custom glass-blowing lathe getting a tune up

to the optics rail, these jets move along with the laser, and their flow is controlled by a computer automated solenoid valve, allowing precise optimization and coordination of the cooling period. For additional convective cooling, I mounted a fan on a steady rest that tracks the motion of the laser. Unlike the original lathe, both headstocks are pressure sealed. Before the current set-up, I was forced to flame polish one end of the capillary shut so that the inner bore could be effectively pressurized, but this delicate operation is no longer needed. Additionally, the stepper and driver motors in the third-generation are more powerful and precise (5107.68 steps/mm, HT23-400 motor driven by Si3540 stepper motor driver, both from Applied Motion Products). In striking contrast to its humble beginnings, the current apparatus is fully automated once the capillary has been loaded into place.

Serendipitously, while endeavoring to increase the efficiency of the modulating process, I found that with the correct combination of laser intensity and exposure time, I could eliminate the polishing of the capillaries. Initially, the laser exposure times were on the order of 40 s with nearly 2 minutes of cooling time between exposures. Modulating a 2.5 cm section of capillary at a periodicity of 0.25 mm translated to 100 modulations, and a highly time consuming task. The active cooling jets significantly reduced the cooling time down to 1 or 2 seconds. However, a quick calculation suggests that the time needed to heat the capillary should be more on the order of 1 s. The simple

relation $Q = mc\Delta T$ relates the heat Q that changes a piece of material with mass m and specific heat c by a temperature ΔT. Considering a length of solid cylindrical piece of fused silica h long with a radius R and a density ρ being heated by a laser with power P, the time t to change by ΔT is given by

$$t = \frac{P}{\pi R^2 h \rho c(\Delta T)} \tag{3.14}$$

Although the specific heat of fused silica varies somewhat with temperature, a value of $\sim$ 1000 J kg^{-1} C^{-1} will suffice for this estimate [45]. The density of fused silica is known to be 2200 $\frac{kg}{m^3}$ [42]. Assuming the cylinder is 1 mm in length with a radius of 0.60 mm and is being heated with a 6 W laser with 100% absorption, the time necessary for a change of 1500° C will be 1.6 seconds. Convective cooling will certainly lengthen this estimate, but still, the glass-blowing operation time appeared as though it could be easily shortened by an order of magnitude. While trying to decrease the laser exposure time with an increased laser power, I noticed an interesting phenomenon. At a 'sweet spot' of intensity, the CO_2 laser beam could both heat the capillary and simultaneously ablate its outer surface. Thus, when operating in this regime, polishing the outer surface of the capillary became an unnecessary step, as the original outside diameter was preserved at the unheated locations, and made slightly smaller at the heated locations. Unfortunately, finding this regime can be tricky, since too much intensity will lead to rapid ablation, and actually less heating of the capillary. If too much ablation occurs too rapidly, the heat deposited by the laser is carried away by evaporative cooling: small molten fused silica debris flies off the capillary or is vaporized by the laser.

So a careful balance of laser power and exposure time must be found for successful modulation of the capillary. Currently, the apparatus has a 'test' mode wherein the exposure time can be varied for each laser exposure. Once I identify the power and focusing parameters to bulge the inner diameter of the capillary, while also ablating

its outer surface, I make several test pieces to identify the optimal exposure time. Generally, I use a chirped exposure, and increase the exposure time in discrete steps every four exposures. When inspected under a microscope, these test pieces quickly reveal the optimal exposure time for a given set of modulation parameters. The result of the many improvements to the glass-blowing apparatus and procedure can be seen in Figure 3.10. This section of modulated capillary exhibits extremely regular and consistent modulations, with only a subtle change to the outside diameter.

Alignment of the apparatus described here is particularly challenging because of the invisibility of 10 μm light. If the laser is not directed along the capillary's radius, the outer wall will be ablated before the inner wall softens; therefore proper alignment is crucial. In fact, considering the travel of the beam from the output of the CO_2 laser to the point where it heats the capillary (around 40 cm), an angular deviation from the aligned laser path of 1x10^{-4} radians, or about 20 arc seconds, is enough to cause improper function. Fortunately, fused silica glows a very bright white when heated with the CO_2 laser, so this glow, along with the manner in which the laser cuts the capillary, can be used for alignment and for diagnosing beam parameters. For rough alignment, I use a hand held piece of capillary to identify the laser beam position in much the same way we normally use a plain white index card. To adjust the focusing optics, I turn the laser power down till only a faint glowing spot appears on a stationary capillary held in the lathe. Then the focusing optics can be adjusted to maximize this glow, indicating the tightest focal spot on the surface of the capillary. Since the Rayleigh length z_R given by

$$z_R = \frac{\pi {\omega_0}^2}{\lambda} \tag{3.15}$$

where ω_0 is the focal spot radius and λ is the laser wavelength, is on the order of several mm, the focusing optics can be accurately adjusted by this maximum glow technique. Once the position giving the tightest focus has been found, I note the positions of the

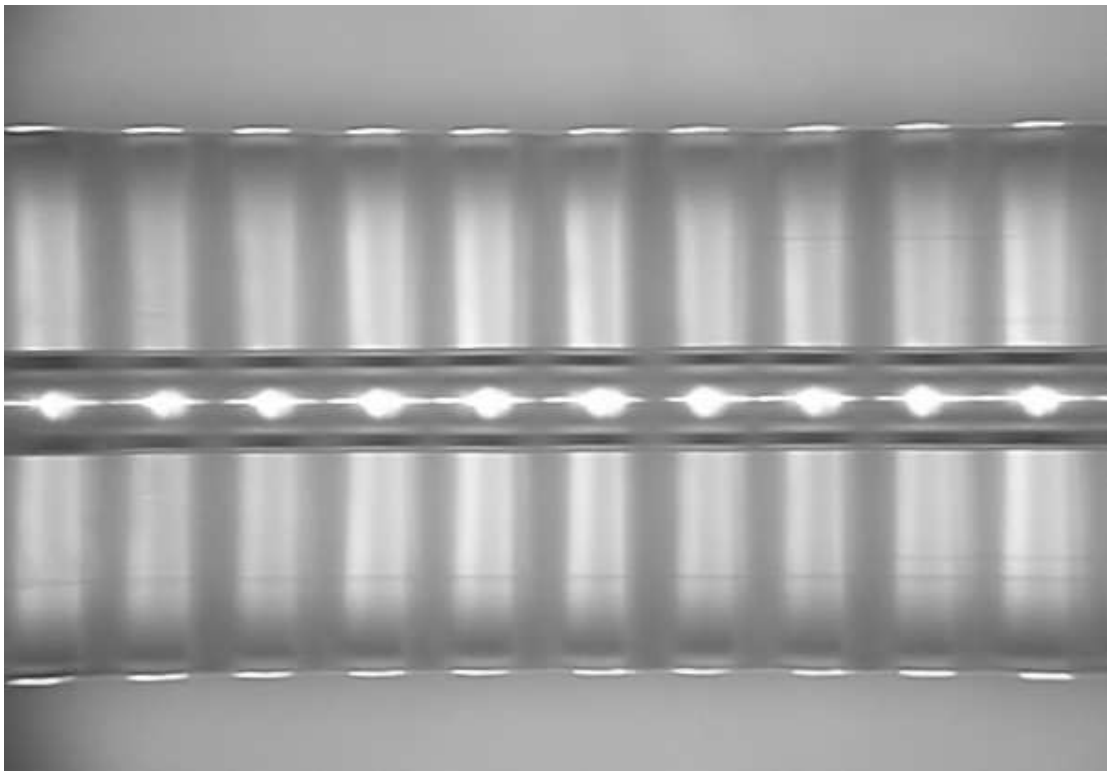

Figure 3.10: A short section of capillary made in the third-generation glass-blowing set-up with a 0.25 mm modulation period. This picture was taken without index matching fluid, and the periodic bright spots are merely an artifact of the microscope illumination and lensing effects of altered capillary

focusing optics and reference other configurations to these positions. For fine alignment of the beam pointing, I allow the laser to cut a hole in a stationary capillary and judge the hole's orientation relative to the radius of the capillary as shown in Figure 3.11. In addition, when the focusing is set to give a line focus, features cut into a stationary capillary allow me to judge the alignment of the line focus relative to the capillary as well as the astigmatism of the focused beam.

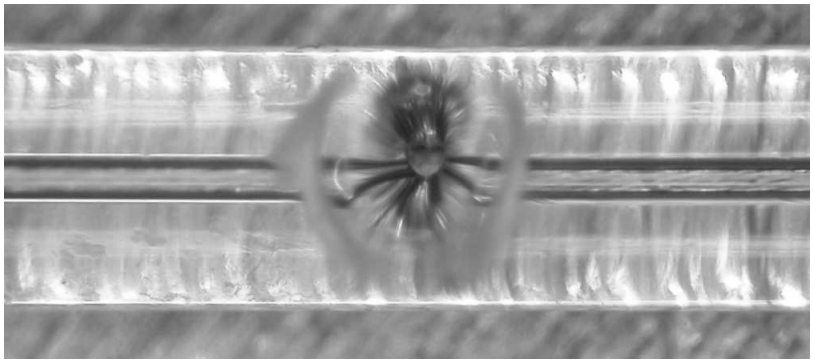

Figure 3.11: A hole cut in the capillary with the CO_2 laser showing how misalignment of the beam pointing can easily be diagnosed.

Although the current apparatus functions well, two main improvements could be made to make it more of a 'turn key' system. First, the CO_2 laser should be given a dedicated closed-loop water chiller. The absolute power of this laser is quite sensitive to its operating temperature and requires the exposure time to be readjusted even in the case of a drift as small as 1° C in the water temperature. Second, the ideal lathe design would incorporate commercially available precision collets. Currently, the weak link in the alignment of the lathe is the specially made collets used to hold the capillary and form a pressure seal to the headstocks. The current collets are made from small pieces of hard plastic, but are difficult to machine to the tolerances needed, and are easily damaged with improper handling. This second issue may require a redesign of the headstocks of the lathe and perhaps an alternative pressure seal. However, the benefits to long term dependable operation would be worth the effort.

3.5.1 Limitations of Modulated Waveguides and Perspective

Of course, solving challenges of precise technical glass blowing at the 100's of μm scale posed an interesting and rewarding task in of itself. However, I currently believe the main utility of this work was to demonstrate the feasibility of modulating the driving light field to achieve QPM in the HHG process. Although more could be done to improve the consistency and efficiency of producing modulated waveguides, they are an inherently tricky structure to create. Moreover, discovering the correct conditions to optimize QPM with this structure involves a slow feedback loop. A much more attractive solution is to employ alternative methods that allow adaptive real-time control of the driving laser field. One such approach, using weak counterpropagating light in an unmodulated hollow waveguide and recently employed by our group, has shown dramatic enhancements of flux at short wavelengths and holds great promise for future results [33]. Perhaps even more interestingly, this technique has proved to be a real-time probe of the HHG process within a waveguide, allowing us insight into the dynamics and optimization of QPM with the hollow waveguide [32]. Another technique using the beating of different driving laser modes within a hollow waveguide has also recently been proposed and claimed dramatic improvements of flux at short wavelengths [46, 47]. The addition of tailored pulse shapes and wavefronts, as well as more accurate models and diagnostic feedback tools will likely lead to even further improvements and extensions of HHG. Indeed, the ultimate solution to optimizing flux at difficult to reach wavelengths most likely will involve a combination of these approaches and tools.

Chapter 4

Hollow Gas-Filled Waveguides

4.1 Introduction

Over the past century, the technologies associated with transmitting high frequency electromagnetic radiation have rapidly grown in importance, particularly with the telecommunications revolution. One of the most important technologies, especially in recent years, has been the application of waveguide structures to the optical domain of the electromagnetic spectrum in the form of optical fibers for long distance communication. Waveguides come in many geometries, and are made from many materials, both metallic and dielectric [48]. However, for the purposes of guiding high intensity laser pulses for various nonlinear applications, hollow dielectric waveguides have become a popular choice [16, 49]. My personal experiences modifying hollow waveguides and incorporating them into the outer capillary fixtures lead me to question some of our established designs and assembly practices. Eventually, this questioning led me to a complete redesign of our fixturing system that incorporated my knowledge of physics, mechanical design, and glassblowing.

4.2 Hollow Waveguides

Since hollow waveguides are one of the essential elements in phase-matched production of high-order harmonics, I believe the basic parameters that can affect their performance should be explored. The results briefly summarized here come from two papers

that have long influenced the use and understanding of hollow waveguides. The first paper, by E. A. J Marcatili and R. A. Schmeltzer, is "Hollow metallic and dielectric waveguides for long distance optical transmission and lasers," Bell System Technical Journal, vol. 43, pp. 1783-1809, (1964) [50]. This paper is one of those rare gems for which the PDF cannot yet be found on the internet, and one must actually go to the library and make a photocopy of it. However, the paper gives the definitive treatment of the modes and loss mechanisms present in the waveguides we use. The second paper, by Richard L. Abrams, "Coupling Losses in Hollow Waveguide Laser Resonators," IEEE Journal of Quantum Electronics, vol. 8, pp. 838-843, (1972), describes the effect of different focusing conditions on the amount of power coupled into a hollow dielectric waveguide for the lowest loss propagation mode [51]. Since the HHG process depends so sensitively on laser intensity, the features of the mode coupled into the hollow waveguide, as well as the nature of this mode's propagation down the guide, affect the spectrum, mode, and flux of the upconverted EUV light.

4.2.1 Modes and Mode Beating

Marcatili and Schmeltzer describe the electromagnetic modes that propagate in a hollow dielectric waveguide. They perform their analysis assuming that the waveguide's inner bore radius is much larger than the free space wavelength of the field. Under this condition, the waveguide can be considered to guide the mode through a series of glancing incidence reflections. They also work under the assumption of infinite wall thickness (interestingly, they mention this condition is the same as frosting the external surface of a glass waveguide). Finally, they only work with low loss modes where the propagation constant in the waveguide is nearly that of free space. For the fused silica waveguides of interest, the lowest loss modes are the hybrid EH_{nm} modes. Although these modes have a longitudinal component to the electric field of the propagating wave, its magnitude is small compared to the transverse fields, so the modes are essentially

transverse. Their electric field profile as a function of the radial direction is given approximately by

$$E(r) = J_{n-1}\left(\frac{\mu_{nm} r}{a}\right) \tag{4.1}$$

where J_{n-1} is a Bessel function of the $(n-1)$ kind, μ_{nm} is the m^{th} root of the equation $J_{n-1}(\mu_{nm}) = 0$, r is the radial coordinate, and a is the radius of the waveguide's inner bore [50].

In most of the calculations for phase matching and other aspects of high harmonic generation, the lowest loss EH_{11} mode is assumed. However, a significant amount of power can also be coupled into some of the higher-order modes, and these modes can have a significant effect on the high harmonic process. In particular, these higher order modes have distinct phase and group velocities, and can beat against the fundamental mode. An example simulation of this situation is shown in Figure 4.1. In general, it would be ideal to avoid mode beating during the HHG process, as it will suppress the intensity of our driving laser at various points along the guide. However, several authors have suggested that under the right conditions, mode beating could be used as a QPM scheme [46, 52].

4.2.2 Attenuation and Bending Losses

Marcatili and Schmeltzer also quantify the attenuation along the waveguide. They give the attenuation constant α_{nm} as

$$\alpha_{nm} = \left(\frac{\mu_{nm}}{2\pi}\right)^2 \frac{\lambda^2}{a^3} \mathrm{Re}\left[\frac{1}{2}\frac{(\nu^2+1)}{(\nu^2-1)^{\frac{1}{2}}}\right] \tag{4.2}$$

where λ is the wavelength of the radiation traveling down the hollow core of the waveguide, and ν is the ratio of the indices of refraction of the guide material and the gas filling the guide. For our case, fused silica has an index of refraction of 1.45, and the core of the guide will have an index of refraction very near to 1 [42]. For a coupled wavelength of 800 nm in a 150 μm inner diameter fused silica waveguide, α_{11} works

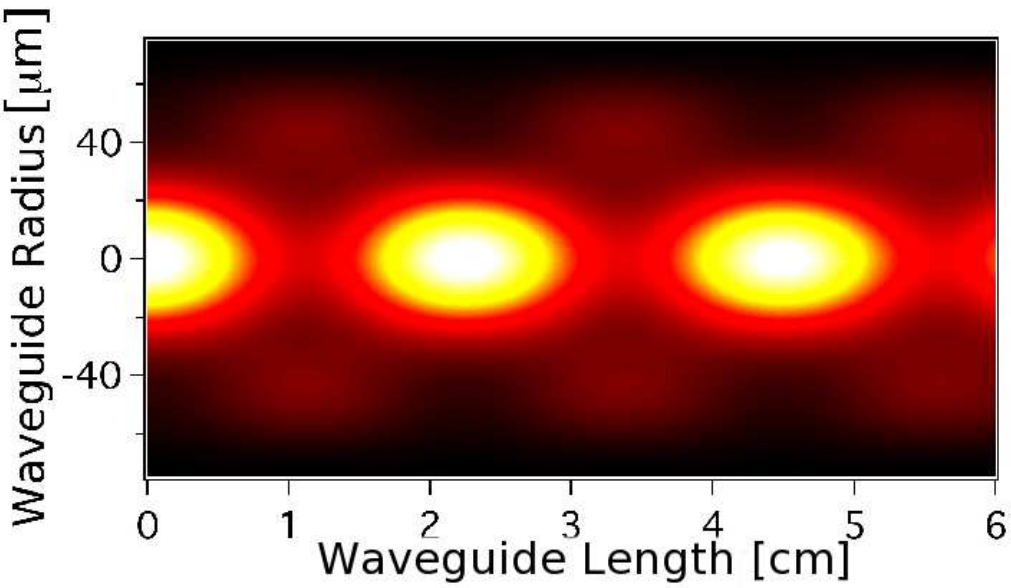

Figure 4.1: A simulation by Amy Lytle of mode beating between equal contributions of the EH_{11} and EH_{12} modes within a hollow waveguide. Note that the beating has an approximately 2 cm period. A similar period is experimentally observed in the form of periodic variation of plasma emission intensity along a hollow waveguide in which gas is being ionized by a driving laser used for HHG

out to be 0.33 m^{-1}. So for our typical 10 cm waveguides, we should have roughly 3% attenuation for the lowest loss EH_{11} mode.

Furthermore, the loss due to bending of the waveguide can be given in terms of the radius of curvature which doubles the straight guide attenuation, labeled R_0. For the EH_{1m} modes

$$R_0 = \frac{2}{\sqrt{3}} \left(\frac{2\pi}{\mu_{1m}}\right)^2 \frac{a^3}{\lambda^2} \left[1 + \frac{1}{\mu_{1m}^2} + \frac{3}{4}\frac{(\nu^2-1)}{(\nu^2+1)} \cos 2\theta_0\right]^{\frac{1}{2}} \tag{4.3}$$

where θ_0 corresponds to the orientation of the field polarization with respect to the curvature of the waveguide. For $\theta_0 = 0$ the field at the waveguide's center is in the plane of curvature and the attenuation is maximum. Similarly, the attenuation will be a minimum when the polarization is perpendicular to the plane of curvature [50]. So, for bending losses, we should notice several key points: the higher order modes are less sensitive to bending loss, the bending losses decrease dramatically for decreasing inner diameter, and the bending loss is sensitive to the polarization of the coupled mode. For example, for an EH_{11} mode at 800 nm wavelength in the maximum attenuation polarization, and with a 150 μm inner diameter fused silica waveguide, the bend radius the bend radius that results in a bending loss equal to the intrinsic EH_{11} loss is 6.2 m. Thus, waveguides should be held as straight as possible to minimize bending. Interestingly though, if loss of lower order modes becomes desirable, inducing a bend may prove to be an interesting way of tuning the loss.

4.2.3 Coupling

Coupling the lowest loss EH_{11} mode efficiently into a hollow waveguide requires a combination of the correct focal spot size and a mechanical system with the precision and sufficient degrees of freedom to align the guide. Abrams calculated that optimum coupling of a TEM_{00} free space mode of the laser to the EH_{11} mode of the guide is given

by

$$\omega_0 = 0.6435a \tag{4.4}$$

where ω_0 is the radius of the free space beam at its focus, and a is the radius of the waveguide. In theory, when this coupling condition is met, 98% of the energy from the TEM_{00} mode will couple into the EH_{11} mode of the waveguide [51]. As the focal spot size deviates from this condition, more energy will go into the lossier modes of the waveguide. Ideally, the driving laser should have a collimated free space beam, and the focusing lens focal length is chosen to meet the condition of Equation 4.5. This way, the lens can be translated parallel to the propagation direction of the laser and change the focal spot position without changing its size. For a collimated driving laser beam of diameter D_{col}, and wavelength λ_0, the lens focal length f will be given by,

$$f = 0.6435\frac{\pi a D_{col}}{2\lambda_0} \tag{4.5}$$

In general, we find that the most successful method for coupling into a hollow waveguide is to position the waveguide to the laser beam, not the laser beam to the waveguide. Usually this alignment is accomplished by noting the path of the laser beam before introducing the waveguide, and then, after inserting the waveguide, adjusting the waveguide alignment until the beam path is unaltered by the waveguide and emerges with a clean spatial mode. Next, the coupling can be optimized using a power measurement and iterative adjustment of focal spot position and waveguide alignment (moving the focal spot invariably steers the laser beam slightly). This approach requires that the waveguide be held in such a way as to allow it 4 degrees of freedom, and that the coupling optic can be translated parallel to the beam propagation direction. Although the waveguide could be placed on a single stage that included horizontal and vertical adjustment, along with azimuthal and planar rotation, we use a much simpler system of placing a vertical and horizontal adjustment at each end of the waveguide. In general, adjustments at the front of the waveguide (since they are the most critical to the

coupling) are used to maximize the power, while the rear adjustments determine the pointing and mode quality of the laser beam emerging from the waveguide. In addition, once the alignment has been optimized, if the rear adjustment is left undisturbed, small corrections to the front of the waveguide to correct for laser pointing drift will not appreciably alter the beam pointing emerging from the waveguide for most experiments. Finally, for the 150 μm inner diameter waveguides we use, the positioning must be done to better than 10 μm for optimum results.

4.3 Modifications to the Hollow Waveguide Design

4.3.1 Why Change the Design?

During my work with modulated waveguides, I became highly interested in ways in which we could improve the consistency and quality of our 3-section hollow waveguides. In terms of consistency, the coupling efficiency of laser light and the output mode quality of the original 3-section design varies substantially. Considering that one of our main goals remains enhancing the flux of EUV, especially at shorter wavelengths, I wanted to start with an optimized unmodulated capillary and be sure that we were able to quantify enhancements in a fair and repeatable manner. Making and assembling the components of the original design in a precise, consistent, and repeatable manner requires a great deal of practice and patience. Outer capillaries are easily broken during the drilling process, and the sanding and handling of individually cleaved inner capillary end pieces must be accomplished with a set of forceps and a steady gentle hand.

The final assembly of the optical-quality inner sections into the outer-capillary fixture presents its own set of difficulties. Sliding the inner capillary pieces into the tight fitting outer capillary can easily break or chip the inner components, while an overzealous application of epoxy can foul the assembly. Of course, maintaining the position of the inner components while jabbing epoxy into the gluing holes can be

a tricky endeavor as well. Furthermore, the outer capillaries are fragile and relatively expensive. Once the inner pieces are glued into place, the outer capillary is not reusable. Therefore, the assembly's effective lifetime depends either on how long the inner capillary survives laser damage or the amount of time before the assembly is stressed and cracked during alignment. Unfortunately, waveguides seem to preferentially expire at moments when they are most needed, so the experimenter must have a backup, or be left waiting many hours for glue to dry.

4.3.2 Initial Hollow Waveguide Improvement Attempts

I began this improvement project by upgrading the manufacture and interchangeability of the outer-capillary fixture. Originally, separate members of the group would produce the radial holes in the fixture using a laborious glass drilling process. To make the quality and consistency of the outer capillaries better, as well as to increase the efficiency of production, I had a local technical glass company ultrasonically mill the holes for us. In this process, a milling tool cuts the three holes at each end of the capillary simultaneously, keeping a precise relationship between the positions of the holes relative to the capillary ends. Next, I turned my attention to the inner-capillary pieces. Originally, separate members of the group would cleave their own end pieces, sand them, and then glue them in place, leaving substantial variability in the size and placement of the end pieces. I developed a procedure to produce and place the inner capillary end pieces. I waxed many pieces of inner capillary together, and cut them simultaneously on a wet saw while using a carefully-measured stop to maintain a length of 5 mm for all batches. Now that the outer capillaries were all made to the same dimensions, the central inner capillary could be centered between the gas feedthrough holes. After the central inner capillary was placed, I used a specially made depth gauge to place the end pieces so that they maintained a 0.5 mm gap from the ends of the central piece.

Although these various improvements greatly facilitated the production of the

3-section waveguides, the coupling efficiency and output modes remained inconsistent and sometimes unsatisfactory. Endeavoring to solve these problems lead me to novel ways of producing the 3-section inner capillary, and eventually a complete redesign of 3-section hollow waveguide assembly.

4.3.3 Single-Piece Inner Capillary Hollow Waveguides

Having the inner capillary split into three separate sections allows for simple gas feedthroughs and differential pumping, but we grew concerned that this arrangement was leading to misalignment and unnecessary coupling losses. The gaps between the end pieces and the central piece clearly cause coupling loss, as evidenced by the scattering of laser light. In addition, since the outer capillary's inner diameter is not a perfect fit to the inner capillary, we were concernced that the end sections might be slightly tilted so that all three capillary pieces did not share a common axis. Nick Wagner cleverly realized that we could make a 3-section waveguide from a single piece of inner capillary by partially slicing through the capillary wall with a wet saw. He initially attempted this procedure by hand; first, by marking the inner capillary with a sharpie at the positions to be slotted, and then holding the capillary gently to the wet saw blade. Although some capillary attrition inevitably occurred, the basic idea was a success. A single-piece inner capillary greatly simplifies the production and assembly of hollow waveguides. To facilitate this manufacturing technique, I quickly designed and machined jigs for holding multiple inner capillaries so that they could be slotted and trimmed simultaneously using a surface grinder. This set-up represented another major step forward in improving the hollow waveguide assembly process. The number of major components had now been reduced to 2, and the length of the inner capillary, as well as the size and depth of the slots, could be precisely set with the surface grinder.

A 3-dimensional rendering of one end of the slotted single piece inner capillary is shown in Figure 4.2. The slot is $\frac{1}{32}$ of an inch wide and made with a diamond

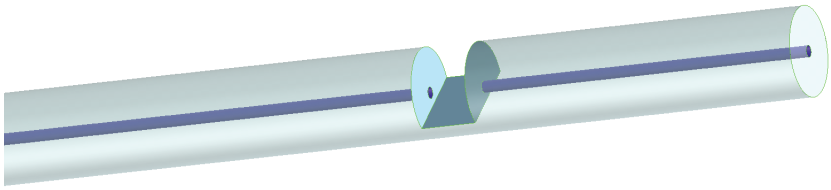

Figure 4.2: To-scale 3-d rendering of the slotted innner capillary

wet saw. Although slotting the inner capillary allows for a single-piece implementation, the mechanical process of cutting the slot can make fine chips in the capillary, as seen in the microscope image of Figure 4.3. The mechanically-made slots did represent a step forward, but the resulting chipping and roughness produced less-than-ideal laser transmission. The output mode, which refers to the mode structure of the laser beam emerging from the output of the capillary, for these slotted capillaries was better overall than with past designs. However, the intense fs amplified laser was producing white light at the face of the slots, suggesting unwanted nonlinear interactions with the capillary material. After considering several ideas for mechanically polishing the slots, my advisor, Prof. Henry Kapteyn, made the critical suggestion that perhaps instead of abrasively cutting the gas feedthrough in the inner capillary, I might be able to efficiently produce a smooth hole by using the CO_2 laser set-up I had developed for modulating waveguides. When tightly focused at near full power, the CO_2 laser ablates fused silica as well as delivering heat, allowing it to 'drill' a smooth hole as shown in Figure 4.4. One of the key elements of the existing CO_2 laser glass-working set-up is its

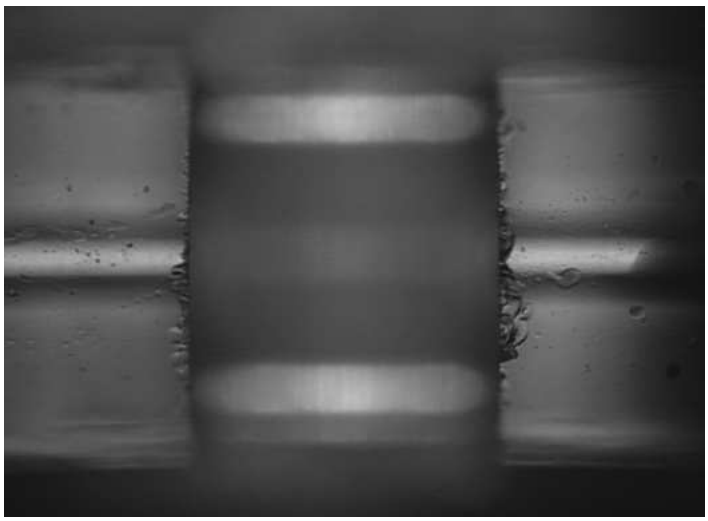

Figure 4.3: Microscope image of an abrasively cut slot

ability to pressurize the capillary with inert nitrogen gas. As the focused laser reaches the inner wall of the capillary tube and the viscosity of the fused silica drops sufficiently due to heating, the pressure forces the remaining wall radially outwards. Therefore, no molten ablated fused silica debris gets lodged on the inner wall of the capillary. I found that a careful balance of focal spot size, laser power, gas pressure, and exposure time produces beautiful radial holes in the capillary. The focal spot size determines the size of the hole, and a $\sim 100\ \mu m$ diameter spot works well. The laser power must be high enough to ablate material, and the optimum power corresponds to a range where it also fire polishes the hole; typically 6 W (65% duty cycle for the CO_2 laser). The capillary internal pressure was set to 15 psi. Although the gas pressure is not exceedingly critical, a gas pressure that is too high pushes the internal wall outwards too soon, leading to a constriction rather than a subtly tapered hole. As for laser exposure time, too short of an exposure time obviously does not allow the laser to penetrate the capillary wall, while too long of an exposure time causes damage to the other side of the inner wall. An exposure time of around 2 s generally works well with the above parameters, making the process quick and efficient. When the capillary is heated by the laser, it glows a bright

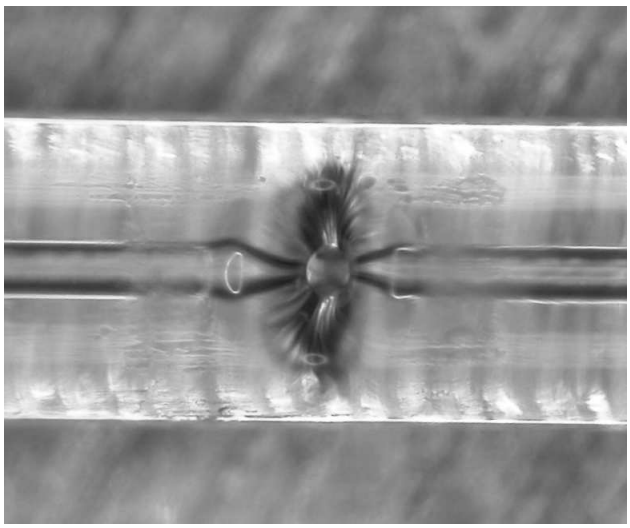

Figure 4.4: Stereoscope image of a laser poked hole

white. However, when the laser penetrates to the inner wall, the pressurized gas flows from the hole. The outward flowing gas cools the capillary, which causes the glowing to dim. This change provides a quick feedback for rough adjustment of the exposure time, but I make the final adjustments by inspecting the holes under a microscope.

As an important side note, I also investigated improved methods for cleaning the inner capillaries. Since the inner capillary ends must be sanded to obtain the best mode and simplify the laser coupling process, small fused silica particles inevitably enter the inner bore. These particles, especially larger ones, are quite pernicious and difficult to remove. Moreover, they can cause massive transmission loss, improper gas flow, and mode corruption. In the past, the generally-accepted method was to spray methanol into the capillary and use an air jet to blow it out over and over again until the capillary had been cleaned. This method was laborious, and often failed to remove lodged particles. The next step was to take a piece of fine wire slightly smaller than the inner bore and use it to push out any unwanted debris. This method also proved neither an easy nor enjoyable task, requiring a steady hand (putting fine wire into a 150 μm diameter hole is *considerably* more difficult than threading a needle). Discussions with

Hans Greene of the JILA instrument shop lead me to try using an ultrasonic cleaner. This method turned out to be a tremendously effective, reliable, and simple solution to the cleaning dilemma. The capillaries are placed in the ultrasonic cleaner for several minutes in an upright position so that debris that is shaken loose falls out of the bottom end, then rinsed with filtered water and blown out. After cleaning in this manner, the inner capillaries show no signs of debris, either when inspected under a microscope, or by coupling a HeNe laser into the capillary and looking for scattering.

4.3.4 V-groove Fixture for Single-Piece Hollow Waveguides

Improvements to the outer and inner capillary components of the hollow waveguide assembly greatly improved their utility and uniformity. However, the inconsistency in transmission and output mode (though ameliorated) continued. The need for a revolutionary design became apparent when Arvinder Sandhu, a post-doc in our group, was having great difficulty getting good coupling or decent modes from a 1 m long hollow waveguide that he wished to use for self-phase-modulation and pulse compression. In trying to determine the nature of the problem, we decided to test the straightness of the outer holding capillary. For a cylindrical object, a simple first test is to roll the object back and forth on a surface plate. While rolling the object, one looks for any gaps between the object and the surface plate as well as watching the ends of the object for any run out. Interestingly enough, although the outer capillary is extremely straight, Arvinder and I noticed that the inner bore of the capillary appeared not to maintain a constant position with respect to the axis of the tube.

The outer capillary material is known as *precision bore tubing*, and because of its dimensions and the aspect ratio of its inner and outer diameters, it is not manufactured by the traditional methods of draw towers. Precision bore tubing is made by melting a piece of thick-walled glass tubing and pulling it over a precision mandrel made of highly polished solid metal. Thus, the surface quality of the metal rod determines the surface

quality of the inner bore of the capillary. Moreover, when the thermal expansion of the metal has been taken into account, the inner diameter of the capillary is extremely accurate to tolerances better than 0.001". The outer surface of precision bore tubing is ground and polished, leaving it very straight and round. Unfortunately, the process of making precision bore tubing does not in general provide reliable concentricity of the outer and inner diameters of the tube. Thus, the inner diameter can "snake" through the tube. For our applications this bending constitutes a highly undesirable feature. It distorts the inner capillary tube through which the laser is coupled and must travel, leading to unwanted attenuation and mode corruption. This discovery, though suggesting a clear path to fixing the nagging inconsistencies of the 3-section design, was somewhat disheartening since the problem of bending induced by the outer capillary fixture seems so glaring in retrospect.

A complete redesign of the 3-stage hollow waveguide assembly presented a major mechanical and experimental challenge, particularly in devising appropriate gas seals. Kinematically speaking, a v-groove beneath and a line contact above represents the ideal geometry for holding a long cylindrical object in a straight and unstressed manner. Ironically, the original work demonstrating pulse compression in hollow waveguides also emphasized the use of a very straight v-groove [49]. The design presented here was created with the invaluable help and expertise of Tracy Keep in the JILA instrument shop. My goals were simple; create a robust, modular, and flexible fixture that guaranteed the straightness of the inner capillary (from now on to be referred to simply as *the capillary*). Prototyping and perfecting this design consumed many months, but it continues to make a lasting contribution to our research as well as allowing exciting possibilities for HHG.

A 3-dimensional exploded rendering of the v-groove fixture is displayed in Figure 4.5 and a picture of an assembled fixture appears in Figure 4.6. This assembly completely eliminates the outer precision bore tubing fixture. The assembly consists of a

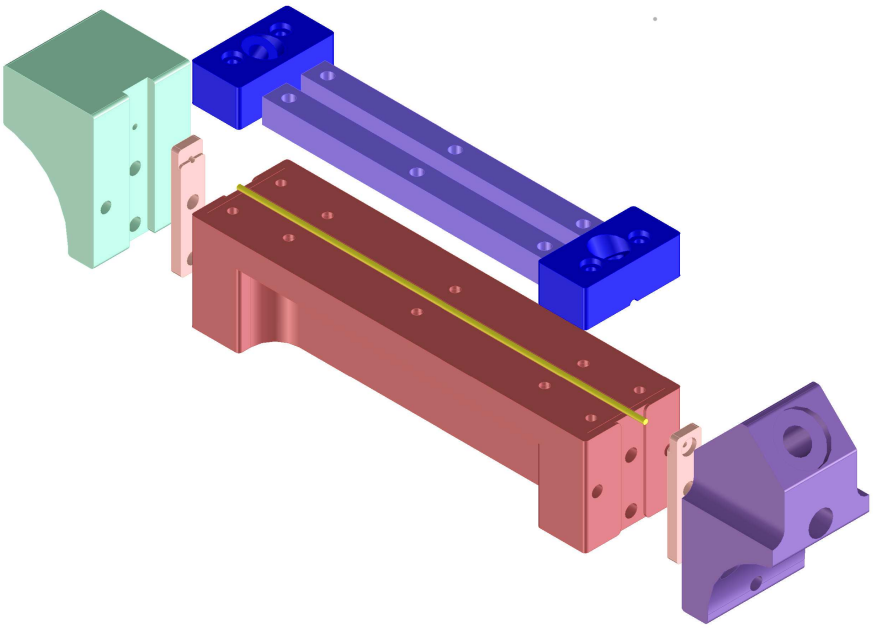

Figure 4.5: A 3-d exploded rendering of the v-groove fixture

Figure 4.6: An assembled v-groove fixture

v-grooved bar with an o-ring holder and end piece on each end, blocks for feeding gas into the capillary, and hold-down bars for securing a clear plastic cover for the capillary. The v-groove bar is a single piece of aluminum machined into a half I-beam configuration to reduce weight but maintain stiffness. The v-groove itself is machined into the bar as the final machining operation to prevent warping or bowing of the groove.

The components attached to the v-groove bar form gas and vacuum seals to the capillary, as well as providing proper seating in the groove. The o-ring holders have seats for an 002 size o-ring that forms the vacuum seal on the ends of the capillary. Silicone o-rings must be used to withstand the heat dissipated into the capillary from the coupled laser. The o-rings are compressed between the end pieces and the o-ring holder so that they seat onto the capillary's outside wall and form a tight seal that does not require vacuum grease. Additionally, this design allows an inspection window to be placed in the end piece that aids with coupling the driving laser into the capillary. However, the ends of the capillary must be beveled to prevent cuts in the sealing o-ring during assembly. A custom-made silicone gasket forms the gas seal to the laser-drilled holes on top of the capillary. At first, I tried using a standard o-ring. Unfortunately, to squeeze an o-ring onto the cylindrical surface of the capillary required too much load, resulting in an unreliable seal as well as deformation and occasional fracturing of the capillary. A 3-dimensional rendering of the gasket is shown in Figure 4.7. The large

Figure 4.7: A 3-dimensional rendering of the custom silicone gasket

surface area and conforming shape of the gasket allow it to create a reliable gas seal with minimal stress on the capillary. I make this gasket from silicone tubing that has an inner diameter that closely matches the outer diameter of the capillary. Using a razor blade, I slice a short length of tubing axially in half, and then use a piece of 17 gauge hypodermic tubing sharpened at one end as a gasket punch to cut the gas feedthrough hole (a thick piece of paper such as an old punch card forms an excellent backing during the hole punching operation). Using a spare gas block as a fixture, I align the gas feedthrough hole in the gasket with its counterpart on the bottom of the gas block and trim the half-cylinder gasket to length with a razor blade. The gas block and gasket together hold the capillary firmly in place at the ends of the fixture, but the capillary must be held in tight contact with the v-groove along its entire length to avoid bowing. I use a sheet of clear plastic cut from a $\frac{1}{2}$" diameter piece of Tygon® tubing to hold the capillary in place. Much like the silicone gasket, I slice the Tygon® tubing axially and then cut it to size, placing it on the capillary such that the Tygon® sheet curves away from the v-groove bar and must be pulled down over the capillary using the two hold-down bars. The end pieces each hold a $\frac{1}{4}$" thin walled stainless steel tube that forms the vacuum connection to Ultra-Torr® fittings.

The v-groove fixture possesses several distinct advantages over the outer capillary fixture, particularly in the configurability of its components. Not being made of a fragile material, the v-groove fixture is quite robust. Since the older outer capillary design employed Ultra-Torr® tee fittings to create the gas seal, large portions of the capillary were not visible, especially the capillary entrance. Being able to view the front of the capillary greatly simplifies the coupling and alignment procedure, while being able to view the length of the capillary allows one to clearly see the plasma created by the driving laser. Maximizing the light emission from this plasma often allows a rough optimization of the EUV flux, and noting the color of the plasma aids in troubleshooting contamination of the gas system. Furthermore, since the stainless tubes

on each end are thin walled, they have a much better conductance for pumping than the outer capillary. Residual gas at the capillary entrance can cause undesirable ionization losses and plasma-induced defocusing of the laser beam that leads to decreased coupling efficiency and mode corruption. The design of the v-groove fixture is also extremely flexible. We have made v-groove bars as long as 1 m and as short as 0.5 cm. The shortest bars have a single gas feedthrough, but I have also made a 10 cm fixture with 5 gas feedthroughs. Although the silicone gaskets must occasionally be replaced when changing the capillary, and the o-rings are disposed of with each capillary replacement, all other components of the v-groove fixture are completely reusable, saving long term cost. Moreover, a laser-damaged capillary can easily be replaced within 10 minutes yielding consistent results results consistent with the previous capillary, saving valuable time, and providing peace of mind.

4.3.5 Simple Set-up for Comparing Transmission of Hollow Waveguides with a Spatially-Filtered HeNe Laser

As I began to work more with hollow waveguides and improve their performance, I became interested in making a careful and repeatable measurement of their throughput under near-perfect coupling conditions. Being able to compare waveguides in this manner allows us to make determinations of waveguide quality between various manufacturers, understand better the effect of different fixturing designs, evaluate the effect of waveguide modifications, and ideally understand and tune the mode structure within the waveguide. My goal was to make a reliable measurement within a 1%-2% uncertainty. However, after realizing that precise power measurement at low powers can be a tricky endeavor, I consulted with Nobel Laureate Jan Hall who has tremendous expertise in perfecting such measurements. The set-up described here reflects several extremely insightful suggestions by Jan. Specifically passive optical isolation, a reference arm for monitoring power fluctuations, and tips for the use of sensitive photodiodes. The set-up

is shown schematically in Figure 4.8. Having a stable light source in terms of power and high quality mode represents the first step in making a reliable transmission measurement. The HeNe laser gives a polarized output of around 4 mW and is held in a custom-machined Delrin® block for stability. Jan mentioned that HeNe lasers are particulary susceptible to power fluctuations from back reflections that return to the laser cavity and incite erratic feedback and mode hopping. So, the first several optics and their alignment was suggested by Jan to minimize this undesirable effect. The HeNe laser beam immediately goes through a linear polarizer (P) set at the output beam polarization, and then a quarter-wave plate (WP). Together these two optical elements form a passive optical isolator. As the beam passes through the quarter-wave plate it becomes circularly polarized. Any back reflections after this point must once again traverse the quarter-wave plate, and in turn regain linear polarization. However, the effect of going through the quarter-wave plate twice will cause the back reflected light to be rotated by 90° to the original polarization state, and thus, it is rejected by the initial polarizer. To further protect against back reflections, the polarizer and quarter-wave plate are set at an angle deviating from the normal to the beam path such that the back reflected light misses the HeNe laser output coupler. Still, for best results, the HeNe laser should be given 30 minutes or so of warmup time to allow for thermal equilibrium.

The rest of the set-up ensures a high quality mode and proper coupling conditions, as well as providing a reference arm to monitor power fluctuations and establish a transmission measurement without moving the waveguide or detector. After the optical oscillator, the beam passes through a spatial filter (SF, Newport model 900 Spatial Filter) to ensure a near-perfect TEM_{00} Gaussian mode. Two lenses (L1 and L2) mounted on linear translation stages serve as a telescope to collimate the beam to an adjustable beam diameter, depending on the desired coupling conditions for the waveguide. The iris immediately following this telescope (I1) eliminates the residual high order modes left from spatial filtering. The next two mirrors (M1,M2) allow alignment of the reference

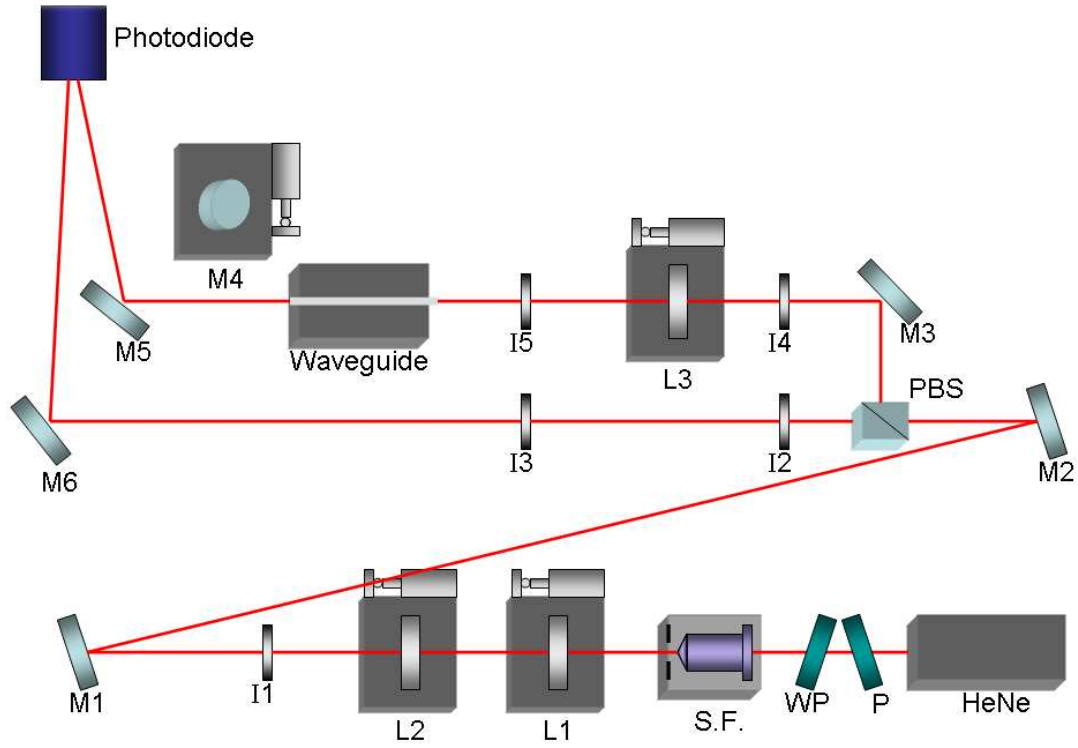

Figure 4.8: A schematic of the set-up for testing waveguide transmission. P: polarizer, WP: quarter-wave plate, S.F.: spatial filter, L1-L3: 7.5 cm, 10 cm, and 50 cm focal length plano-convex AR coated lenses respectivley, I1-I5: irises, M1-M6: silver mirrors, PBS: polarizing beam splitter cube.

arm. Since the light is circularly polarized after the quarter-wave plate following the HeNe laser, it is evenly split when it encounters the 50/50 polarizing beam splitter cube (PBS). This cube itself and a mirror (M3) allow alignment of the waveguide testing arm. Although different lenses can be used for focusing into the waveguides, the set-up is currently optimized for 150 μm inner diameter waveguides using a 50 cm focal length lens (L3) mounted on a linear translation stage. The beam size and mode quality at the focus of the 50 cm lens are diagnosed using a CCD camera. Since the beam going into the focusing lens (L3) is collimated, the lens can be adjusted to optimize coupling without changing the focal spot characteristics. To ensure the alignment of both the testing and reference arm, a collared iris can be placed in mounts at four positions along the beam paths (I2-I5). The waveguide to be tested sits in a v-groove held on a stage that provides vertical and horizontal positioning perpendicular to the beam propagation direction, as well as tilt and rotation adjustment. The front end of the waveguide sits referenced to the front end of the v-groove for repeatable placement. To properly align the waveguide, a 45° turning mirror (M4) can be translated into the beam path where it redirects the laser light to the bottom of a shelf above the set-up. This mirror is placed in the beam before the waveguide is put into place, and the position of the beam is carefully marked. A poorly-coupled waveguide will steer the incident HeNe laser beam from its original path as well as exhibit high order output modes. So, once some light can be seen coming through the waveguide, careful adjustments are made to the waveguide position and orientation so that the beam returns to its original position with a good mode. Two final mirrors (M5, M6), guide the beams from the testing and reference arm onto the power detector (Newport 818-UV measured with Newport 1825-C power meter).

With the set-up properly aligned, making a power measurement becomes straightforward. A large area photodiode acts as the power detector. The photodiode was tested to verify that the detection characteristics across its surface were homogeneous, and it

is positioned such that the reference and test arm beams impinge on its surface with approximately equal sizes. The photodiode is very sensitive, and will give varying measurements if moved or tilted with respect to the beam. Therefore, a mount firmly locks the photodiode in place, and it is not disturbed during the measurement. To increase the accuracy of the measurement, I custom made a filter holder for the photodiode and fitted it with a HeNe laser notch filter. This filter rejects all light with wavelength outside the range of 633±2 nm. Since the photodiode is optimized for low power measurements, even reflections of room light from a hand or shirt can alter the measurement without this filter in place. Furthermore, following a suggestion from Jan, the filter holder is shiny aluminum to reduce IR background on the photodiode. Without the waveguide in place, a ratio can easily be established between the power throughput of the measurement arm and the reference arm that naturally takes into account all losses. Since only a relative measurement is desired, with the waveguide in place and aligned, the arms can be alternately blocked and power measurements taken. Double-checking the reference arm ensures that the power has not fluctuated during the measurement and allows a transmission measurement without moving the waveguide or the detector. Finally, a CCD camera can be inserted at the waveguide output to record the output mode structure and quality.

This transmission measurement apparatus had been for the most part a side project, but I was lucky enough to have an extremely talented and meticulous visiting student, Steffen Haedrich, complete some waveguide characterization experiments for me. Steffen came from the University of Jena in Germany, home of optics legends Carl Zeiss and Ernst Abbe, so he was well acquainted with precise optical measurements. He perfected the mode quality of the coupled beam, as well as carefully setting its size to the optimum of 0.64 times the waveguide diameter for introducing the lowest loss mode [51]. I first requested that he compare the transmission of waveguides cut from the capillary stock of 2 different suppliers, as we had long been curious if either man-

ufacturer produced better quality products. He quickly determined that no significant statistical difference appeared between the two manufacturers. So, I had him quantify the difference in transmission between several waveguide configurations. Figure 4.9 shows a comparison of 10 cm waveguides (meaning 11 cm total length, since we usually have 5 mm end sections) resting in the v-groove to those held in an outer-capillary fixture. Waveguides 1-8 had no laser-poked holes. They were first measured resting in the v-groove and then remeasured held in different outer-capillary fixtures. This data exhibits a nearly 10% lower average transmission for the outer capillary fixture, as well as illustrating the inconsistency inherent in that design, as indicated by the standard deviation. Figure 4.10 compares 2 sets of 10 cm waveguides resting in a v-groove, those without any modifications and those with a laser-poked hole at each end. This data shows that only a small loss of transmission occurs with the laser-poked hole modification. To further understand the waveguide laser coupling issues, Steffen captured images of the output mode from the waveguides placed in various configurations with a CCD camera. A very relevant example for work presented later in this thesis on imaging with coherent EUV light, shows the mode corruption induced with the old outer capillary fixture. Figure 4.11 shows the output modes of three different waveguides when resting in a v-groove (top) and the output modes of the same waveguides placed in three different outer capillary fixtures (bottom). Clearly, this data emphasizes the need for a consistent and reliable fixture for maintaining EUV mode quality. Hopefully this setup will be used for future transmission measurements and mode comparisons as new waveguide configurations come into use. It should also be helpful if tuning the coupling conditions and waveguide configurations to a specific set of waveguide modes arouses more interest, as has been suggested as a QPM scheme [47].

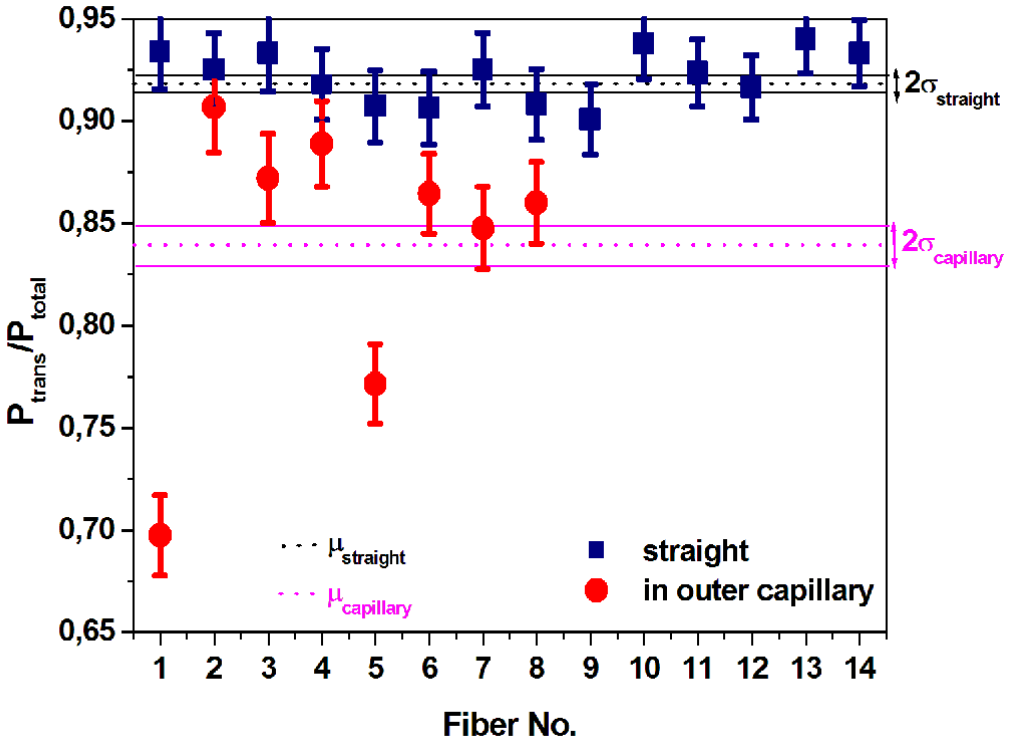

Figure 4.9: A measurement of transmitted power for 10 cm waveguides comparing those resting in a v-groove with those held in an outer-capillary fixture

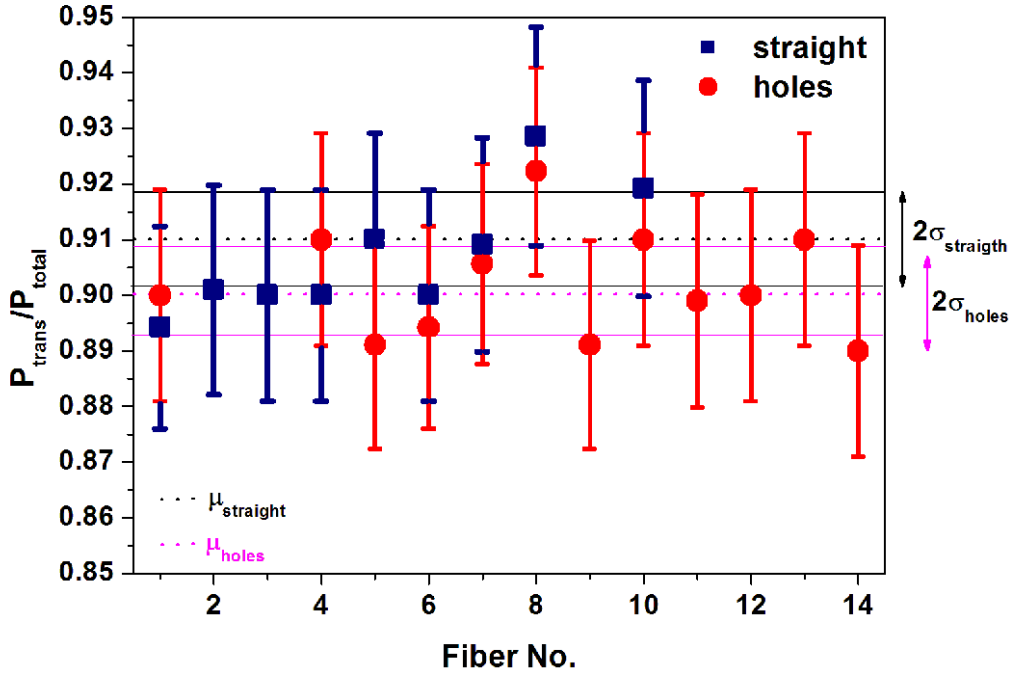

Figure 4.10: A measurement of transmitted power for 10 cm waveguides resting in a v-groove without holes versus those with 2 laser-poked holes

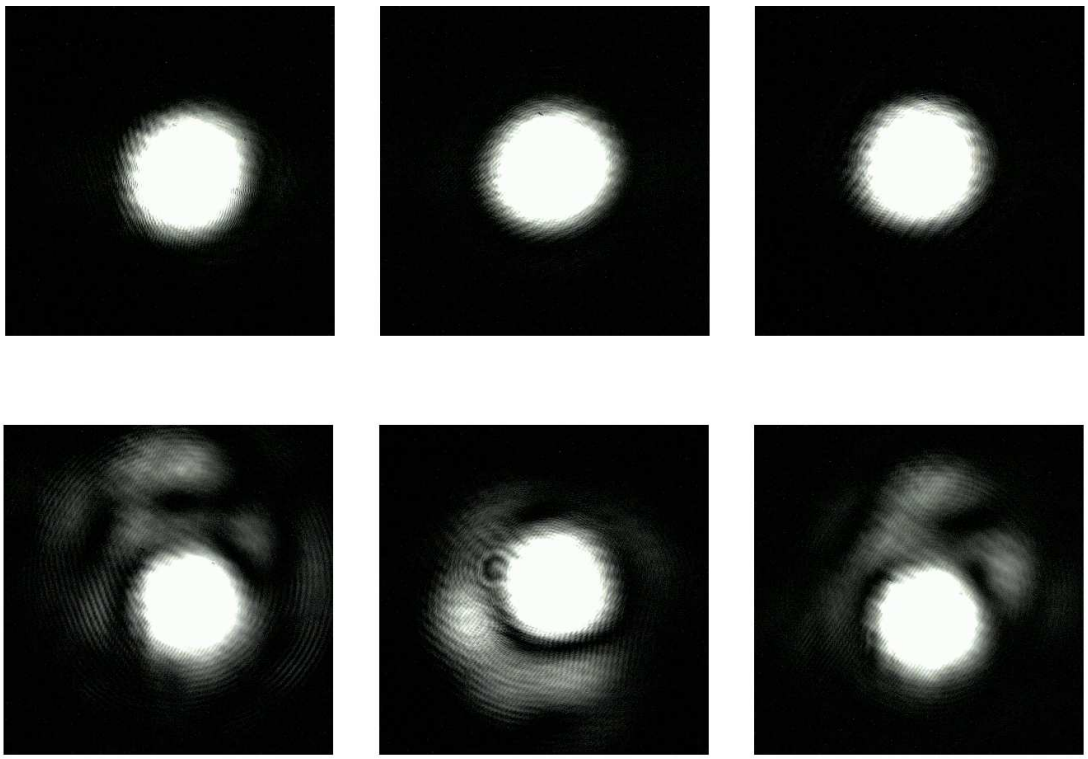

Figure 4.11: An example of the comparison of the output modes for three different waveguides placed in a v-groove (top) and the corresponding waveguides held in an outer capillary fixture (bottom)

4.4 Future Directions

Several interesting possibilities exist for future work using the v-groove fixture design with 3-section laser drilled capillaries. Perhaps most straightforwardly, this fixture will allows us to perform HHG in very long waveguides, which may be useful for high flux applications requiring low pressure gasses with low absorption at the wavelength of interest. Another exciting possibility will be a 2-stage waveguide arrangement, in which a different gas is used in each stage. Whereas the traditional arrangement for compressing amplified fs pulses calls for a self-phase modulation (SPM) cell followed by carefully chosen and aligned chirped mirrors, previous work in our group has shown that under certain conditions, a short hollow waveguide filled with Ar can efficiently self-compress these pulses to shorter time durations [53, 54]. Ideally, the first section of the 2-stage waveguide would be filled with Ar to compress the driving laser pulse, and the second section would be filled with Ne or He, which with their large ionization potentials can produce the highest energy harmonics. Such an arrangement promises the possibility of a high quality mode of a very short pulse duration ($\sim$ 10 fs) with extremely straightforward coupling into the second stage. We attempted a 2-stage waveguide in the past, but with disruptions due to the gas inlets, the outer capillary fixture design had an unacceptably poor transmission and output mode. I have already designed and built such a 2-stage waveguide with the v-groove fixture, and it exhibits good transmission characteristics despite having 5 laser poked holes in an 11 cm overall length. However, it has not yet been tested for its original purpose of HHG with self-compressed pulses. Ironically, although I designed the v-groove fixture with the straightness of the waveguide as the main consideration, a well-defined and tunable bend may actually be of interest. Recent experiments suggests that mode-beating within the waveguide can be used as a QPM scheme [46,52]. In this work, the authors rely on coupling conditions to launch high order modes. High order modes are more lossy than low order modes in

a hollow waveguide. However, high order modes are actually less susceptible to bending losses than lower order modes. Therefore, a tunable bend could be used to adjust the ratio of high and low order modes, and optimize the mode beating QPM. As for the capillary itself, a tapered end section might form a useful modification leading to longer capillary lifetimes, and should also be useful for high gas pressures where larger gas flows and bigger conductances are beneficial. I believe such an end section could be easily and reliably made in much the same way the laser drilled holes are formed in the capillary. Although such a task would require delicate and repeatable alignment and placement of the capillary, I believe it is well within the limits of laboratory precision.

Chapter 5

Coherent Imaging in the Extreme Ultraviolet

5.1 Introduction

The development of novel light sources,such as the monumental invention of the light bulb and the x-ray tube, has spurred major advancements in our ability to image the natural world in both the macroscopic and microscopic realms. Recently, coherent laser light sources have played an important role in extending the utility of the microscope. Coherent light sources make possible spectacular new imaging techniques such as laser scanning confocal microscopy, holography, and laser tweezers. The coherent EUV light generated using HHG performed in a hollow waveguide is a relatively unique light source as it exhibits near-perfect coherence at a range of short wavelengths in the EUV [55]. Considering the uniqueness of this source, and its wavelength of operation, we wished to demonstrate a suitable imaging technique.

Although established microscopy techniques are already exceedingly capable at imaging on micron and sub-micron length scales, high-resolution imaging (i.e. nanometer-scale) of 'thick' samples remains an outstanding problem in imaging. Using innovative imaging and labeling techniques, far-field light microscopes can image living cells with a resolution as high as 200 nm [56]. Of course, this resolution is fundamentally limited by the wavelength of the visible/near-UV light. Using the much shorter wavelengths of moderate-energy electrons to surpass the diffraction limit of optical microscopy, electron microscopy has demonstrated resolution at the atomic level [57]. However, many bio-

logical specimens, as well as samples of interest for materials science, are too thick for electron microscopy. Inelastic scattering of electrons changes their wavelength, leading to image blur. In addition, the phase contrast information of the electrons is decreased by plural elastic scattering, but this information forms the primary image contrast mechanism for electron microscopes. These effects are especially prevalent in 'thick' samples, and limit electron microscopes to imaging thin samples, typically < 500 nm [58]. Thus, a resolution gap exists between optical microscopes and electron microscopes; optical microscopes can view thick specimens with an excellent depth of field but limited resolution, whereas electron microscopes have excellent resolution but are not suitable for thick samples. Especially in the realm of biology, this resolution gap obscures some of the most important and exciting mysteries of life and its development; examples include internal cell features, morphology and architecture of groups of chromosomes, as well as groups of cells during embryonic development. Understanding of such enigmatic biological structures will benefit greatly from new microscopy techniques that bridge this resolution gap [59].

The use of short wavelength light in the EUV or soft-x-ray (SXR) regions of the spectrum, represents one of the most promising alternative approaches for high-resolution imaging of thick samples [60]. EUV/SXR light can be used for nondestructive imaging applications requiring high resolution in thick samples [61]. Furthermore, numerous core-shell absorption edges and widely varying elemental absorption cross sections provide excellent inherent image contrast. For instance, with these unique characteristics, light at 800 eV has been used for imaging magnetic nanostructures [62, 63]. However, some of the most exciting possibilities exist in the realm of biology. Between the K-shell absorption edges of carbon at $\sim$290 eV and oxygen at $\sim$530 eV, nature has provided a 'water window' where organic materials are up to 10 times more absorbing than water [58]. Using synchrotron sources, imaging in this 'water window' region of the spectrum has already allowed imaging of several micron thick samples with high intrin-

sic contrast, and 3-dimensional tomography of a cell at impressive resolutions (~ 60 nm) has also been demonstrated [61, 64]. The long-term goal of the work I am presenting in this thesis is to enable these exciting capabilities using a tabletop-size microscope setup.

5.2 Coherent vs. Incoherent Illumination and Imaging

Human vision, i.e. the imaging of light transmitted through or reflected from objects, forms the basis of our perception of reality. Not surprisingly, the qualities of the light illuminating an object, such as its frequency, polarization, and intensity, can dramatically change our perception of the object. Along with these qualities, we must also consider whether the illumination is coherent or incoherent. For instance, when a painted wall is illuminated by the sun, it looks quite different than the speckle pattern we observe when the same surface is illuminated by a visible laser beam. In simple terms, if we can merely add the square of the amplitudes of the light waves, the illumination is incoherent, but if we must first add the amplitudes of the waves and then square the sum, the illumination is coherent [65]. For instance, if I take two separate mirrors and use them to reflect light from an incoherent source like the sun onto a screen, the illumination will be brighter where the two beams overlap. However, if I shine light from two coherent sources, such as two identical lasers, onto a screen, the brightness where the two beams overlap will depend on the phase relationship between the two waves in the overlapped region.

Of course, the coherence of illumination in most experiments is neither perfectly coherent nor perfectly incoherent, but instead lies somewhere between these two extremes. The following discussion of partial coherence, briefly summarizes a treatment by Fowles [17]. Strictly speaking, the time averaged light flux at a given point where two monochromatic fields $\mathbf{E}_1$ and $\mathbf{E}_2$ meet is given by the irradiance

$$\mathscr{I} = \langle \mathbf{E} \cdot \mathbf{E}^* \rangle = \langle |\mathbf{E}_1|^2 + |\mathbf{E}_2|^2 + 2Re(\mathbf{E}_1 \cdot \mathbf{E}_2^*) \rangle \tag{5.1}$$

where the sharp brackets imply the time average. Making the assumption that this average remains constant regardless of the definition of the time origin, and furthermore, that the fields possess identical polarizations, so we may ignore their vectorial nature, Equation 5.1 becomes

$$\mathscr{I} = \mathscr{I}_1 + \mathscr{I}_2 + 2Re\langle E_1 \cdot E_2^* \rangle \tag{5.2}$$

$$\mathscr{I}_1 = \langle |\mathbf{E}_1|^2 \rangle \qquad \mathscr{I}_2 = \langle |\mathbf{E}_2|^2 \rangle$$

In a generalized interference experiment, the fields E_1 and E_2 come from a common source but take differing optical paths to some point of overlap. In general the fields take unequal amounts of time to traverse these divergent paths, and a phase difference arises between the fields at the overlap point. Calling the time to reach the overlap point t for E_1 and $t + \tau$ for E_2, the interference term in Equation 5.2 is written as

$$2Re\Gamma_{12}(\tau) \tag{5.3}$$

where

$$\Gamma_{12}(\tau) = \langle E_1(t) \cdot E_2^*(t+\tau) \rangle \tag{5.4}$$

This function, $\Gamma_{12}(\tau)$ is known as the *mutual coherence function*, and it measures, as a function of separation in space and time, the extent to which we can predict the electric field at one point if we know its value at some other point [60]. However, for convenience, this function is often used in a normalized form known as the *degree of partial coherence*, and given by

$$\gamma_{12}(\tau) = \frac{\Gamma_{12}(\tau)}{(\mathscr{I}_1 \mathscr{I}_2)^{\frac{1}{2}}} \tag{5.5}$$

Using the degree of partial coherence the irradiance is expressed by

$$\mathscr{I} = \mathscr{I}_1 + \mathscr{I}_2 + 2(\mathscr{I}_1 \mathscr{I}_2)^{\frac{1}{2}} Re\gamma_{12}(\tau) \tag{5.6}$$

In general, $\gamma_{12}(\tau)$ is a complex periodic function of τ, and an interference pattern will result when $|\gamma_{12}(\tau)| \neq 0$. The types of coherence can be summarized in terms of

$|\gamma_{12}(\tau)| \neq 0$ as follows:

$$\begin{aligned} |\gamma_{12}| &= 1 \quad \text{(complete coherence)} \\ 0 < |\gamma_{12}| &< 1 \quad \text{(partial coherence)} \\ |\gamma_{12}| &= 0 \quad \text{(complete incoherence)} \end{aligned} \tag{5.7}$$

For an interference pattern, the contrast of fringes varies between a maximum and minimum value given by $\mathscr{I}_{max}$ and $\mathscr{I}_{min}$ where

$$\mathscr{I}_{max} = \mathscr{I}_1 + \mathscr{I}_2 + 2(\mathscr{I}_1\mathscr{I}_2)^{\frac{1}{2}}|\gamma_{12}| \quad \mathscr{I}_{min} = \mathscr{I}_1 + \mathscr{I}_2 - 2(\mathscr{I}_1\mathscr{I}_2)^{\frac{1}{2}}|\gamma_{12}| \tag{5.8}$$

and the fringe visibility $\mathscr{V}$ is defined as

$$\mathscr{V} = \frac{\mathscr{I}_{max} - \mathscr{I}_{min}}{\mathscr{I}_{max} + \mathscr{I}_{min}} \tag{5.9}$$

and for $\mathscr{I}_1 = \mathscr{I}_2$, $\mathscr{V}$ will be given by

$$\mathscr{V} = |\gamma_{12}| \tag{5.10}$$

In essence, the fringe visibility in an interference experiment reveals the level of coherence of a source [17]. In fact, a measure of fringe visibility in a double pinhole interference experiment has been used previously by our group to study and quantify the level of coherence of our HHG source [55, 66].

The type of illumination chosen, along with the imaging method used, the quality of the instrument, and the skill and experience of the observer, all mix together in the final process of image interpretation. In general, the question of whether coherent or incoherent illumination is better has no definitive answer unless applied to a specific set of imaging parameters. For instance, for a conventional optical microscope in the bright field imaging mode, highly coherent illumination tends to be associated with several undesirable effects. These effects include a 'ringing' in the image from sharp edges, a granular speckle background coming from randomly phased scatters in the illuminating

light diffuser, and a high sensitivity to imperfections such as dust or scratches along the optical train of the instrument [67].

In contrast, any imaging technique that uses phase information as a contrast mechanism requires at least some degree of coherence. In optical microscopy, some techniques requiring coherence include phase contrast, differential interference contrast, and polarization contrast microscopy. These techniques can detect phase changes induced by small variations in a specimen's index of refraction. Even the incandescent filament lamps used in optical microscopes exhibit partial coherence, and the degree of coherence can be adjusted by selecting portions of the source light with a condenser aperture. In this case, the coherence originates from strong interactions that occur between neighboring atoms in microscopic domains during photon emission. These effects give rise to localized synchronous emission of discrete bundles of light over the filament's surface [68]. On the other hand, holographic imaging techniques require a very high degree of coherence. In classic holography, the light from a coherent source is split into two beams, one illuminating a sample and the other serving as a reference. After the illuminating beam interacts with the a specimen, it interferes with the reference beam and the resulting interference pattern is recorded. This interference pattern essentially encodes the phase information carried by the illuminating wave as intensity modulations [17]. The relatively new technique of lensless diffractive imaging, which is the imaging method we have chosen to mate with our HHG source, also necessarily requires coherent illumination and will be discussed in more detail in Section 5.5.

5.3 Spatial and Temporal Coherence

The discussion in the preceding section concerning coherence dealt with fairly idealized sources. Light sources in practice have a finite source size, a finite spectral bandwidth, and radiate with some restricted angular extent. Therefore, it is often more appropriate in practical terms to determine the region over which the light from a

realistic source can be considered coherent, in directions both perpendicular and parallel to the light's propagation direction [60].

The coherence parallel to the direction of propagation is referred to as the temporal coherence, and a temporal coherence length $\mathscr{L}_{Tcoh}$ can be defined as

$$\mathscr{L}_{Tcoh} = \frac{\lambda^2}{2\Delta\lambda} \tag{5.11}$$

where λ is the wavelength of the light and $\Delta\lambda$ is its FWHM bandwidth. This temporal coherence length equates to the length of propagation that causes two waves that are separated in wavelength by exactly the bandwidth to slip 180° out of phase [60]. So, in a diffraction experiment, path length differences from the diffracting object to the observation plane should be kept under this length to maintain a well-defined diffraction pattern.

Similarly, the coherence transverse to the direction of propagation is referred to as the spatial coherence, and a spatial coherence length $\mathscr{L}_{Scoh}$ can be defined as

$$\mathscr{L}_{Scoh} = \frac{z\lambda}{2\pi\mathscr{D}} \tag{5.12}$$

where z is the distance from the source, and $\mathscr{D}$ is the source's diameter [60]. $\mathscr{L}_{Scoh}$ gives the spatial extent over which two points in a transverse slice of the beam can still be considered to have a well correlated phase relationship. So, in an experiment to record diffraction from an object, care should be taken to keep $\mathscr{L}_{Scoh}$ of the illuminating light larger than the transverse dimension of the sample object.

5.4 Imaging in the Extreme Ultraviolet

Producing images in the EUV involves a set of challenging parameters not prevalent with visible light sources. The glass lens is an ancient scientific device, with its origins tracing back more than a thousand years ago. In terms of imaging, this elegant optical element forms the backbone of even the most advanced modern optical

microscopes. Unfortunately, for imaging at EUV wavelengths, the venerable glass lens cannot be used. A glass lens relies on the phenomenon of refraction for its ability to focus light and produce images. However, refractive imaging does not exist at EUV wavelengths due to the nature of the index of refraction for this region of the spectrum. The following explanation is a brief summary of a discussion given by Attwood in [60].

At EUV wavelengths the index of refraction varies only slightly from unity and is expressed as

$$n(\omega) = 1 - \delta + i\beta \tag{5.13}$$

To understand the δ and β terms in Equation 5.13, consider a plane wave

$$\mathbf{E}(\mathbf{r}, t) = \mathrm{E}_0 e^{-i(\omega t - \mathbf{k}\cdot\mathbf{r})} \tag{5.14}$$

propagating in material with an initial amplitude E_0 and having the magnitude of $\mathbf{k}$ as

$$k = \frac{\omega}{c}(1 - \delta + i\beta) \tag{5.15}$$

Then, for the propagation direction that satisfies $\mathbf{k} \cdot \mathbf{r} = kr$

$$\mathbf{E}(\mathbf{r}, t) = \underbrace{\mathrm{E}_0 e^{-i(\omega t - r/c)}}\,\underbrace{e^{-i(2\pi\delta/\lambda)r}}\,\underbrace{e^{-(2\pi\beta/\lambda)r}} \tag{5.16}$$

the first exponential term in Equation 5.16 represents the phase shift that would have resulted from propagation in vacuum, the second exponential describes the phase shift induced by the material, and the third exponential represents decay of wave strength due to absorption. The values of δ and β in the EUV are such that no significant refraction can occur in material before the incident wave is completely absorbed. Therefore, optics in the EUV must rely on reflection or interference effects to focus, image, and manipulate the light field. [60].

Fresnel zone plate lenses, usually just called zone plates, are the most common diffractive optical elements used in high resolution imaging at EUV and shorter wavelengths. These diffractive optics are basically chirped transmission diffraction gratings

in a circular geometry. An SEM micrograph of a zone plate is shown in Figure 5.1. The central region of the zone plate is opaque to the wavelength of interest. Going

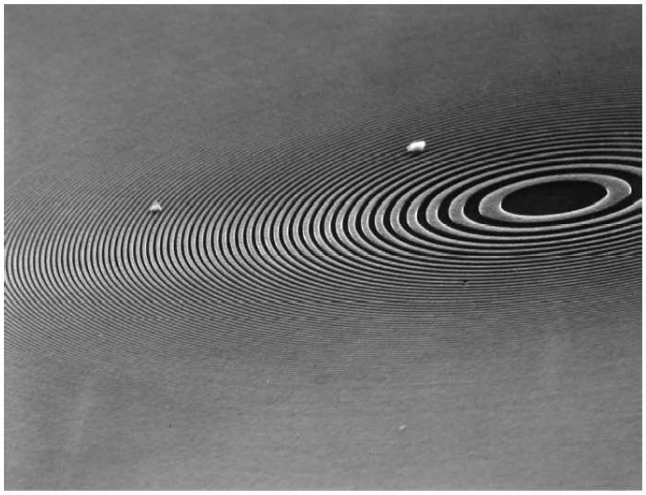

Figure 5.1: A zone plate as seen by a scanning electron microscope, picture by Eric Anderson, LBNL. From [60]

radially outward from this central portion, concentric zones alternate between being transmissive and opaque while also getting finer in spacing. So, as a beam of light shines on this structure, it has a small angle of diffraction near the inner most zones, and a large angle of diffraction at the outermost zones. With the proper arrangement of zones, the diffraction through the zone plate leads to constructive interference at a well-defined point. This situation equates to defining a focal point [60]. In his book, "Soft X-Rays and Extreme Ultraviolet Radiation: Principles and Applications," David Attwood presents a thorough treatment of zone plates, and the reader is referred to this reference for a detailed overview. However, I wish to summarize a few of his key points for the purpose of comparison. First, the resolution attainable with a zone plate is on the order of the size of its smallest outer zone, labeled Δr. Thus, the manufacturing process must produce dimensional tolerances that are much smaller than Δr. To achieve this demanding specification, advanced electron beam lithography and etching

techniques are employed [69]. Additionally, the focal length *f*, depth of focus DOF, and spectral bandwidth requirement of a zone plate lens are given as follows:

$$f = \frac{4N(\Delta r)^2}{\lambda} \qquad \text{DOF} = \pm\frac{2(\Delta r)^2}{\lambda} \qquad \frac{\lambda}{\Delta\lambda} \geq N \tag{5.17}$$

where N is the number of zones, and λ is the illuminating wavelength [60]. As with conventional lenses, focal lengths of zone plate lenses must be quite short to obtain good magnification. Spatial resolutions as high as 15 nm have been achieved with the XM-1 microscope at the Advanced Light Source in Berkeley using a state-of-the-art zone plate with $\Delta r = 15$ nm, 500 zones, and a 1.5 nm illuminating wavelength [69]. Using this zone plate as an example, we see that for $f = 300$ μm, the depth of focus is 300 nm, and $\frac{\lambda}{\Delta\lambda}$ must be better than 500. So at high magnifications, zone plates have a relatively short working distance, a small depth of focus, and the potential for large chromatic abberation. Additionally, the design of a zone plate, which blocks much of the light it receives, makes them typically around 10% efficient in the first-order diffracted light. Despite these challenges, resolutions down to 38 nm have been demonstrated using tabletop EUV lasers that exhibit superbly narrow spectral bandwidth [70, 71]. Unfortunately, the range of these lasers does not extend into the 'water window' region of the spectrum that tabletop HHG sources have already reached, albeit with limited flux. Currently, however, high harmonic sources have only demonstrated resolutions of $\sim$ 200 nm with zone plate imaging using 13 nm light [72].

Holography represents another possible imaging method in the EUV, and was first demonstrated with x-rays in 1987 using Gabor holography [73]. Gabor holography is a very straightforward holographic technique in which the illuminating light wave impinges on a weakly scattering object, after which the undisturbed portion of the illuminating wave becomes its own reference wave and interferes with the scattered wave in the far field [74, 75]. In an on-axis Gabor holography experiment, this situation can be accomplished by using a small scattering specimen in comparison to the illuminating

beam size. The need to surround a specimen by a large highly transmissive region limits the usefulness of Gabor holography, particularly in the EUV region of the spectrum [67]. Natural extensions of Gabor holography, such as Fourier transform holography have yielded sub-100 nm resolutions using spatially filtered coherent x-rays at synchrotron facilities [76].

Lensless diffractive imaging is a relatively new coherent imaging technique that is an extension of holography [77–80]. It requires spatially coherent beams and replaces imaging elements in the optical system with a computerized phase retrieval algorithm. By obviating the need for physical imaging optics, this technique is well-suited to the EUV, and was first demonstrated in 1999 using spatially-filtered x-ray light from a synchrotron source [77]. In principle, lensless diffractive imaging is free of aberrations, has a very large depth of focus, and can achieve diffraction limited resolution. Using this technique at a synchrotron, a freeze-dried yeast cell has been imaged to better than 30 nm resolution [81]. In other exciting work, 3-dimensional reconstructions of objects have been achieved to better than 50 nm resolution [82] Very recently in 2006, the first lensless diffractive microscopy using a soft-x-ray free-electron laser at 32 nm wavelength was demonstrated, with a claimed resolution of $\sim$ 60 nm [83].

5.5 Lensless Diffractive Imaging

In the late 1800's the German physicist and influential microscope designer Ernst Abbe introduced the notion that Fourier analysis could be applied to the theory of imaging. In an analogy to the manner in which an arbitrary bounded waveform with only finite discontinuities can be thought of as being decomposed to a series of elementary functions consisting of sines and cosines with different frequencies, Abbe suggested that an object to be imaged with coherent illumination could be thought of as being composed of a series of gratings with varying periodicities, positions, and orientations. So, the total diffraction from an irregular object can be realized as the sum of the

diffraction contributions from its various component gratings combined with the correct background component. However, this idea is strictly *not* the same as suggesting that an object can be considered as the overlay of many varied gratings. When using a lens to image the object, the diffraction contributions interfere at any point at which overlap between them occurs, but only near the image plane does this interference produce a meaningful reproduction of the object [65]. Amazingly, lensless diffractive imaging, as the name implies, performs this feat without the use of a physical lens.

5.5.1 The Phase Problem

Under the conditions of coherent plane wave illumination and validity of the Born approximation, the light wave diffracted from an object forms the Fourier transform of the object [84]. Considering this idea from the Abbe point of view suggests that the phase information carried by the diffracted wave contains the critical components to reproducing a faithful image of the object. Writing the Fourier transform $\mathscr{F}$ of an arbitrary finite object described by the function $g(x, y)$ as

$$\mathscr{F}\{g(x,y)\} = G(k_X, k_Y) \tag{5.18}$$

where the transformation is from the space domain to the frequency domain, and k_X and k_Y are coordinates in the frequency domain, the two dimensional Fourier shift theorem states that

$$\mathscr{F}\{g(x-a, y-b)\} = G(k_X, k_Y)\exp[-i2\pi(k_X a + k_Y b] \tag{5.19}$$

Or, stated in words, translating a function in the space domain corresponds to creating a linear phase shift in the frequency domain [67]. Thinking about the diffracted wave as coming from the contributions of many gratings, the positions of these conceptualized gratings will relate to the shape of the diffracting object. Thus, the phase information contained in the diffracted wave must be preserved or retrieved to allow for meaningful imaging. A lens preserves this phase information, but a simple energy detector (such as

photographic film or a CCD array) cannot.

A traveling electromagnetic wave carries both amplitude and phase information. However, detectors of electromagnetic waves in optics only record the intensity of the waves given by $|\mathbf{E}|^2$, leaving no possibility for direct detection of the phase information. This phase problem is pervasive in areas of imaging and diffraction. Thus, solving this phase problem is an active topic in areas as diverse as wave front sensing, astronomy, crystallography, and diffractive imaging [85]. In a general form, the phase problem involves determining an object $f(\mathbf{x})$ solely from intensity measurements of its Fourier transform $F(\mathbf{u})$. $F(\mathbf{u})$ can be expressed as

$$\begin{aligned} F(\mathbf{u}) &= |F(\mathbf{u})| \exp[i\psi(\mathbf{u})] = \mathscr{F}[f(\mathbf{x})] \\ &= \int_{-\infty}^{\infty} f(\mathbf{x}) \exp[2\pi i \mathbf{u} \cdot \mathbf{x}] d\mathbf{x} \end{aligned} \tag{5.20}$$

where $\mathbf{x}$ is an M-dimensional spatial coordinate, and $\mathbf{u}$ is an M-dimensional spatial frequency coordinate . Thus, the Fourier transform $F(\mathbf{u})$ can be written as an amplitude and a phase. With only intensity measurements of $F(\mathbf{u})$, to fully recover $f(\mathbf{x})$, one must determine the phase function given by $\psi(\mathbf{u})$ [85].

5.5.2 The Oversampling Method

The problem of retrieving phase information has been well studied in the field of x-ray crystallography. In x-ray crystallography the diffraction from many identical unit cells leads to constructive interference and very strong Bragg peaks. However, the oversampling technique can handle the situation that arises in diffraction from noncrystalline objects where detectable intensity appears between Bragg peaks, or where no Bragg peaks occur, and the diffraction pattern is continuous [84]. Sampling such a diffraction pattern at a frequency finer than that given in the situation of Bragg peaks is referred to as oversampling [86]. The idea that oversampling the diffraction pattern might be able to reveal the phase information was suggested by David Sayre in 1952 [87].

However, to make it possible to resolve features in an oversampled diffraction pattern with good fidelity, the diffraction pattern must have a high dynamic range and be produced with illumination that is both spatially and temporally coherent [86].

In 1998, Miao et al. gave the currently accepted explanation for the oversampling method [88, 89]. They suggested that each intensity point in the diffraction pattern can be viewed as a nonlinear equation. Solving the phase problem reduces to finding the unknown 'electron density' from this set of equations (since the oversampling method has its roots in the field of crystallography, the object of interest to be reconstructed when the phase problem is solved is the sample's electron density). However, when sampling is done at the Bragg peak frequency, twice as many unknowns exist as independent equations [84]. Miao calls the oversampling degree in real space σ, and defines it as

$$\sigma = \frac{\text{electron density region} + \text{no-density region}}{\text{electron density region}} \tag{5.21}$$

Furthermore, he calls the linear oversampling ratio for two dimensions in reciprocal space O, and defines it as

$$O = \sigma^{\frac{1}{2}} \tag{5.22}$$

[86]. For σ larger than 2, the number of independent equations exceeds the number of unknowns, and the phase information is embedded within the diffraction pattern [88].

Unfortunately, just performing oversampling cannot directly produce phase information. The phase itself must be retrieved using an iterative algorithm described in the following section. In addition, several experimental parameters must also be optimized concerning the sample, its placement relative to the detector, and the illumination.

In their paper entitled "On possible extensions of X-ray crystallography through diffraction-pattern oversampling,"Acta Crystallographica, vol. 56, pp. 596-605, (2000), John Miao and David Sayre present a very straightforward derivation of the oversampling theorem [84]. For an $N-by-N$ sized sample in real space, the Nyquist frequency in reciprocal space will be $1/N$. This theorem suggests that sampling (in reciprocal space)

the Fourier transform of an object at a frequency finer than its Nyquist frequency corresponds to generating a no-density region surrounding the electron density of the object (in real space). This theorem forms one of the primary experimental considerations for applying the oversampling method, as it means that a transmissive object must be surrounded by an opaque mask whose size scales with the degree of oversampling. The following derivation is a near verbatim version of the one in the aforementioned paper. If the electron density of an object is assumed to be $\rho(\mathbf{x})$, then the Fourier transform of this object is given by

$$F(\mathbf{k}) = \mathscr{F}[\rho(\mathbf{x})] = \int_{-\infty}^{\infty} \rho(\mathbf{x}) \exp[2\pi i \mathbf{k} \cdot \mathbf{x}] d\mathbf{x} \tag{5.23}$$

where $\mathbf{x}$ is the three-dimensional spatial coordinate in real space and $\mathbf{k}$ is the three-dimensional frequency coordinate in reciprocal space. If $F(\mathbf{k})$ is sampled at the Nyquist frequency of the object, then

$$F(\mathbf{k}) = \sum_{\mathbf{x}=0}^{N-1} \rho(\mathbf{x}) \exp[2\pi i \mathbf{k} \cdot \mathbf{x}/N], \qquad \mathbf{k} = 0, \ldots, N-1. \tag{5.24}$$

where $\mathbf{x}$ and $\mathbf{k}$ have become discrete and range from 0 to $N-1$ in each dimension. However, if $F(\mathbf{k})$ is sampled at twice the Nyquist frequency, then

$$F(\mathbf{k}) = \sum_{\mathbf{x}=0}^{N-1} \rho(\mathbf{x}) \exp[2\pi i \mathbf{k} \cdot \mathbf{x}/(2N)], \qquad \mathbf{k} = 0, \ldots, 2N-1. \tag{5.25}$$

Let us introduce a new function $g(\mathbf{x})$ such that

$$g(\mathbf{x}) = \begin{cases} \rho(\mathbf{x}) & 0 \leq \mathbf{x} \leq N-1 \\ 0 & N \leq \mathbf{x} \leq 2N-1 \end{cases} \tag{5.26}$$

If $g(\mathbf{x})$ is substituted into Equation 5.25, then

$$F(\mathbf{k}) = \sum_{\mathbf{x}=0}^{2N-1} g(\mathbf{x}) \exp[2\pi i \mathbf{k} \cdot \mathbf{x}/(2N)], \qquad \mathbf{k} = 0, \ldots, 2N-1. \tag{5.27}$$

Equation 5.27 represents the relation between the density function $g(\mathbf{x})$ and its fast-Fourier-transform pattern sampled at the Nyquist frequency of $g(\mathbf{x})$. Thus, oversampling the discrete Fourier transform of the object's density function by sampling more

finely than the object's Nyquist freqency generates a no-density region surrounding the electron density of the object as illustrated in Figure 5.2 [84]. Clearly, by the same logic, increasing the degree of oversampling increases the size of this no-density region.

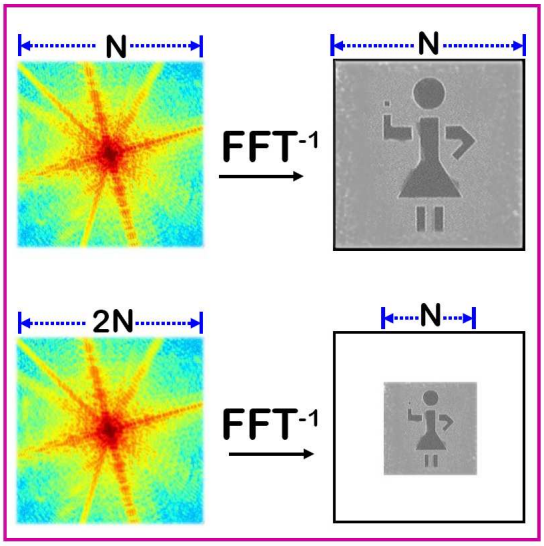

Figure 5.2: An illustration of the no-density region generated by oversampling the diffraction pattern

5.5.3 General Description of Algorithm

Our collaborator John Miao and his group at UCLA perform iterative phase retrieval on our diffraction data to yield a reconstructed image of our sample. The algorithm used to perform this phase retrieval is based on an approach suggested by Fienup [90]. Furthermore, the algorithm incorporates constraints concerning the electron density. For illumination with hard x-rays with energy far from any absorption edges, the electron density is positive and real. For lower energy illumination (EUV), the electron density is complex. The real part of this density is usually positive, and only becomes negative near absorption edges. The imaginary part, representing absorption by the sample, is positive definite [84]. The current algorithm, known as the guided hybrid input output (GHIO) algorithm, was developed by John Miao and consists of

the following four basic steps in each iteration [86]:

1. The square root of the measured diffraction intensities is the magnitude of the Fourier transform of the sample with some experimental noise. This magnitude of the Fourier transform is combined with a phase set to give a function with both amplitude and phase for each pixel. For the first iteration, a random phase set is used. For subsequent iterations, the best phase set available is used.

2. An inverse fast Fourier transform is applied to the outcome of the first step. This inverse transform provides a new electron density function.

3. The electron density function from the second step is now subject to the constraints that it must be positive inside the support and zero outside the support. To enforce the positivity constraint,the negative electron density inside the support is pushed close to zero, and the positive electron density inside the support is retained. To enforce the constraint outside the support, the electron density in this region is also pushed close to zero. In this manner, a new electron density is defined.

4. To calculate a new set of phases, a fast Fourier transform is applied to the electron density created in step three. The phase of the central pixel is set to zero, and this new phase set is employed in the following iteration [88].

The algorithm is shown schematically in Figure 5.3 [84].

5.5.4 Experimental Requirements

To obtain a given resolution with a high quality reconstructed image we must consider the sample, the placement of the sample with respect to the detector, qualities of the illuminating light, and the nature of the collected diffraction data. The sample should be illuminated with a plane wave and must be placed far enough from the detector to guarantee a far field diffraction pattern. In practical terms, plane wave illumination means that the sample aperture dimensions should be much smaller than the radius of curvature of the wavefront impinging on the aperture (we currently use a factor of

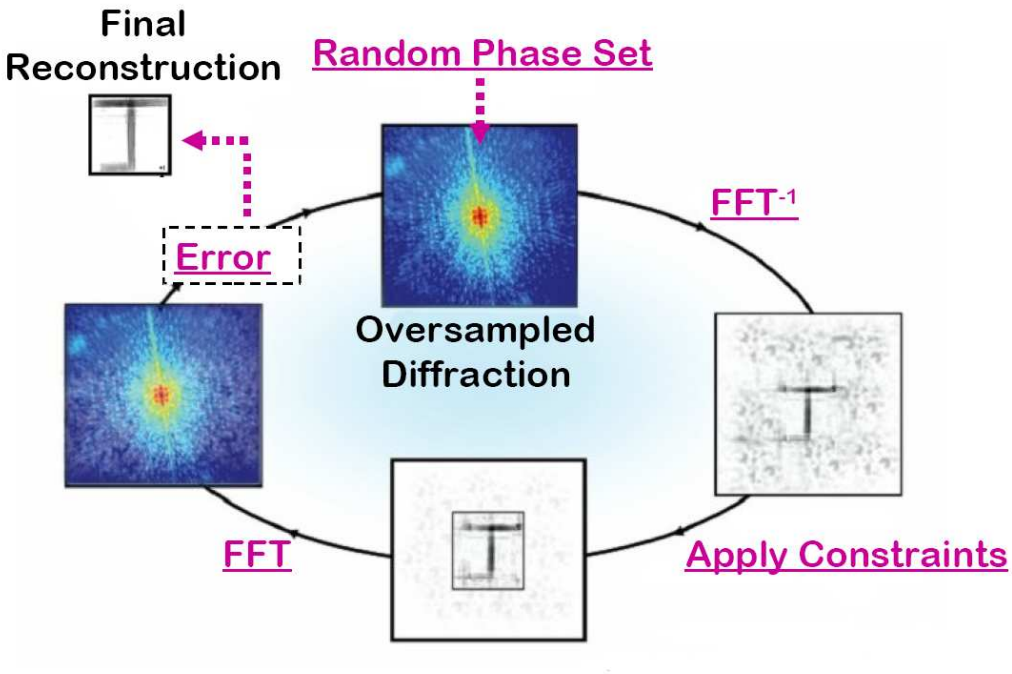

Figure 5.3: A schematic representation of the iterative phase retrieval algorithm

~ 100). For a far-field diffraction pattern, the Fraunhofer criterion must be satisfied, which for plane wave illumination is given by

$$z \gg \frac{D^2}{\lambda} \tag{5.28}$$

where in this case, z is the sample to CCD distance, D is the sample diameter, and λ is the illuminating wavelength. Essentially, the condition of Equation 5.28 ensures that the diffraction pattern is also in a plane wave condition and its curvature can be neglected [17]. From a practical point of view, z larger than the right hand side of Equation 5.28 by a factor of 3 is often sufficient, but a factor of 10 or more is much preferred.

The distance from the sample to the CCD is chosen to give an appropriate linear oversampling ratio (> 5) that allows for easily reconstructable diffraction patterns with high resolution [86]. The linear oversampling ratio relates the smallest diffraction pattern speckles to CCD pixels. The linear oversampling ratio O in terms of experimental quantities is given by

$$O = \frac{z\lambda}{Dp} \tag{5.29}$$

where z is the sample to CCD distance, λ is the wavelength, D is the sample diameter, and p is the pixel size of the CCD camera. In the reconstructed image, each image pixel (not to be confused with a CCD pixel), corresponds to a size r given by

$$r = \frac{OD}{N} = \frac{z\lambda}{pN} \tag{5.30}$$

where N is the linear number of pixels in an N-*by*-N CCD array. This image pixel size is suggestively labeled as r since it sets the ultimate resolution for any given geometry; with a pixelated image the sharpest discernable feature is at minimum one pixel wide. Since their is a one-to-one mapping of pixels in reciprocal space to pixels in real space (the reconstructed image), this condition can be thought of as coming from a 'conservation' of pixels. So, the larger we make O, the more pixels in the reconstructed image we must

allow to become part of the no-density region. So for a sample 1000 nm across, if $O = 1$ and we have 1000 pixels across in the reconstructed image, each pixel corresponds to 1 nm. However, if $O = 2$ the sample in the reconstructed image will only be 500 pixels across and be surrounded by a no-density region, so each reconstructed image pixel will correspond to 2 nm [84]. Of course, having the pixel size in the reconstructed image correspond to a particular dimension does *not* guarantee that we can achieve such a resolution. Clearly, we would like to have a detector with a large number of pixels, and the smallest pixel size possible. Several other important considerations affect the resolution. To begin, we must actually capture the diffraction information corresponding to features of a given size. Viewing features of the desired resolution as being diffraction gratings with a slit spacing d, we recall the familiar formula for first order constructive interference

$$d\sin(\theta) = \lambda \tag{5.31}$$

where we also note that $d\sin(\theta)$ is the path length difference between waves emanating from two adjacent slits and meeting at a common point. So, for a desired resolution d, we must ensure that the geometric conditions are such that the CCD camera captures this diffraction angle. However, we must also take care that the oversampling ratio in this geometry is sufficiently large for obtaining a high fidelity reconstructed image, and simultaneously, sufficiently small such that the pixel size in the reconstructed image allows resolving of features possessing the desired resolution. In general, for increasing resolution, these constraints require placing the sample closer to the detector to capture high diffraction angles, and shrinking the sample aperture to maintain the oversampling ratio and far-field condition. Additionally, the spectral bandwidth of the illuminating beam will affect the quality of the diffraction pattern and the reconstructed image. Thinking from the point of view of a simple diffraction grating, clearly if the light hitting such a grating is not monochromatic, the diffraction speckles will blur since

slightly different wavelengths will diffract at slightly different angles. Miao gives the spectral bandwidth requirement for lensless imaging as

$$\frac{\lambda}{\Delta\lambda} \geq \frac{OD}{d} \tag{5.32}$$

[86]. To clarify how the desired resolution comes into Equation 5.32, I think it is useful to put this condition into terms of temporal coherence. Multiplying each side of Equation 5.32 by λ gives

$$\frac{\lambda^2}{\Delta\lambda} \geq OD \cdot \frac{\lambda}{d} = OD\sin(\theta) \tag{5.33}$$

which now substituting into Equation 5.11 we can write

$$\mathscr{L}_{Tcoh} \geq \frac{OD}{2}\sin(\theta) \tag{5.34}$$

So the spectral bandwidth condition can be interpreted as suggesting that the temporal coherence length of the illuminating light should be larger than the *path differences* arising in the diffraction from illuminating an area larger than the sample aperture by O/2.

Chapter 6

Table-Top Lensless Microscopy

6.1 Introduction

Perhaps the most important factor in the success of the optical microscope as a tool for science has been its accessibility. The elegant compactness of this device allows scientists around the world to not only explore the wonders of the microscopic world, but it also gives them the freedom to invent and perfect new imaging and sample preparation techniques. The motivation for the work presented in this chapter is to forge a pathway towards a practical tabletop EUV microscope that takes advantage of the unique properties of our EUV source, and that can be scaled to use at shorter wavelengths. Here I describe the world's first demonstration of lensless diffractive imaging in the EUV using a table-top light source, and I discuss the possibilities of extending this work to shorter wavelengths and higher resolutions.

Much of the description of the imaging results presented here is an extension of a paper I authored with Richard Sandberg that will be published in Physics Review Letters. Furthermore, all of the reconstructed images presented here were produced by Changyong Song of John Miao's Coherent Imaging Group at UCLA.

6.2 Lensless Diffractive Imaging and HHG in Hollow Waveguides: A Natural Fit

6.2.1 Coherence of High-Order Harmonic Emission Generated Using a Hollow-Waveguide Geometry

Coherence of the illuminating light source forms one of the primary requirements for successful lensless imaging. Since this imaging technique relies on collecting diffraction from the specimen, the visibility of the diffraction pattern, and ultimately the resolution of the reconstruction, is directly related to the coherence of the illumination. Considering this requirement, most small-scale EUV and x-ray sources, as well as large-scale sources such as synchrotrons or free-electron lasers (FEL's) lack intrinsic coherence. Therefore, for coherent imaging techniques, the light must be sent through a monochromator, as well as made spatially coherent via spatial filtering through microscopic pinholes, causing a large loss of flux. Although the bright large-scale sources can handle this loss of flux, most small-scale sources are left without sufficient light for imaging in any practical manner. Thus, before the work presented here, lensless imaging experiments in the EUV and x-ray have only been conducted at synchrotrons or FEL's.

In some of my earliest days of graduate school research, I made several of the experimental pieces that helped Randy Bartels and Sterling Backus demonstrate that HHG performed in a gas-filled hollow waveguide generates essentially fully spatially coherent EUV beams at wavelengths of ~ 30 nm. The spatial coherence was measured via the visibility of fringes produced from a double pinhole experiment. To demonstrate the coherent imaging potential of this light source, it was also employed for Gabor holography with moderate resolutions of $< 10\ \mu m$ [55]. Later work in our group, using the same double pinhole technique, showed that HHG performed in the hollow waveguide geometry also gives spatial coherence at 13 nm, suggesting further that the trend is

intimately linked to phase matching of the HHG process and will continue to even shorter wavelengths [66, 91].

6.2.2 Efficient Use of Photons

Considering the unique nature of our high-harmonic source, the appropriate experimental approach is to investigate imaging techniques that take advantage of this source's intrinsic spatial coherence, and efficiently use its photons. Originally, we had considered performing imaging using zone plates, as we have collaborators at Berkeley that are world experts in the manufacture and use of these diffractive optics. However, traditional zone plate imaging would require us to destroy some of the spatial coherence to avoid 'ringing' artifacts in our images. Moreover, the low efficiency of zone plates at our operating wavelengths would severely limit our useable flux. Scanning transmission microscopy is another possibility that would actually benefit from our source, as its coherence should allow us to focus to near diffraction-limited spot sizes. However, this technique would again require zone plates and discard large amounts of flux. Since it involves rastering over many points in a sample, scanning transmission microscopy would also require extremely accurate positioning mechanisms, as well as methods for normalizing flux at each position. A purely reflective optics geometry using ultra-high quality multilayer mirrors could in principle be used to create high quality images and preserve flux [60]. However, such systems generally require incoherent illumination, and the optics arrangements are not usually conducive to a compact geometry. On the other hand, Gabor holography would take full advantage of our coherence, and has been demonstrated with tabletop sources at submicron resolution [92]. However, for on-axis Gabor holography, only a small fraction of the beam interacts with the sample. Since the signal coming from the diffracted wave is small, this technique is not well suited to our flux levels.

Oren Cohen, a post-doc in our group, originally suggested the possibility of trying

lensless diffractive imaging. Oren and Ra'anan Tobey performed some initial diffraction experiments that bolstered the feasibility of his suggestion, and afterwards, Richard and I pursued its implementation. Several aspects of lensless imaging make it an extremely elegant and appealing microscopy technique for our high-harmonic EUV source. The source, while bright, certainly does not compete with the overall flux available at a synchrotron or FEL. In the setup discussed here, the longest integration time is around 120 minutes. Therefore, ease of sample setup remains an important concern, as well as the long-term stability of the source. As long as the conditions outlined in Section 5.5.4 are met: including proper illumination, the appropriate sample size and sample to CCD distance, the technique should, in principle, work. Of course, the sample to CCD distance sets the linear oversampling ratio and ultimately determines the highest angle of diffraction that can be captured. Yet, placement of the sample is non-critical; $\sim$ mm placement accuracy is completely acceptable in our imaging geometry. In addition, no multi-step focusing process is necessary, in contrast to the case of physical imaging optics that require sample placement and stability at the micron level. Furthermore, when performing imaging with a single optic, the magnification is a purely geometric function of the object to image distance ratio, often requiring the detector to be a meter or more from the imaging optic for high-resolution work. In contrast, for table-top lensless imaging, the entire imaging apparatus fits in 0.5 m x 1.5 m, and large magnifications are achieved with only centimeters separating the sample and detector. I should also note that the same experimental setup will work at any shorter wavelengths at which bright coherent light can be produced, reflected, and made narrowband with reasonable efficiency.

6.3 Experimental Set-up

6.3.1 Illumination by the EUV Source

A 10 cm hollow waveguide is used to ensure full spatial coherence of the illuminating EUV light. The pump laser is typically run at a 3 kHz repetition rate, with 4.2 W of average power, a 780 nm center wavelength, and 25 fs pulses. The 150 μm inner diameter hollow waveguide is held in the v-groove geometry described earlier and filled with $\sim$ 65 torr of Ar. It should be noted that the best flux for the 27^{th} harmonic produced in this hollow waveguide filled with Ar is observed at a phase-matching pressure of $\sim$35 torr. However, the EUV mode generated at this lower pressure of Ar is less Gaussian and appears to have a less narrow spectral bandwidth than the EUV produced at 65 torr. Consequently, though the flux is greater, it fails to produce crisp diffraction patterns. Preliminary tests of spectral bandwidth of our source with an EUV spectrometer at the two pressures suggest a $\frac{\lambda}{\Delta\lambda}$ of around 200 for data taken at 65 torr and 120 at 35 torr. These estimates of the spectral bandwidth appear consistent when compared with the radial extent of clearly defined speckles seen in the diffraction data at the highest recorded diffraction angles (where smearing due to lack of monochromaticity will be most evident).

When optimally coupled, an EUV beam is generated with a beam waist radius of about 25 μm and approximately 1 milliradian divergence, with $\sim$ 5 harmonics centered near the 30 nm wavelength. Two 200 nm thick aluminum filters are used to extinguish the fundamental laser light. The second filter encountered by the laser light is held in a special light-tight filter wheel described later in this chapter. A pair of narrowband Mo/Si multilayer mirrors acts as both a monochromator and a condenser. The narrowband mirrors each have a peak reflectivity of about 25% centered 29 nm in a 2.5 nm bandpass, making it possible to effectively select a single harmonic order, in this case, the 27^{th} harmonic of the fundamental laser light. Having two mirrors narrows the band-

pass, and this bandpass can also lead to a slight narrowing of the spectrum of a single harmonic. The first mirror is flat, while the second has a 50 cm radius of curvature to gently focus the illuminating beam down to a beam diameter of a few hundred microns at the sample position.

To appropriately calculate the EUV beam size illuminating the sample, simple Gaussian beam propagation methods provide a useful and quick solution. However, care must be taken to include the initial radius of curvature of the wavefront exiting the waveguide in the input parameters of the calculation. A 1 milliradian divergence corresponds to an initial radius of curvature of about 2 cm. If the beam waist radius at the output of the waveguide is taken to be 25 μm, and its radius of curvature assumed to be 2 cm, the calculations give an estimate of the illuminating beam size along its optical path with sufficient accuracy. We confirmed the validity of these assumptions by changing the focusing geometry several times, taking careful measurements of the beam path, and recording the beam size on the CCD camera.

The position of the sample relative to the condenser mirrors and detector is chosen to optimize the illumination, the diffraction quality, and the oversampling ratio. We wish to use high EUV flux on the sample, while still maintaining a fairly flat intensity profile. To maintain high flux on a small sample, we focus the illuminating beam with a curved multilayer mirror. To make the illumination more uniform, the focused beam size overfills the sample. Assuming a perfect Gaussian beam, overfilling the sample by a factor of ~ 4 and using the most intense portion of the beam leads to an intensity distribution with a variation $\sim 10\%$. Overfilling the sample not only leads to a more uniform illumination, but also tends to ensure long-term illumination stability, mode quality, and a large radius of curvature of the EUV beam compared to the aperture size. Though overfilling the sample seems wasteful, conventional imaging would also require uniform illumination for the best results.

6.3.1.1 Mode Quality

A high quality and uniform EUV mode is needed for lensless imaging, to ensure the best spatial coherence and the best resolved diffraction data. Figure 6.1 shows the mode of the 29 nm beam after reflecting from the two multilayer mirrors. Strikingly, the mode profile fits to a near perfect Gaussian. This excellent beam spot quality results from both the development of consistent alignment techniques, and the major improvements in waveguide design described in Chapter 4.

The data plotted in Figure 6.1 represents a total of 5.2x10^7 counts on the CCD detector in a 2 second exposure. Knowing the number of counts and the efficiency of the optical elements lends itself to a flux estimate. To begin, the number of observed counts must be converted to a number of detected photons. As quoted by the manufacturer, the number of counts N_c seen per pixel at a gain setting of g for each incident photon of energy E is given by

$$N_c = \frac{E}{g3.65} \tag{6.1}$$

For the readout time used in this measurement, the camera had a gain setting of 2. In addition, only one harmonic order was detected, corresponding to 45 eV (29 nm). Therefore, the camera detected 4.2x10^6 photons per second. Next, the throughput of the optical system must be combined with the efficiency of the camera to determine the ratio of photons output by the waveguide to those detected by the camera. For all further quoted transmission, reflection, and efficiency in this estimate an energy of 45 eV will be assumed. After the waveguide, the EUV beam encounters two 200 nm aluminum filters, a set of two multilayer EUV mirrors, and finally, the detector. 400 nm of aluminum is about 40% transmissive at the energy of interest [38] However, pure aluminum oxidizes, and typically there will be about 10 nm of aluminum oxide per filter [93]. This 20 nm of aluminum oxide has a transmission of about 45%. Each mirror has a reflectivity of around 25%, and likely a 10 nm SiO_2 layer on each mirror (meaning

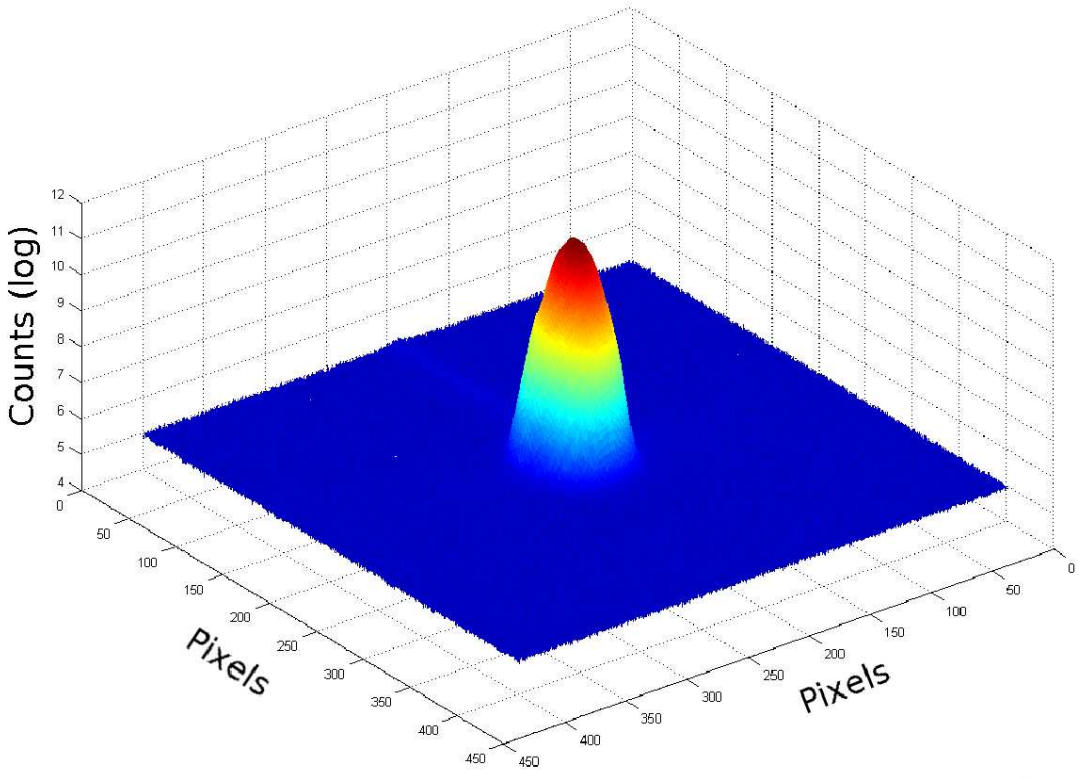

Figure 6.1: The mode of the 29 nm HHG light near its focus, plotted on a log scale.

effectively 40 nm total, since the beam must pass through this layer twice on each mirror bounce). 40 nm of SiO_2 has a transmission of 25%, giving a total throughput of the mirrors of 1.6%. Finally, the camera's manufacturer claims a quantum efficiency of approximately 33%, giving an overall throughput of the system as $9.3\text{x}10^{-4}$. This throughput amounts to an estimate of about $4.5\text{x}10^{9}$ photons per second or about 32 nW in a single 45 eV harmonic. However, the actual number may be an order of magnitude or so higher, as the CCD chip also surely had oxide layers. Moreover, after having antifreeze from a separate experiment condense on its surface repeatedly, the chip had been manually cleaned with methanol many times before this measurement, leaving a film of contamination that is difficult to quantify.

6.3.2 Geometry, Microscope Vacuum Chamber, and Detector

A schematic of the current imaging geometry is shown in Figure 6.2. Following the hollow waveguide and aluminum filters, the EUV light proceeds into the vacuum chamber where it reflect from the two multilayer mirrors in a z-fold configuration and is focused onto the sample. The two multilayer mirrors are preceded by a mirror held in a motorized flipper mount that can be inserted into the beam path. This mirror can be used to monitor the coupling of the driving laser light into the hollow waveguide, and also protects the sample from focused laser light when the aluminum filters are removed from the beam path. The first multilayer mirror is flat, and the second has a 50 cm r.o.c; both are mounted in compact motorized mounts so that their pointing may be finely adjusted under vacuum. To reduce astigmatism of the illuminating beam, the multilayer mirrors are positioned to bring the angle of incidence of the illuminating beam as close to the normal as possible. The sample is held on a 2-axis stage driven by closed loop DC motors that have a minimum incremental motion of $\sim$ 30 nm. This stage provides for precise alignment of the sample aperture and illuminating beam transverse to the beam propagation direction. A special mount for holding beam blocks precedes the

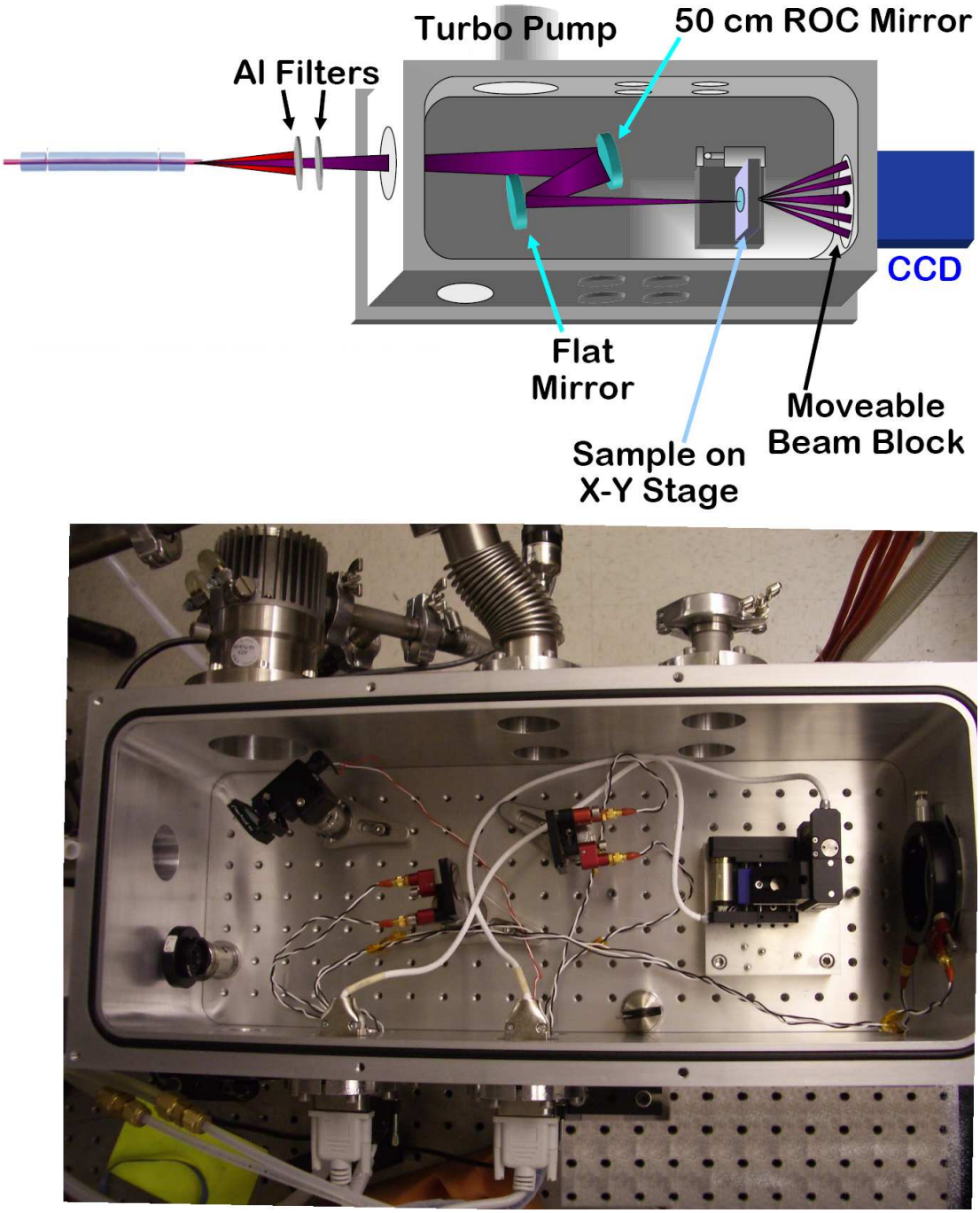

Figure 6.2: A schematic of the current transmission imaging geometry (top) and the custom microscope vacuum chamber (bottom)

CCD detector, and allows fine positioning of the beam blocks relative to the diffraction data.

I created the initial design of the current microscope vacuum chamber, however, Hans Green performed the actual machining of the chamber and made some essential modifications to my original conception. The chamber has an interior dimension of 8.5"x22", and a 6" depth. The chamber walls are made from a solid piece of aluminum, and they seal via an o-ring to the 1.25" thick base. The chamber base includes an integrated breadboard of $\frac{1}{4}-20$ holes on a 1 inch square grid, allowing flexibility and easy of alignment. Furthermore, the entrance port for the EUV illumination is vertically centered at 4" above the optic table height (the standard beam height in our optics experiments), and horizontally positioned such that it corresponds to a line of holes on the internal breadboard. The camera port is similarly designed, but with a 1" horizontal offset from the illumination port. A set of tapped holes encircles the camera port on the inside of the chamber to accommodate the beam block holder. To provide for quick pumping of the system, a turbo pump mates directly to the side of the chamber with no constrictions to limit its conductance. The mass and design of the chamber make it quite stable and we experience no sensitivity to vibrational noise induced by the turbo pump. Since the experiment requires frequent venting to change beam blocks (described in Section 6.3.3), the chamber lid is a single piece that relies solely on the force of atmosphere to keep it sealed and can be removed immediately upon venting. The chamber also includes 8 NW-40 ports for electronic feedthroughs, vacuum diagnostics, and to add flexibility to the design. Finally, a window with a light-tight removable cover has been included so that the coupling of the driving laser beam into the hollow waveguide may be monitored while the system is under vacuum.

The detector is a large-area x-ray CCD camera (Andor DO436). The camera bolts directly to the chamber and is sealed with a large o-ring in such a manner that its clear aperture is completely free of obstructions and a sample can be placed within

a minimum range of $\sim$ 2 cm from the CCD chip. The camera has a square array of 2048x2048 pixels each measuring 13.5 μm on a side. As a 16 bit device, it can read from between 0 and 65,356 counts per pixel. However, from a practical standpoint, this range varies from about 50 to 65,356 counts per pixel. The lower end of this range does not reach quite to zero due to intrinsic thermal noise and electrical noise during readout of the pixels. To reduce the 'dark' counts due to thermally excited electrons, the CCD chip is cooled to a temperature of -60° C. The readout of this camera can be made highly real-time by binning the pixels together in multiples of 2 up to 32. This binning feature becomes especially useful for sensitive feedback during alignment and flux optimization procedures. The camera also possesses the option of four readout times at 1, 2, 16, and 32 μs per pixel. Although the shortest readout time is quite useful for prompt feedback, the longest readout time corresponds to a significant reduction in background electrical noise in the image, and is therefore used for all final data sets.

6.3.3 Beam Blocks for Increasing Dynamic Range

When we go outside on a sunny day, the stars are still present but are not visible to the naked eye. In this case, the bright sunlight scattered in the atmosphere overwhelms the feeble light of the stars. Much like the human eye, a CCD camera has a limited dynamic range. If exposed to a light source past the point of saturation, the electrons in a CCD pixel begin to bleed into adjacent pixels. As pixels become over-saturated, information is lost and eventually the entire image is washed out. Unfortunately, the standard dynamic range of an x-ray CCD camera cannot capture both the strongly diffracted low spatial frequency information and the weakly diffracted high spatial frequency information from a sample simultaneously without over-saturating.

Just as a solar eclipse allows the stars to become visible during the daytime, beam blocks allow us to capture the weak large angle diffraction that corresponds to high spatial frequency information. These beam blocks vary in size and are placed in the

central high intensity region of the diffraction pattern. The larger-diameter beam blocks are used while acquiring long exposure images to record the high spatial frequencies diffracted from the sample, and the smaller beam blocks are used during the relatively shorter exposures to record diffraction emanating from low spatial frequencies. The beam blocks are positioned close to the CCD chip surface (within ~ 3 cm) to minimize any diffraction occurring around the edges of the beam block. Moreover, the blocks must be suspended in the beam path in a manner so that they block a minimum of the CCD area, other than the central spot.

Creating an effective beam block holder presented an enjoyable challenge. I sought a suitable wire with which to suspend the beam blocks. Tungsten thin wire is a most remarkable material. It has the ductility to be drawn into extremely fine diameters, yet possesses enormous tensile strength. The tungsten wire used to support the beam blocks has a diameter of 12.5 μm (nearly 5 times thinner than the average human hair). I designed the holder ring to allow easy replacement of the suspension wires, as well as have them cross at the exact center of the ring. A 3-dimensional rendering of the beam block holder ring is shown in Figure 6.3, and two different size beam blocks suspended on the holder ring are pictured in 6.4. Four identical dowel pins are pressed into the ring and are offset from a diametric line by their radius so that a wire stretched between them will be positioned in the center of the ring. The ring also includes a 0.010" lip across which the wires are stretched to tension them, and the securing screws are placed such that their clockwise tightening also tensions the wire.

Ideally, the beam blocks are circles with smooth and well-defined edges to take advantage of symmetry in the diffraction pattern and aid in their proper placement. The larger beam blocks are punched out of brass shim stock with a close tolerance blanking punch, and then superglued to the intersection of the suspension wires. In the case of the smallest beam blocks, I view the wires under a stereoscope and apply a small amount of 5-minute epoxy to the crossing point until I form an appropriately

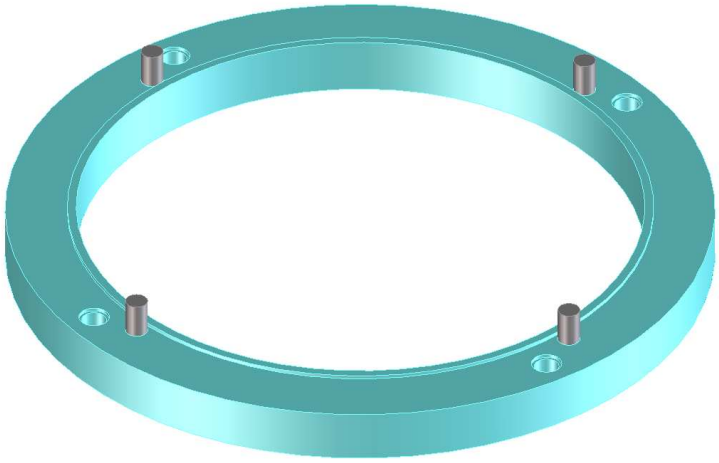

Figure 6.3: 3-d rendering of the beam block ring

Figure 6.4: A large and medium beam block suspended within the ring holder

sized epoxy ball. To gauge the size of the epoxy beam block when viewed with the stereoscope, I use a wire with a diameter equal to the desired diameter of the beam block for reference. In this manner, I can reliably produce beam blocks from the tens to hundreds of μm in diameter.

We record diffraction patterns of the sample with different size beam blocks in place, and subsequently stitch the patterns together. This procedure essentially extending the dynamic range of the camera from 3 to almost 10 orders of magnitude. However, for this procedure to remain most effective, the fidelity of the diffraction pattern and its position on the CCD camera must be carefully maintained. As such, the mounting ring for the beam blocks sits in a 2" kinematic x-y lens translator (Standa 5ZYP-2) that I retrofitted with two piezo stepper motors (New Focus tiny Picomotor actuator 8351) to allow fine control of the beam block position relative to the diffraction pattern. This retrofitted translator is shown in Figure 6.5. In addition, the beam block sizes must be carefully chosen so that enough well defined features of the diffraction pattern overlap between the various data sets to allow proper stitching and scaling of the data. Without the ability to accurately position the various size beam blocks, the diffraction pattern would need to be steered onto the detector, compromising its consistency and complicating the image-stitching procedure. Moreover, the moveable beam block saves enormous amounts of time. Originally, we used stationary beam blocks, that we could position nearly, but never exactly, to the center of the camera. Walking the diffraction pattern onto the beam block involves a laborious procedure of first adjusting the illumination beam pointing and then carefully adjusting the sample to compensate. Especially for the higher spatial frequency data, where weak diffraction makes feedback times painfully long (and yes, even 5 seconds for feedback is a long time in the wee hours!), the moveable beam block considerably shortens the overall image acquisition process.

As the resolution of the lensless microscope is pushed to shorter length scales,

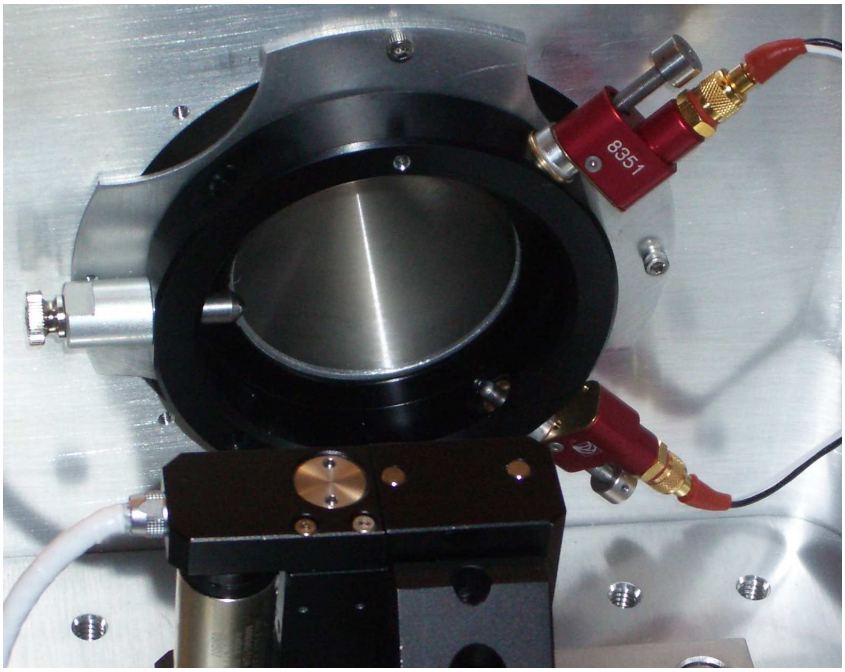

Figure 6.5: The x-y kinematic lens mount used to steer the beam blocks into position

and the acquisition times decrease through increased flux, improvements to the beam block configuration will be necessary. Most importantly, the ideal realization would include beam blocks that could be interchanged within the vacuum chamber with no need to vent the system and manually replace them. With a larger vacuum chamber, one possibility would be to have a fixture containing multiple beam blocks. Such a fixture could be translated to select the appropriate beam block, and then the fixture could be finely positioned to steer the chosen beam block with respect to the diffraction pattern. Although the wires suspending the beam blocks are quite fine, a small amount of information is lost with their presence. A slightly more fanciful, though feasible, solution would be to magnetically levitate spherical beam blocks and have a mechanism for exchanging different sized spheres [94].

6.4 Imaging Results

6.4.1 Initial Attempts and Improvements

When we began developing a lensless microscope, we performed our initial attempts in a reflection geometry in which I glued the sample to a mirror and masked all but a small portion with a pinhole aperture. Before Oren's suggestion to try lensless diffractive imaging, I was compelled to begin work on a microscope using zone plates. So, I developed several components that would turn out useful for the lensless version. I had already machined a small rectangular vacuum chamber from a solid block of aluminum to form a stable base for the microscope. Furthermore, with a condenser application in mind, we had previously made narrowband multilayer mirrors for operation around 29 nm, and we had also purchased compact piezo driven optic mounts for steering the beam (New Focus 8887). For motion control of the sample, I modified a two-axis micro translation stage (Standa 7T228T-9S35) so that it could hold a 1" diameter mirror and itself be held in a 1" optic mount. I also retrofitted this stage with the piezo stepper

motors that would later be used on the motorized beam block positioner.

Unfortunately, the dimensions and design of the vacuum chamber I had machined, along with the available positioners, were not conducive to the straightforward transmission geometries that had been demonstrated at synchrotron facilities. The geometry we used was quite simply a z-fold of the EUV beam using two mirrors. The first mirror was flat and held the sample. This mirror was held by the two-axis micro translation stage, which was in turn held by a motorized optic mount. So, the first mirror had 4 degrees of freedom; it could be tipped and tilted to steer the EUV light hitting the sample, and it could also be moved horizontally and vertically to align the sample. Although this arrangement functioned, it was quite unwieldy, and the lever arms involved made the beam steering particularly sensitive to adjustment. The second mirror had a 1 m r.o.c. so that the diffraction data could be collected and imaged onto the camera. Using this focusing optic was far from ideal. One of the advantages of lensless imaging is that in principle it is aberration free, but by introducing an optic downstream from the diffraction of the sample we introduced aberration and distortion of the wavefront. Furthermore, since the vacuum chamber had been designed for a different application, some of the clear aperture of the camera was blocked by the vacuum connections to the chamber, limiting the ultimate resolution of this geometry.

Despite these limitations, we decided to push forward to gain knowledge and insight while planning for a more optimized microscope design. We wished to begin by imaging an interesting test object that would provide a distinct diffraction pattern and that would be readily recognizable if the reconstruction efforts were successful. My advisor, Henry Kapteyn, suggested we use an electron microscope test grid. In particular, he pointed out a pattern made by Quantifoil Micro Tools GmbH that had the qualities which we were seeking. This pattern is shown in Figure 6.6, and consists of a $\sim$10 nm thick perforated plastic film stretched over a fine copper mesh and coated with $\sim$10 nm of carbon. The copper grid bars are nominally 10 μm wide, and the clear

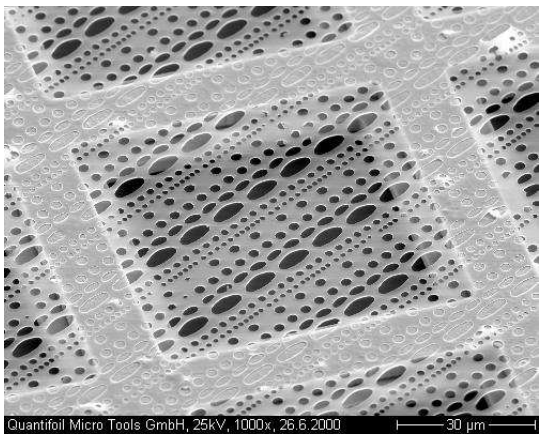

Figure 6.6: SEM micrograph of the QUANTIFOIL® MultiA carbon film, from [95]

aperture of each grid cell is 50x50 μm. To increase the opacity of the grid we sputter coated $\sim$ 100 nm of gold onto the surface. To mount this specimen to the mirror, I found that a stereoscope was an invaluable tool. Due to its large working distance, depth of field, and depth perception, a stereoscope allows one to view small objects and manipulate them with success. Konrad Lehnert has been kind enough throughout the lensless imaging work to let me use his stereoscope and micromanipulators to prepare samples. While viewing the mirror under the stereoscope, I placed the grid on the mirror, and used a micromanipulator to hold the grid in place while I applied small dots of glue to its edges. Next I placed a pinhole aperture over the grid and followed the same procedure to affix it.

Some of the original data from the reflection geometry is shown in Figure 6.7. Unfortunately, the original sample for this data was destroyed soon after the diffraction data had been collected, which taught us the valuable lesson of recording an optical or SEM picture of the sample *before* collecting any diffraction data. The diffraction data shown in Figure 6.7 represents only about half of the camera pixels, as the full data set includes a large blacked out region coming from the narrow vacuum connection to the camera. The sample was apertured with a 150 μm pinhole, so that portions of

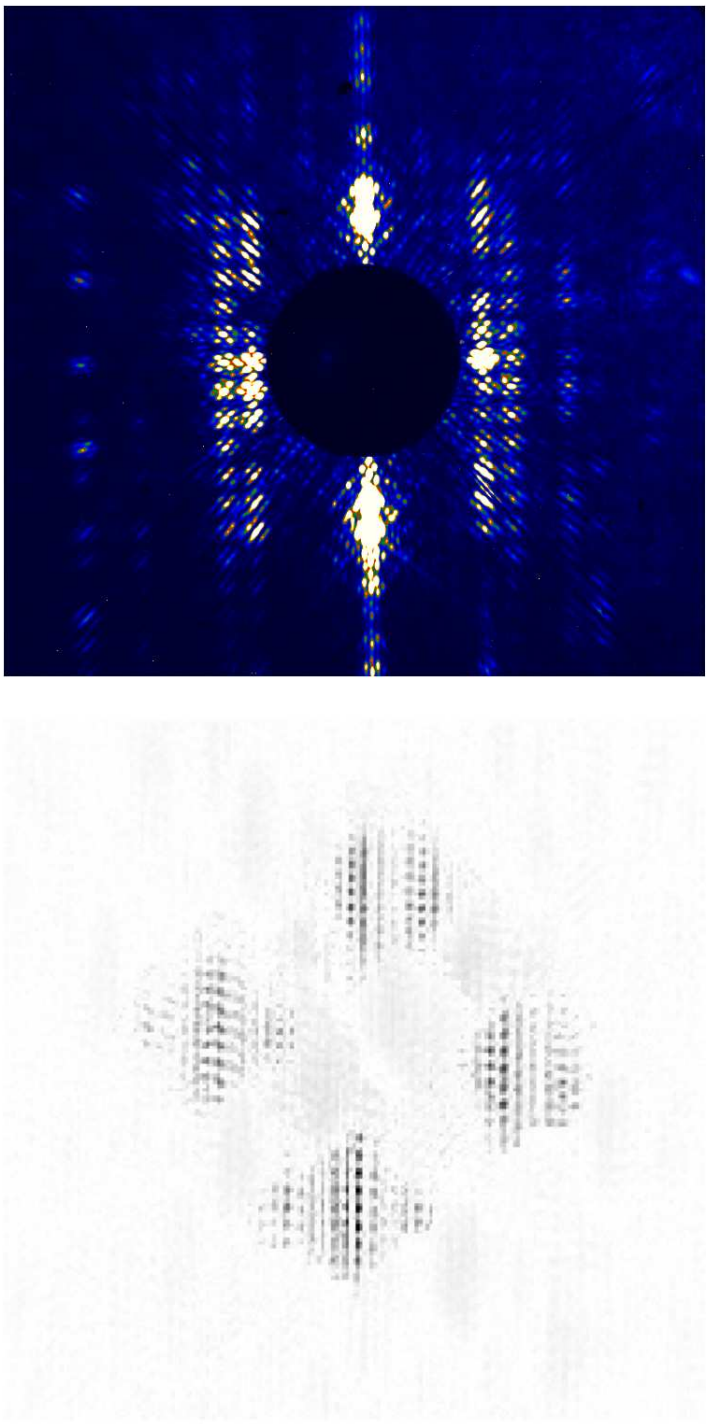

Figure 6.7: An portion of the high spatial frequency data taken for the reflection geometry on a linear scale (top), the reconstruction attempt showing some basic features but poor resolution (bottom)

4 grid cells were visible. The diffraction data shows reasonably well defined speckles, partially due to the amplification of signal by several identical grid cells. In addition, the EUV beam was many times larger than the sample aperture, so small changes in beam pointing had little effect on the data. Basic features of the grid geometry are visible in the reconstruction, but clearly the resolution and image quality are poor. Although promising, the initial attempts showed relatively serious limitations in terms of efficient use of flux, resolution, ease of alignment, and overall flexibility of the imaging system.

To fix some of these issues, we built a larger vacuum chamber specifically designed to the task of lensless imaging in a transmission geometry as described above. This geometry removes any optics between the path of the diffracted light and the detector. Furthermore, since it allows tight focusing onto a small sample, the efficient use of flux has been markedly increased. The transmission imaging geometry allows for a straightforward and highly effective alignment technique. To begin, the driving laser is set to run in a CW mode where no ultrafast seed pulse is introduced into the amplifying crystal, so that the only light comes from amplified spontaneous emission (ASE). The ASE provides rough alignment of the capillary and the steering mirrors within the chamber. When kept at low power, ASE is much safer to align with and will not damage the optics or sample. Next, we pump the system down, and optimize the EUV flux and mode with the pulsed laser at full power through a combination of adjusting capillary alignment, coupling conditions, and gas pressure within the capillary. After this point, care is taken not to disturb the pointing of the capillary, in particular the x-y adjustments at its output. The EUV mode is then centered on the camera using the internal chamber steering optics, and a baseline is established for exposure times. Next, we vent the system, put the sample in place, and set the driving laser to ASE at a power such that the laser focus is just visible to the naked eye when reflecting off the sample aperture. A bright light is placed behind the sample so the naked eye sees a small point of white light emanating from the sample aperture. Using an inspection

mirror, the overlap between the pump laser and the sample aperture can be viewed. The EUV beam path has been set to be centered on the CCD camera, so the sample itself is adjusted horizontally and vertically to match the illuminating light. Once we find a reasonable overlap, a white card is placed between the sample and the camera. With the room darkened, we view the light passing through the sample aperture with an IR viewer and maximize this light's intensity with fine movements of the sample translation stages. Since the v-groove fixture establishes an extremely straight waveguide, the pointing of the driving laser light coupled through the waveguide remains extraordinarily collinear to the produced EUV light. Therefore, when the system is again pumped down, only minor tweaks to the sample alignment are necessary to maximize the EUV diffraction.

Isolating the fundamental laser beam from air currents proved to be one of the most significant improvements for acquiring stable and crisp diffraction patterns. One of the unique characteristics of an ultrashort laser pulse is its relatively broad bandwidth. In terms of wavelength, our amplified ultrashort laser produces pulses with around 80 nm FWHM bandwidth. Considering classical dispersion, the various wavelengths forming the ultrashort pulse will experience different indices of refraction through a given material, and correspondingly, different phase delays. Stable material dispersions can be compensated with the gratings forming the heart of the well-known chirped-pulse amplification scheme [4]. However, air currents produce randomly fluctuating gas densities and so correspond to randomly fluctuating indices of refraction that lead to highly undesirable degradation of pulse stability. For the long acquisition times necessary for high resolution imaging, even slowly varying air currents cause a disturbance. In particular, air currents around the components of the amplifier at which the beam is spectrally dispersed lead to variations in the pulse's pointing, spectrum, and beam shape at the output of the amplifier [96]. These variations affect laser coupling into the hollow waveguide as well as the extreme nonlinear interaction of the laser with the gas in the hollow waveguide. Ultimately then, air currents disturbing the fundamental

amplified laser vary the flux, pointing, and spectrum of the generated EUV light. After seeing substantial improvements in laser beam stability with the simple addition of a cardboard tube around the portion of the beam being focused into the hollow waveguide, I decided the time had come to properly seal the laser system and path from air currents. With the assistance of Nathan Lemke I proceeded to make a series of acrylic enclosures for the optics of the front end pump lasers, as well as the steering optics on the output of the amplifier leading to the hollow waveguide. All the enclosures are assembled in an ingenious manner suggested by Etienne Gagnon, whereby the side pieces are held together with heavy duty thick double-sided sticky tape. Enclosures constructed in this manner not only form a quality air seal, but also allow for quick and easy reconfiguration. The enclosures are connected with a series of acrylic tubes and rubber gaskets, and the removable tops sit on foam weather stripping to further protect against stray air currents. As shown in Figure 6.8, the difference in diffraction pattern quality is astounding between data taken before and after the implementation of the enclosures. The clear radial smearing in the first picture of Figure 6.8 suggests that the spectral bandwidth of the EUV light was drifting during the acquisition most likely from variations in the fundamental laser pulse shape, power, or duration.

6.4.2 J-Slit Sample

Once we moved into the transmission geometry, we eventually decided to use a less ambiguous and more binary sample. To increase the ease of reconstruction, and get a feel for optimizing the transmission geometry, we wanted to try a rudimentary sample that was strictly either opaque or transmissive. We happened to have a small aperture in the shape of a "J" that had been laser machined into a piece of stainless steel shim stock. This "J-slit" turned out to be an excellent diagnostic sample.

The J-slit is about 80 μm tall (D), and was placed at a distance $z = 33$ cm from CCD. Referring to Equations 5.29 and 5.30, these values work out to a linear

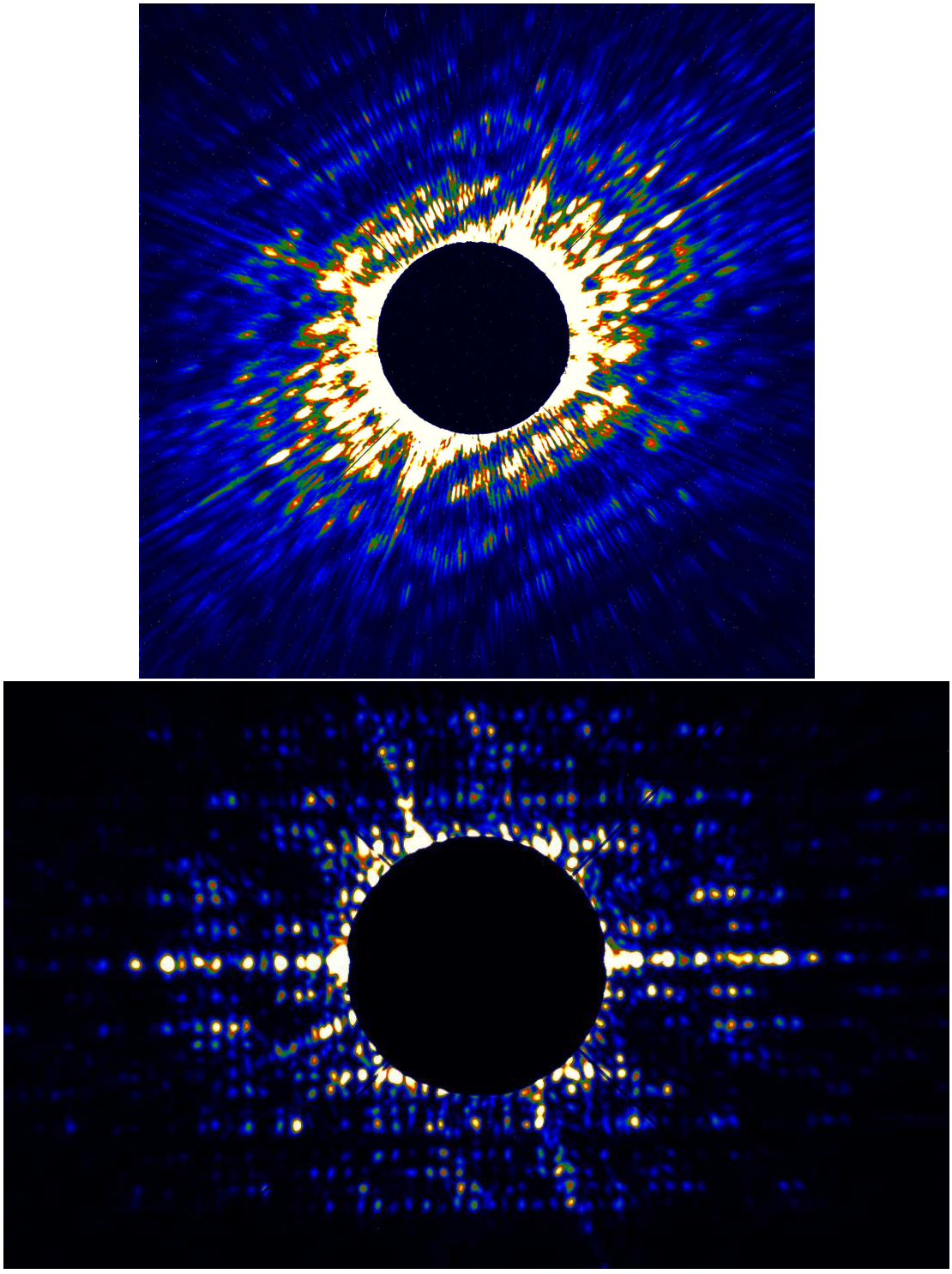

Figure 6.8: Data taken before the laser was isolated from air currents (top) and after (bottom)

oversampling ratio of 9, and an image pixel size of 0.3 μm. Pictures of the stitched diffraction pattern, an optical microscope image of the J-slit, and the reconstructed image are shown in Figure 6.9. Three different diffraction patterns were stitched together in order to form the high dynamic range data shown. The lowest spatial frequencies were captured with no beam block in about 1 minute. Next, a small beam block, $\sim$ 200 μm in diameter, was used to get slightly higher spatial frequencies in about 10 minutes. Finally, a larger beam block, $\sim$ 3 mm in diameter, was used to capture the highest spatial frequencies in about 120 minutes. The main purpose of this sample was to troubleshoot our system. Therefore, we were not concerned about optimizing the ultimate resolution, but rather, with convincing ourselves that we could obtain a reasonable reconstruction that gave a faithful reproduction of the sample. Clearly, this reconstruction shows the J-slit, and even preserves the aspect ratio of its components.

6.4.3 200 nm Resolution with QUANTIFOIL® Sample

To push the resolution of the system we returned to the QUANTIFOIL® sample, but this time with a 15 μm aperture. The sample was again gold coated, but with only about 20-30 nm of Au which should have a transmission between 10% and 3% for our illuminating wavelength. The sample to CCD distance was $z = 10$ cm, giving a linear oversampling ratio of about 14.5. Figure 6.10 displays the sample, diffraction data, reconstructed image, and a line-out of the reconstruction to demonstrate resolution. The picture in Figure 6.10a is a SEM micrograph of the sample taken here with the instrument in the JILA Keck Lab. This picture reveals that the sample has torn and a piece has folded back upon itself. I should note that the foil itself is sitting $\sim$ 50 μm above the aperture (Richard Sandberg estimated this distance by tilting the sample in the SEM and performing straightforward trigonometric calculations from the change in relative location of features). Moreover, the subtle difference in the observed aperture position between the SEM picture and the reconstructed image shown in Figure 6.10c is

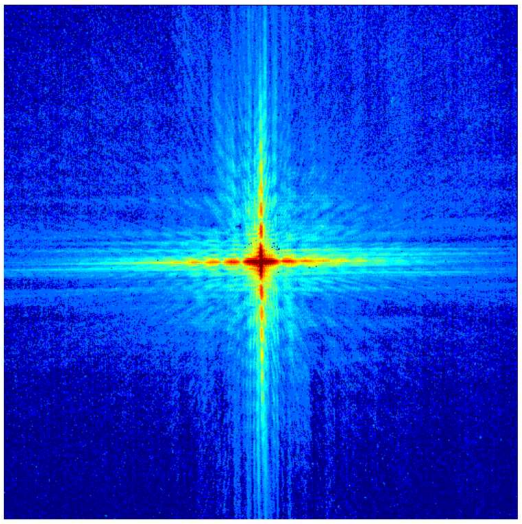

a) Logarithmic stiched diffraction

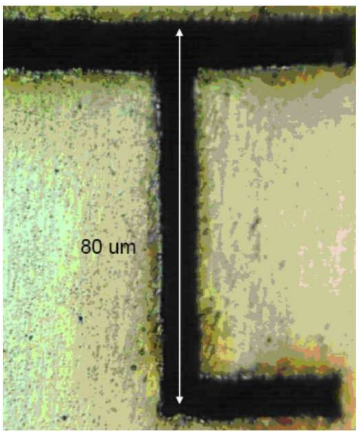

b) Optical microscope image of J-slit

c) Reconstructed image of J-slit

Figure 6.9: The diffraction data, J-slit sample, and reconstructed image

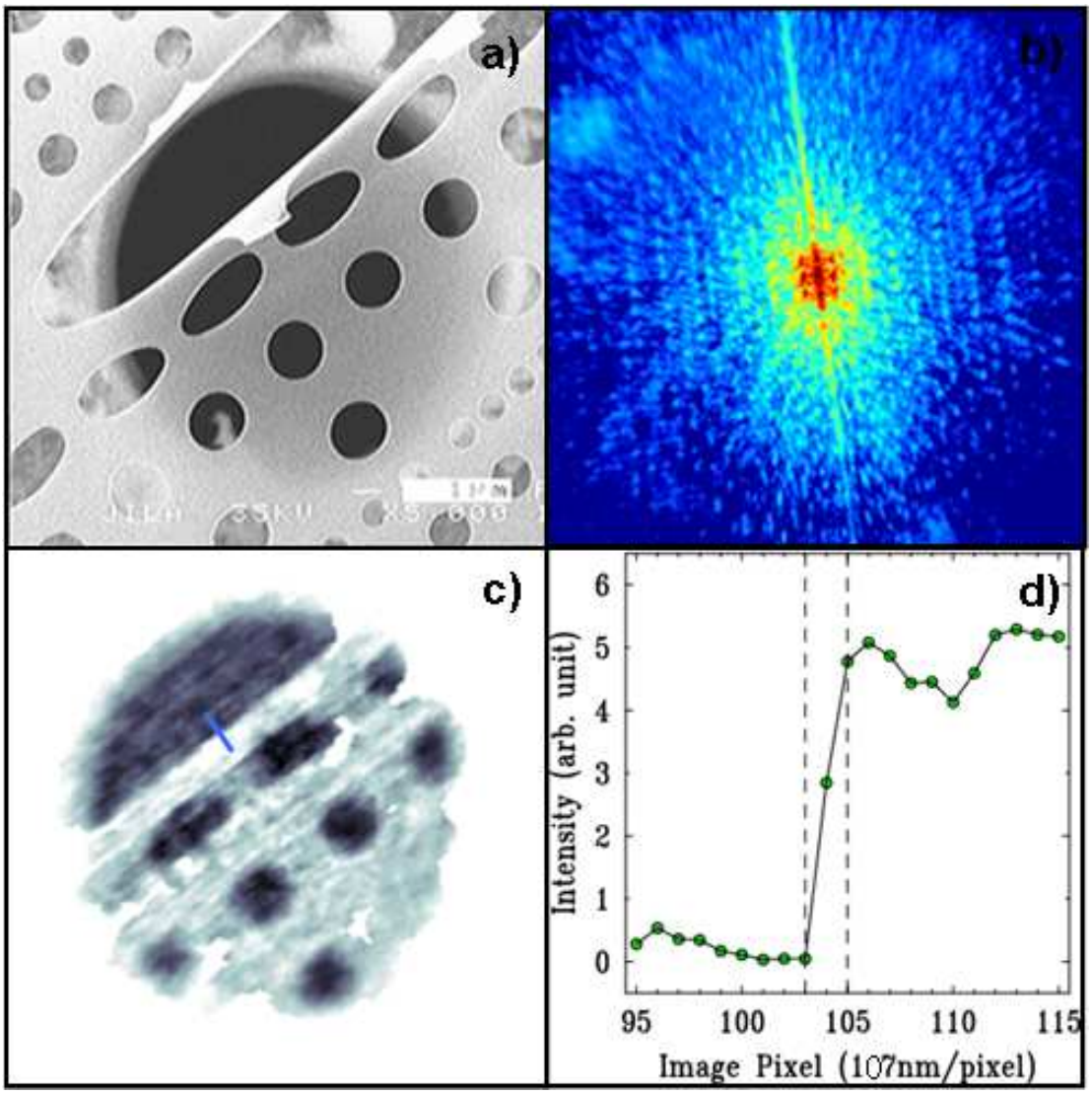

Figure 6.10: (a): SEM image of the sample over its 15 μm aperture , (b): the stitched diffraction data on a logarithmic scale, (c): the reconstructed image, (d): a line out of the reconstructed image taken across the small blue bar in (c)

merely from parallax. Figure 6.10b shows the coherent EUV diffraction pattern, and the non-centro-symmetry of the diffraction pattern indicates that the sample has absorption and that the sample density is complex. Finally, the line scan of the reconstructed image in 6.10d indicates that the current tabletop lensless microscope has a resolution of 214 nm.

By looking at the fidelity of the diffraction pattern speckles near the edge of the CCD camera (high scattering angle) we estimated a lower bound on our spectral bandwidth of ~ 200, and this estimate corresponds well to preliminary measurements taken using an EUV spectrometer. However, for the claimed resolution the spectral bandwidth requirement would appear to me much higher, more on the order of 1000. Fortunately, since the experimental linear oversampling ratio was much higher than 2, our collaborators were able to bin the data together, and reduce the linear oversampling ratio by a factor of 3. This reduction simultaneously eases the spectral bandwidth requirement, and the claimed resolution appears reasonable.

Several small white blotches appear on the foil in the reconstructed image that do not appear in the SEM image. Clearly, the feature in the lower left hand corner of the aperture appears in both images, but I think it is interesting to speculate on the nature of the other discrepant features. The mysterious features could be artifacts of the reconstruction. However, we note that where the torn piece has folded back on itself (near the blue line) the contrast in the reconstructed image consequently changes. It would appear we did not coat enough gold to make the foil completely opaque, which is not surprising considering that we merely timed our sputtering process and assumed a certain deposition rate. Moreover, quoting the manufacturer's website,"In the final stage of the production process of QUANTIFOIL® holey film, carbon is evaporated onto a plastic holey film, and the plastic is dissolved. The grids are washed with chloroform, ethylacetat and aceton. However, not all plastic can be removed. Therefore, the final thickness of the foil is about 20 nm, although only 10 nm of carbon is evaporated onto

the plastic. [95]" So, the discrepant features may in fact be blobs of plastic not evenly washed away in the manufacture of the foil, or perhaps specks of dust. Unfortunately, the SEM does not have the depth of field to focus through the backside of the aperture and image the plastic side of the film. We also do not wish to detach this delicate sample. However, we should look at some other grids to at least confirm this possibility.

One final quality of the reconstructed image worthy of note is its depth of field. Considering that the foil sits many microns above the aperture, but the aperture outline can be seen sharply in the reconstructed image, the foil and aperture together can be thought of as a 'thick' sample. However, in the SEM image the aperture is quite blurry when the foil is in focus.

6.5 Light-Tightness with Thin Metal Filters

6.5.1 Thin Metal Filters for Separating Pump and EUV

Using some typical values, it becomes apparent that massive extinction ratios are required to maintain good signal to noise ratios on the CCD detector. The typical parameters for the ultrafast amplified laser driving the harmonic generation process are a 4.25 W average power running at 3 kHz repetition rate with a center wavelength of around 780 nm. So, the laser produces about 1.4 mJ per pulse, equating to approximately $8.8\text{x}10^{15}$ photons per pulse at 1.59 eV per photon. Or equivalently, $2.6\text{x}10^{19}$ photons per second.

The highest spatial frequency diffraction information of the data sets will appear at the highest diffraction angles and tends to have the weakest diffraction efficiency. Therefore, long integration times are necessary to capture this information, typically 2 hours. During such an exposure, the dark count background will be on the order of 100 counts, while the weakest diffraction speckles may only be 50 counts above this background. Considering the quantum efficiency of the CCD chip, and the gain of

the readout electronics, an approximately one-to-one correspondence exists between impinging *visible* photons and the associated counts registered by the CCD camera. 50 visible photons on each pixel will be enough to wash out the highest spatial frequency information. A less than 50 count noise background from visible photons across the 2048x2048 pixel camera in a 2 hour exposure requires an extinction ratio of 1 part in 10^{15}!

To achieve this feat, thin metal foils are used to filter the 780 nm driving laser light from the generated EUV light. The idea of using thin metal foils as EUV filters was first explored in the 1960's as part of the space program [97]. The basic techniques for making unbacked metal foils in the several hundred nanometer thickness range were initially developed to be used for EUV spectroscopy experiments [98] [99]. Presently, these foils are produced commercially and can be purchased in a variety of materials, thicknesses, geometries, and backings. The filters in this work are unbacked 200 nm thick aluminum mounted on a metal annulus. Thin foils of aluminum are particularly well suited for removing amplified ultrafast laser light from EUV at 29 nm. At 780 nm, Al has an extinction coefficient of 8.597 [42]. Accordingly, after going through 400 nm of Al, the intensity of 780 nm light should drop by a factor $8.7\text{x}10^{-25}$. Yet, 400 nm of Al has a transmission of around 40% for 29 nm EUV light. In addition, aluminum is quite resistant to thermal damage when placed in an intense ultrashort laser beam due to its high reflectance in the near IR and its high thermal conductivity. A single 400 nm Aluminum foil appears to be an ideal solution to the filtering needs of the experiment.

Unfortunately, major issues complicate the use of thin metal foils for filtering. The foils are extraordinarily delicate since they must be thin enough to efficiently transmit the EUV. Foils can be made more mechanically stable by using a supporting grid structure, but this added support cannot be used when mode quality of the EUV beam must be preserved. Pinholes pose another difficulty, as they are a nearly unavoidable property of thin metal films and compromise the light rejecting properties of the film [100]. More-

over, the high absorption of EUV in atmosphere requires experiments to be conducted under vacuum, so the films must survive the viscous forces applied during pumping and venting of the experiment.

Clearly, the proper choice of filter geometry and an inventive holding arrangement becomes necessary with the enormous extinction ratios needed for successful lensless imaging with HHG. The issues caused by pinholes can generally be avoided by using two thin filters, rather than a single filter of the necessary thickness. Pinholes form in random locations, so the chances of two pinholes in separate filters lining up are small. If the filters are placed sufficiently close to one another (usually several cm), unwanted light transmitted through the first filter's pinholes will not have a chance to diverge enough to be transmitted through the second filter. To ensure light-tightness, stray visible light cannot be allowed to find a reflected path around the fixture used to hold the filter. Unfortunately, a perfectly light-tight fixture is seemingly also gas-tight, so during pump-out and venting large viscous flow forces threaten to destroy the filter unless pressures on both its faces are well balanced. Two specialized fixtures were developed in association with the imaging work presented here to overcome the challenges intrinsic to holding EUV filters in a light-tight manner: a baffle, and an in-vacuum filter wheel.

6.5.2 NW-40 Baffle Design

The need for an inventive 'baffle' design for holding EUV filters was first suggested to me by Randy Bartels, and the design described here was prototyped by myself with invaluable guidance from Todd Asnicar of the JILA instrument shop. By a baffle, I mean an arrangement whereby gas but not light can efficiently bypass the filter. The general design philosophy of this sort of baffle involves a convoluted, yet high conductance, pumping path around the filters that guarantees that any stray light attempting to circumvent the filters will undergo many diffuse reflections from an absorptive material.

The baffle holds two EUV filters and consists of an insert, a housing, and threaded retaining rings for securely holding the filters. Figure 6.11 shows a 3-d rendering of the baffle parts and their relative positions when assembled. The central portion of the housing forms an NW-40 centering ring holder, so that the baffle may be inserted between two standard NW-40 flanges. As can be seen in Figure 6.11, the insert and the housing each have four large pumping holes. Each pair of 180° opposed pumping holes in the insert is rotationally offset by 90° from the corresponding pair of holes in the housing, and the two pairs of holes in each piece are rotationally offset by 90° from each other. The insert is cemented with epoxy into the housing, and the insert ends form a seating surface for the filters. The filters are held in place by coarsely threaded retaining rings which mate with the housing (the coarse threading of the retaining rings avoids stripping of the threads).

All pieces of the baffle are made from aluminum and then anodized black to increase absorption. Furthermore, the inner and outer surfaces of the insert, as well as the inner surface of the housing are bead blasted before anodizing to increase scattering of incident light. Stainless steel wool is placed between the insert and housing to further increase diffuse scattering of any stray light while maintaining high conductance. For light to go around the filters it must enter one of the housing pump holes, reflect around to the corresponding insert pump hole, reflect off the inner insert walls to the second set of insert pump holes, and then reflect around to the second set of housing pump holes while avoiding scattering from the steel wool in the process.

Overall, this design effectively eliminates stray visible light while allowing filters to survive viscous forces during pumping. However, several aspects of the design limit its utility. The large surface area of anodized aluminum (which is quite porous and absorbs water vapor when at atmosphere) increases pump out times as well as limiting the ultimate pressure of the vacuum system in which the baffle is placed. Since the filters are always in the pumping path of the vacuum, they remain susceptible to mechanical

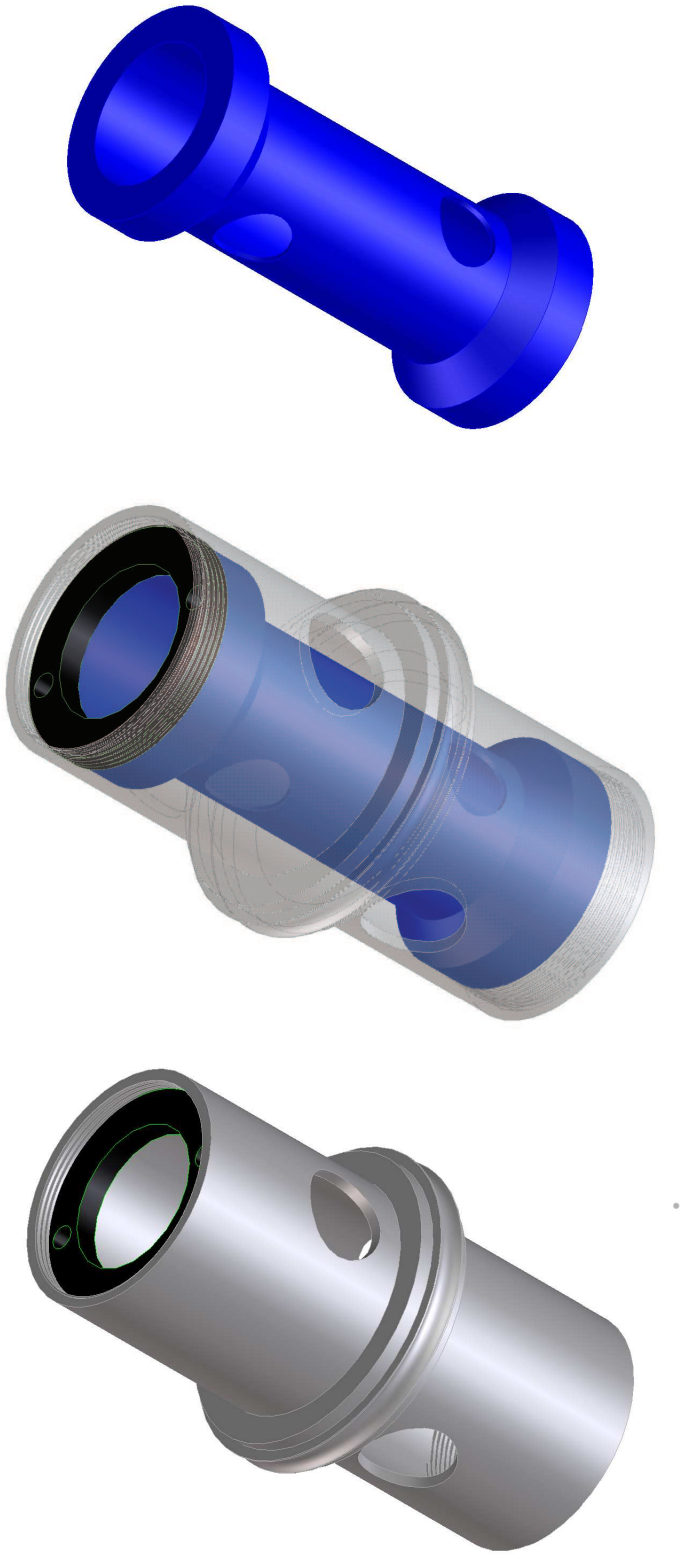

Figure 6.11: Schematic diagram of the NW-40 Baffle

damage. In addition, if either filter becomes compromised, the entire apparatus must be removed from the vacuum system.

6.5.3 Magnetically-Coupled Vacuum-Compatible Filter Wheel

The idea for the unique and novel filter wheel described here was initially suggested by my advisor Henry Kapteyn. The execution of the design was a joint effort between myself and Tracy Keep of the JILA instrument shop. The original motivation for this apparatus stemmed from the desire to study and optimize HHG at various wavelength regions within the EUV spectrum. To efficiently access these different wavelengths, several different filter materials must be used to optimize EUV transmission. Furthermore, filters with sharp transmission "edges" in the wavelength regime of interest act as calibration standards for EUV spectroscopy. The ideal experimental setup allows filter sets to be interchanged and calibration filters to be inserted without dismantling the vacuum system.

Figure 6.12 shows a 3-d rendering of the filter wheel in both an exploded and a fully assembled configuration. The key design elements incorporated in the wheel include a magnetic rotational coupling, a light tight seal, NW-40 flange connections, a "safe" position, an inspection window, and a low profile in the EUV beam propagation direction. A brass ring seated on the exterior of the wheel housing holds six rare earth magnets that couple to the internal filter wheel, allowing the filter wheel to be turned without the use of a dynamic vacuum sealing o-ring. To further improve vacuum performance, the interior of these wheels contains no anodized material, although the outside is anodized for laser safety and durability concerns. Detents in the wheel housing ensure proper positioning of the internal wheel, while the inspection window provides a visual check of both wheel position and filter integrity. The wheels hold three filters each and have a large high conductance aperture that serves as the "safe" position during evacuation and venting of the vacuum system. When the experiment is left idle

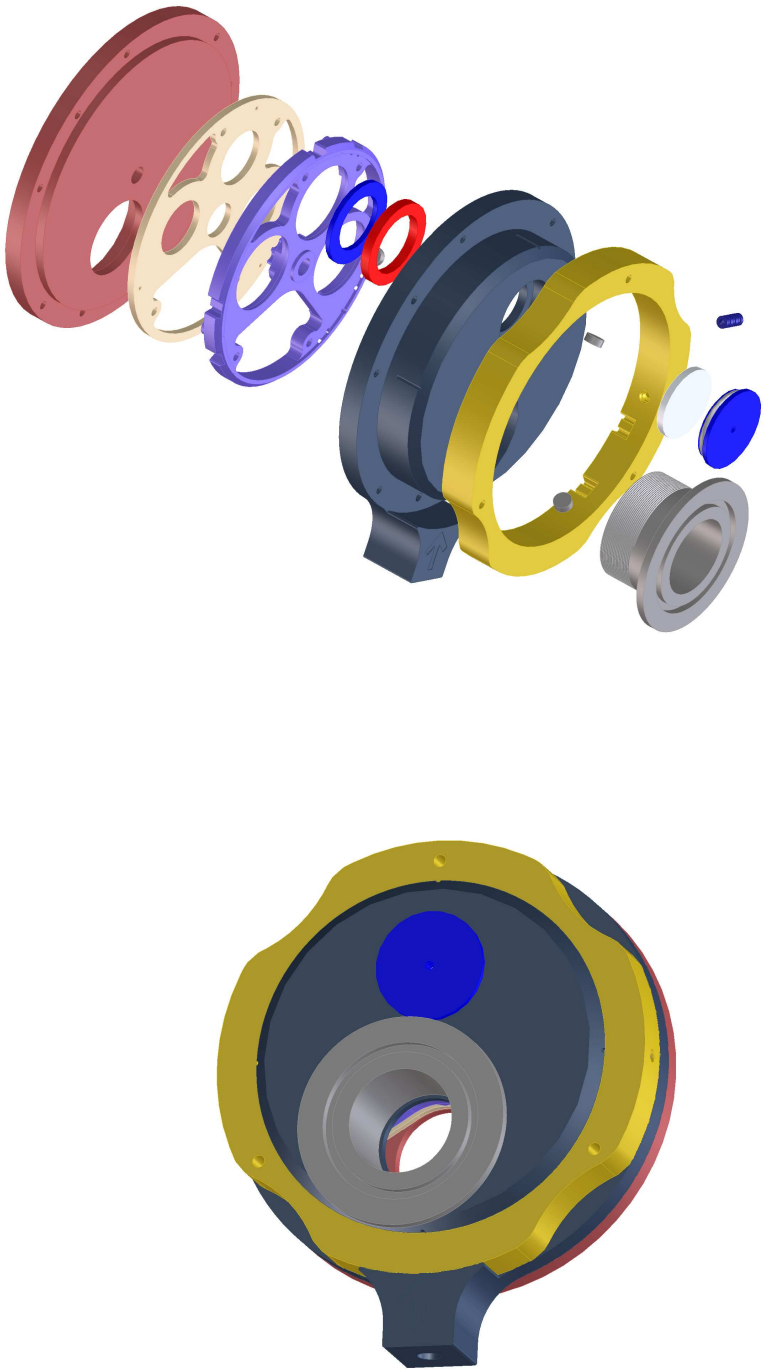

Figure 6.12: 3-dimensional renderings of an exploded and assembled vacuum-compatible filter wheel

under vacuum, the wheel is placed in this safe position to avoid filter damage due to unintentional venting (power outages, mechanical failures, operator error). The low profile of the design also accommodates the close stacking of several wheels, providing the ability to have many filter combinations available in a compact geometry. The wheel itself bears against an internal o-ring that forms a light-tight seal when a filter is rotated in place in front of it. During exposures times exceeding 2 hours using one of these devices, no detectable visible light 'bleed-through' has occurred. I should note that nearly every EUV experiment in the Kapteyn/Murnane group currently employs one or more of these filter wheels.

6.6 Future Directions

6.6.1 Improving Resolution

Three approaches are possible for further improving the ultimate resolution of the microscope. First, if a larger detector were used, higher spatial frequencies could be captured while maintaining the oversampling ratio. Equivalently, a CCD camera with a smaller pixel size could be used, and the sample to CCD distance reduced. Second, the effective spectral bandwidth of the source could be improved using either narrower band mirrors or by narrowing the individual harmonic peaks. Third, shorter wavelength HHG light could be used. Techniques for quasi phase matching, and selective enhancement of a single harmonic order, have recently been demonstrated that allow for the efficient generation of shorter wavelength harmonics. These techniques also accomplish spectral selectivity that reduces the need for filtering, and thus can increase the throughput of the condenser optics [33, 37]. These improvements are quite feasible, and should increase the ultimate resolution to 10's of nm. As the laser repetition rates are increased from 3 kHz to tens of kHz, the EUV flux will be simultaneously increased, and image acquisition time will be dramatically reduced from hours to minutes. Furthermore, as

computing power increases reconstruction times will subsequently shrink, making the lensless technique more accesible.

Given a bright coherent source in the 'water window' and appropriate multilayer mirrors, the set up described above could immediately begin producing reconstructible data. The multilayer mirror technology presently exists, with the possibility of narrow-band mirrors with over 30% reflectivity [101]. Of course, smaller samples, with a more tightly focused illuminating beam, would need to be used to maintain the far field condition and the proper oversampling ratio. The extraordinary time resolution afforded by high harmonics also leaves open the tantalizing possibility of tabletop time-resolved imaging on femtosecond timescales. So, a tabletop EUV and even a soft x-ray lensless microscope is likely to become increasingly practical and has wonderful possibilities for use in metrology in support of next-generation lithographies, nanoscience, biological imaging and perhaps even dynamics studies.

Chapter 7

Conclusion

In conclusion, my thesis reports on two major achievements. The first, in the field of nonlinear optics, involved ground-breaking work that extended traditional nonlinear optics techniques for quasi-phase matching to the extreme realm of HHG. This work not only extended the range over which efficient HHG could take place, but demonstrated the feasibility of modulating the driving light field as a QPM mechanism. Since my work done with modulated waveguides, several other techniques based on similar ideas have shown impressive enhancement factors [33, 46]. The second achievement is the construction and demonstration of the world's first tabletop lensless diffractive microscope using coherent EUV light from high harmonics as an illumination source. This microscope showed a resolution of ~ 200 nm, and already competes with the resolution available from zone-plate microscopy with HHG sources.

Additionally, this thesis describes several original scientific devices that are both novel and elegant. To the best of my knowledge, the custom glass-blowing apparatus is a one-of-a-kind device. Furthermore, the vacuum-compatible filter wheel and the v-groove fixture are examples of enabling technologies, without which, the achievable quality of our lensless microscope would be severely compromised.

As amplified ultrafast lasers are pushed to higher repetition rates, and the efficiency of HHG sources continues to improve at shorter wavelengths, using techniques directly influenced by my work, the practicality of a tabletop EUV lensless microscope

with sub-100 nm resolution for the biological and material sciences will increase dramatically. Such a microscope promises to have broad applications, and should fuel advancements in technology, fundamental understanding of the microscopic world, and perhaps even unlock some of the mysteries of how life develops.

Bibliography

[1] A. Paul, R. Bartels, R. Tobey, H. Green, S. Weiman, I. Christov, M. Murnane, H. Kapteyn, and S. Backus, "Quasi-phase-matched generation of coherent extreme-ultraviolet light," Nature, vol. 421, no. 6918, pp. 51–54, 2003.

[2] T. H. Maiman, "Stimulated optical radiation in ruby," Nature, vol. 187, no. 4736, pp. 493–494, 1960.

[3] S. Backus, C. G. Durfee III, M. M. Murnane, and H. C. Kapteyn, "High power ultrafast lasers," Review of Scientific Instruments, vol. 69, no. 3, p. 1207, 1998.

[4] D. Strickland and G. Mourou, "Compression of amplified chirped optical pulses," Optics Communications, vol. 56, no. 3, pp. 219–221, 1985.

[5] D. M. Gaudiosi, A. L. Lytle, P. Kohl, M. M. Murnane, H. C. Kapteyn, and S. Backus, "11-w average power ti: sapphire amplifier system using downchirped pulse amplification," Optics Letters, vol. 29, no. 22, pp. 2665–2667, 2004.

[6] H. C. Kapteyn, M. M. Murnane, and I. P. Christov, "Extreme nonlinear optics: Coherent x-rays from lasers," Physics Today, vol. 58, no. 3, pp. 39–44, 2005.

[7] R. D. Guenther, "Modern optics," New York: Wiley, 1990, pp. 633–667, 1990.

[8] P. Corkum, "Plasma perspective on strong-field multiphoton ionization," Physical Review Letters, vol. 71, no. 13, pp. 1994–1997, 1993.

[9] J. L. Krause, K. J. Schafer, and K. C. Kulander, "High-order harmonic generation from atoms and ions in the high intensity regime," Physical Review Letters, vol. 68, no. 24, pp. 3535–3538, 1992.

[10] M. V. Ammosov, N. B. Delone, and V. P. Krainov, "Tunnel ionization of complex atoms and of atomic ions in an alternating electromagnetic field," Sov. Phys. JETP, vol. 64, no. 6, pp. 1191–1194, 1986.

[11] A. R. Rundquist, "Phase-matched generation of coherent, ultrafast x-rays using high harmonics," Ph.D. dissertation, Washington State University, 1998.

[12] P. A. Franken, A. E. Hill, C. W. Peters, and G. Weinreich, "Generation of optical harmonics," Physical Review Letters, vol. 7, no. 4, pp. 118–119, 1961.

[13] M. M. Fejer, G. A. Magel, D. H. Jundt, and R. L. Byer, "Quasi-phase-matched second harmonic generation-tuning and tolerances," IEEE Journal of Quantum Electronics, vol. 28, no. 11, pp. 2631–2654, 1992.

[14] A. L'Huillier, X. F. Li, and L. A. Lompre, "Propagation effects in high-order harmonic generation in rare gases," Optical Society of America, Journal, B: Optical Physics, vol. 7, pp. 527–536, 1990.

[15] A. Rundquist, C. G. Durfee 3rd, Z. Chang, C. Herne, S. Backus, M. M. Murnane, and H. C. Kapteyn, "Phase-matched generation of coherent soft x-rays," Science, vol. 280, no. 5368, pp. 1412–5, 1998.

[16] C. G. Durfee III, A. R. Rundquist, S. Backus, C. Herne, M. M. Murnane, and H. C. Kapteyn, "Phase matching of high-order harmonics in hollow waveguides," Physical Review Letters, vol. 83, no. 11, pp. 2187–2190, 1999.

[17] G. R. Fowles, Introduction to Modern Optics. New York: Dover Publications, 1989.

[18] J. A. Armstrong, N. Bloembergen, J. Ducuing, and P. S. Pershan, "Interactions between light waves in a nonlinear dielectric," Physical Review, vol. 127, no. 6, pp. 1918–1939, 1962.

[19] P. A. Franken and J. F. Ward, "Optical harmonics and nonlinear phenomena," Reviews of Modern Physics, vol. 35, no. 1, pp. 23–39, 1963.

[20] D. Feng, N. B. Ming, J. F. Hong, Y. S. Yang, J. S. Zhu, Z. Yang, and Y. N. Wang, "Enhancement of second-harmonic generation in linbo crystals with periodic laminar ferroelectric domains," Applied Physics Letters, vol. 37, p. 607, 1980.

[21] I. Christov, H. Kapteyn, and M. Murnane, "Quasi-phase matching of high-harmonics and attosecond pulses in modulated waveguides," Optics Express, vol. 7, no. 11, pp. 362–367, 2000.

[22] I. P. Christov, "Control of high harmonic and attosecond pulse generation in aperiodic modulated waveguides," J. Opt. Soc. Am. B, vol. 18, pp. 1877–1881, 2001.

[23] A. Paul, E. A. Gibson, X. Zhang, A. Lytle, T. Popmintchev, X. Zhou, M. M. Murnane, I. P. Christov, and H. C. Kapteyn, "Phase-matching techniques for coherent soft x-ray generation: Extreme ultraviolet coherent sources and applications," IEEE Journal of Quantum Electronics, vol. 42, no. 1-2, pp. 14–26, 2006.

[24] C. Spielmann, "Generation of coherent x-rays in the water window using 5-femtosecond laser pulses," Science, vol. 278, no. 5338, pp. 661–664, 1997.

[25] Z. Chang, A. Rundquist, H. Wang, M. M. Murnane, and H. C. Kapteyn, "Generation of coherent soft x rays at 2.7 nm using high harmonics," Physical Review Letters, vol. 79, no. 16, pp. 2967–2970, 1997.

[26] J. Seres, P. Wobrauschek, C. Streli, V. S. Yakovlev, E. Seres, F. Krausz, and C. Spielmann, "Generation of coherent kev x-rays with intense femtosecond laser pulses," New Journal of Physics, vol. 8, p. 251, 2006.

[27] S. Backus, R. Bartels, S. Thompson, R. Dollinger, H. C. Kapteyn, and M. M. Murnane, "High-efficiency, single-stage 7-khz high-average-power ultrafast laser system," Opt. Lett, vol. 26, pp. 465–467, 2001.

[28] P. L. Shkolnikov, A. Lago, and A. E. Kaplan, "Optimal quasi-phase-matching for high-order harmonic generation in gases and plasma," Physical Review A, vol. 50, no. 6, pp. 4461–4464, 1994.

[29] H. R. Lange, A. Chiron, J. F. Ripoche, A. Mysyrowicz, P. Breger, and P. Agostini, "High-order harmonic generation and quasiphase matching in xenon using self-guided femtosecond pulses," Physical Review Letters, vol. 81, no. 8, pp. 1611–1613, 1998.

[30] L. Misoguti, S. Backus, C. G. Durfee, R. Bartels, M. M. Murnane, and H. C. Kapteyn, "Generation of broadband vuv light using third-order cascaded processes," Physical Review Letters, vol. 87, no. 1, p. 13601, 2001.

[31] S. L. Voronov, I. Kohl, J. B. Madsen, J. Simmons, N. Terry, J. Titensor, Q. Wang, and J. Peatross, "Control of laser high-harmonic generation with counterpropagating light," Physical Review Letters, vol. 87, no. 13, p. 133902, 2001.

[32] A. L. Lytle, X. Zhang, J. Peatross, M. M. Murnane, H. C. Kapteyn, and O. Cohen, "Probe of high-order harmonic generation in a hollow waveguide geometry using counterpropagating light," Physical Review Letters, vol. 98, no. 12, p. 123904, 2007.

[33] X. Zhang, A. L. Lytle, T. Popmintchev, X. Zhou, H. C. Kapteyn, M. M. Murnane, and O. Cohen, "Quasi-phase-matching and quantum-path control of high-harmonic generation using counterpropagating light," Nature Physics, vol. 3, pp. 270–275, 2007.

[34] G. D. Miller, R. G. Batchko, W. M. Tulloch, D. R. Weise, M. M. Fejer, and R. L. Byer, "42 percent-efficient single-pass cw second-harmonic generation in periodically poled lithium niobate," Opt. Lett, vol. 22, no. 24, pp. 1834–1836, 1997.

[35] S. Zhu, Y. Zhu, and N. Ming, "Quasi-phase-matched third-harmonic generation in a quasi-periodic optical superlattice," Science, vol. 278, no. 5339, pp. 843–846, 1997.

[36] S. Somekh and A. Yariv, "Phase matching by periodic modulation of the nonlinear optical properties," Optics Communications, vol. 6, no. 3, pp. 301–304, 1972.

[37] R. Bartels, S. Backus, E. Zeek, L. Misoguti, G. Vdovin, I. P. Christov, M. M. Murnane, and H. C. Kapteyn, "Shaped-pulse optimization of coherent emission of high-harmonic soft x-rays," Nature, vol. 406, pp. 164–166, 2000.

[38] B. L. Henke, E. M. Gullikson, and J. C. Davis, "X-ray interactions: photoabsorption, scattering, transmission, and reflection at e= 50-30000 ev, z= 1-92," Atomic Data and Nuclear Data Tables, vol. 54, no. 2, pp. 181–342, 1993.

[39] E. A. Gibson, "Quasi-phase matching of soft x-ray light from high-order harmonic generation using waveguide structures," Ph.D. dissertation, University of Colorado, 2004.

[40] E. A. Gibson, A.Paul, N. Wagner, R. Tobey, D. Gaudiosi, S. Backus, I. P. Christov, A. Aquila, E. M. Gullikson, D. T. Attwood, M. M. Murnane, and H. C. Kapteyn, "Coherent soft x-ray generation in the water window with quasi-phase matching," Science, vol. 302, no. 5642, pp. 95–98, 2003.

[41] E. A. Gibson, A. Paul, N. Wagner, R. Tobey, S. Backus, I. P. Christov, M. M. Murnane, and H. C. Kapteyn, "High-order harmonic generation up to 250 ev from highly ionized argon," Physical Review Letters, vol. 92, no. 3, p. 33001, 2004.

[42] R. C. Weast, Ed., CRC Handbook of Chemistry and Physics [M]. Florida: CRC Press Inc, 1985, vol. 66th Edition.

[43] T. E. Dimmick, G. Kakarantzas, T. A. Birks, and P. S. J. Russell, "Carbon dioxide laser fabrication of fused-fiber couplers and tapers," Appl. Opt, vol. 38, no. 33, p. 68456848, 1999.

[44] A. J. C. Grellier, N. K. Zayer, and C. N. Pannell, "Heat transfer modelling in co2 laser processing of optical fibres," Optics Communications, vol. 152, no. 4, pp. 324–328, 1998.

[45] Y. S. Touloukian and C. Y. Ho, Thermophysical properties of matter-the TPRC data series. Volume 14. Master index-to materials and properties. Lafayette, IN: Purdue Univ., Thermophysical and Electronic Properties Information Center, 1979.

[46] M. Zepf, B. Dromey, M. Landreman, P. Foster, and S. M. Hooker, "Bright quasi-phasematched soft x-ray harmonic radiation from argon ions," Arxiv preprint physics/0702117, 2007.

[47] B. Dromey, M. Zepf, M. Landreman, and S. M. Hooker, "Quasi-phasematching of harmonic generation via multimode beating in waveguides," Arxiv preprint physics/0702116, 2007.

[48] J. D. Jackson, Classical Electrodynamics, ser. Classical Electrodynamics, 3rd Edition, by John David Jackson. New York: John Wiley & Sons, Inc., 1999.

[49] M. Nisoli, S. Stagira, S. De Silvestri, O. Svelto, S. Sartania, Z. Cheng, M. Lenzner, C. Spielmann, and F. Krausz, "A novel-high energy pulse compression system: generation of multigigawatt sub-5-fs pulses," Applied Physics B: Lasers and Optics, vol. 65, no. 2, pp. 189–196, 1997.

[50] E. A. J. Marcatili and R. A. Schmeltzer, "Hollow metallic and dielectric waveguides for long distance optical transmission and lasers," Bell System Technical Journal, vol. 43, pp. 1783–1809, 1964.

[51] R. Abrams, "Coupling losses in hollow waveguide laser resonators," Quantum Electronics, IEEE Journal of, vol. 8, no. 11, pp. 838–843, 1972.

[52] T. Pfeifer and M. C. Downer, "Direct experimental observation of periodic intensity modulation along straight hollow core optical waveguides," Arxiv preprint physics/0609080, 2006.

[53] N. L. Wagner, E. A. Gibson, T. Popmintchev, I. P. Christov, M. M. Murnane, and H. C. Kapteyn, "Self-compression of ultrashort pulses through ionization-induced spatiotemporal reshaping," Physical Review Letters, vol. 93, no. 17, p. 173902, 2004.

[54] X. Zhang, A. Lytle, T. Popmintchev, A. Paul, N. Wagner, M. Murnane, H. Kapteyn, and I. P. Christov, "Phase matching, quasi-phase matching, and pulse compression in a single waveguide for enhanced high-harmonic generation," Optics Letters, vol. 30, no. 15, pp. 1971–1973, 2005.

[55] R. A. Bartels, A. Paul, H. Green, H. C. Kapteyn, M. M. Murnane, S. Backus, I. P. Christov, Y. Liu, D. T. Attwood, and C. Jacobsen, "Fully spatially coherent euv beams generated using a small-scale laser," Science, vol. 297, p. 376378, 2002.

[56] S. M. Hurtley and L. Helmuth, "The future looks bright," Science, vol. 300, no. 5616, p. 75, 2003.

[57] J. C. H. Spence, High-Resolution Electron Microscopy, 3rd ed. New York: Oxford University Press, 2003.

[58] C. Jacobsen, "Soft x-ray microscopy," Trends in Cell Biology, vol. 9, p. 4447, 1999.

[59] J. Kirz, C. Jacobsen, and M. Howells, "Soft x-ray microscopes and their biological applications," Q. Rev. Biophys, vol. 28, no. 1, pp. 33–130, 1995.

[60] D. T. Attwood, Soft x-rays and extreme ultraviolet radiation. New York: Cambridge University Press, 2000.

[61] C. A. Larabell and M. A. Le Gros, "X-ray tomography generates 3-d reconstructions of the yeast, saccharomyces cerevisiae, at 60-nm resolution," Molecular Biology of the Cell, vol. 15, no. 3, pp. 957–962, 2004.

[62] S. Eisebitt, J. Luening, W. F. Schlotter, M. Loergen, O. Hellwig, W. Eberhardt, and J. Stoehr, "Lensless imaging of magnetic nanostructures by x-ray spectroholography," Nature, vol. 432, no. 7019, pp. 885–888, 2004.

[63] P. Fischer, D. H. Kim, W. Chao, J. A. Liddle, E. H. Anderson, and D. T. Attwood, "Soft x-ray microscopy of nanomagnetism," Materials Today, vol. 9, p. 26, 2006.

[64] D. Sayre, J. Kirz, R. Feder, D. M. Kim, and E. Spiller, "Transmission microscropy of unmodified biological materials: comparative radiation dosages with electrons and ultrasoft x-ray photons," Ultramicroscopy, vol. 2, no. 4, pp. 337–49, 1977.

[65] M. Spencer, Fundamentals of Light Microscopy. Cambridge University Press, 1982.

[66] X. Zhang, A. R. Libertun, A. Paul, E. Gagnon, S. Backus, I. P. Christov, M. M. Murnane, H. C. Kapteyn, R. A. Bartels, and Y. Liu, "Highly coherent light at 13 nm generated by use of quasi-phase-matched high-harmonic generation," Optics Letters, vol. 29, no. 12, pp. 1357–1359, 2004.

[67] J. W. Goodman, Introduction to Fourier Optics, Second Edition. Boston: McGraw Hill, 1996.

[68] D. B. Murphy, R. Hoffman, K. R. Spring, and M. W. Davidson, "Specimen contrast in optical microscopy." [Online]. Available: http://www.microscopyu.com/articles/formulas/specimencontrast.html

[69] W. Chao, B. D. Harteneck, J. A. Liddle, E. H. Anderson, and D. T. Attwood, "Soft x-ray microscopy at a spatial resolution better than 15 nm," Nature, vol. 435, no. 7046, pp. 1210–1213, 2005.

[70] G. Vaschenko, F. Brizuela, C. Brewer, M. Grisham, H. Mancini, C. S. Menoni, M. C. Marconi, J. J. Rocca, W. Chao, and J. A. Liddle, "Nanoimaging with a compact extreme-ultraviolet laser," Optics Letters, vol. 30, no. 16, pp. 2095–2097, 2005.

[71] G. Vaschenko, C. Brewer, F. Brizuela, Y. Wang, M. A. Larotonda, B. M. Luther, M. C. Marconi, J. J. Rocca, C. S. Menoni, and E. H. Anderson, "Sub-38nm resolution tabletop microscopy with 13nm wavelength laser light," Optics Letters, vol. 31, no. 9, pp. 1214–1216, 2006.

[72] M. Wieland, K. U. Spielmann Ch, T. Westerwalbesloh, U. Heinzmann, and T. Wilhein, "Toward time-resolved soft x-ray microscopy using pulsed fs-high-harmonic radiation," Ultramicroscopy, vol. 102, no. 2, pp. 93–100, 2005.

[73] J. E. Trebes, S. B. Brown, E. M. Campbell, D. L. Matthews, D. G. Nilson, G. F. Stone, and D. A. Whelan, "Demonstration of x-ray holography with an x-ray laser," Science, vol. 238, no. 4826, p. 517, 1987.

[74] D. Gabor, "A new microscopic principle," Nature, vol. 161, no. 4098, pp. 777–778, 1948.

[75] ——, "Microscopy by reconstructed wave-fronts," Proceedings of the Royal Society of London. Series A, Mathematical and Physical Sciences, vol. 197, no. 1051, pp. 454–487, 1949.

[76] I. McNulty, J. Kirz, C. Jacobsen, E. H. Anderson, M. R. Howells, and D. P. Kern, "High-resolution imaging by fourier transform x-ray holography," Science, vol. 256, no. 5059, p. 1009, 1992.

[77] J. Miao, P. Charalambous, J. Kirz, and D. Sayre, "Extending the methodology of x-ray crystallography to allow imaging of micrometre-sized non-crystalline specimens," Nature, vol. 400, no. 6742, p. 342, 1999.

[78] M. A. Pfeifer, G. J. Williams, I. A. Vartanyants, R. Harder, and I. K. Robinson, "Three-dimensional mapping of a deformation field inside a nanocrystal," Nature, vol. 442, no. 7098, pp. 63–66, 2006.

[79] H. M. Quiney, A. G. Peele, Z. Cai, D. Paterson, and K. A. Nugent, "Diffractive imaging of highly focused x-ray fields," Nature Physics, vol. 2, no. 2, pp. 101–104, 2006.

[80] X. Xiao and Q. Shen, "Wave propagation and phase retrieval in fresnel diffraction by a distorted-object approach," Physical Review B, vol. 72, no. 3, p. 33103, 2005.

[81] D. Shapiro, P. Thibault, T. Beetz, V. Elser, M. Howells, C. Jacobsen, J. Kirz, E. Lima, H. Miao, and A. M. Neiman, "Biological imaging by soft x-ray diffraction microscopy," Proceedings of the National Academy of Sciences, vol. 102, no. 43, pp. 15 343–15 346, 2005.

[82] H. N. Chapman, A. Barty, S. Marchesini, A. Noy, S. P. Hau-Riege, C. Cui, M. R. Howells, R. Rosen, H. He, and J. C. H. Spence, "High-resolution ab initio three-dimensional x-ray diffraction microscopy," Journal of the Optical Society of America A, vol. 23, no. 5, pp. 1179–1200, 2006.

[83] H. N. Chapman, A. Barty, M. J. Bogan, S. Boutet, M. Frank, S. P. Hau-Riege, S. Marchesini, B. W. Woods, S. Bajt, and W. H. Benner, "Femtosecond diffractive imaging with a soft-x-ray free-electron laser," Nature Physics, vol. 2, 2006.

[84] J. Miao and D. Sayre, "On possible extensions of x-ray crystallography through diffraction-pattern oversampling," Acta crystallographica. Section A, Foundations of crystallography, vol. 56, no. 6, pp. 596–605, 2000.

[85] J. R. Fienup, "Phase retrieval algorithms: a comparison," Applied Optics, vol. 21, no. 15, pp. 2758–2769, 1982.

[86] J. Miao, T. Ishikawa, E. H. Anderson, and K. O. Hodgson, "Phase retrieval of diffraction patterns from noncrystalline samples using the oversampling method," Physical Review B, vol. 67, no. 17, p. 174104, 2003.

[87] D. Sayre, "Some implications of a theorem due to shannon," Acta Crystallographica, vol. 5, no. 6, pp. 843–843, 1952.

[88] J. Miao, H. N. Chapman, J. Kirz, D. Sayre, and K. O. Hodgson, "Taking x-ray diffraction to the limit: Macromolecular structures from femtosecond x-ray pulses and diffraction microscopy of cells with synchrotron radiation," Annual Review of Biophysics and Biomolecular Structure, vol. 33, no. 1, pp. 157–176, 2004.

[89] J. Miao, D. Sayre, and H. N. Chapman, "Phase retrieval from the magnitude of the fourier transforms of nonperiodic objects," Journal of the Optical Society of America A, vol. 15, no. 6, pp. 1662–1669, 1998.

[90] J. R. Fienup, "Reconstruction of an object from the modulus of its fourier transform," Opt. Lett, vol. 3, no. 1, pp. 27–29, 1978.

[91] A. R. Libertun, X. Zhang, A. Paul, E. Gagnon, T. Popmintchev, S. Backus, M. M. Murnane, H. C. Kapteyn, and I. P. Christov, "Design of fully spatially coherent extreme-ultraviolet light sources," Applied Physics Letters, vol. 84, no. 19, pp. 3903–3905, 2004.

[92] P. W. Wachulak, R. A. Bartels, M. C. Marconi, C. S. Menoni, J. J. Rocca, Y. Lu, and B. Parkinson, "Sub 400 nm spatial resolution extreme ultraviolet holography with a table top laser," Optics Express, vol. 14, no. 21, pp. 9636–9642, 2006.

[93] F. R. Powell, J. F. Lindblom, S. F. Powell, and P. W. Vedder, "Thin film filter performance for extreme ultraviolet and x-ray applications," Optical Engineering, vol. 29, p. 614, 1990.

[94] M. D. Simon, L. O. Heflinger, and A. K. Geim, "Diamagnetically stabilized magnet levitation," American Journal of Physics, vol. 69, p. 702, 2001.

[95] "Quantifoil®holey carbon films." [Online]. Available: http://www.quanitfoil.com

[96] M. Roth, J. Roslund, and H. Rabitz, "Assessing and managing laser system stability for quantum control experiments," Review of Scientific Instruments, vol. 77, p. 083107, 2006.

[97] W. R. Hunter, D. W. Angel, and R. Tousey, "Thin films and their uses for the extreme ultraviolet," Appl. Opt, vol. 4, p. 891898, 1965.

[98] G. N. Steele, "Development and fabrication of large-area extreme-ultraviolet filters for the apollo telescope mount," Space Optics, Proceedings, Ninth International Congress of the International Commission for Optics, 1974.

[99] W. R. Hunter, "The preparation and use of unbacked metal films as filters in the extreme ultraviolet," Phys. Thin Films, vol. 7, pp. 43–114, 1973.

[100] W. R. Hunter, J. D. Purcell, and G. N. Steele, "Evaluation of pinholes in unbacked metal film filters to be used in rocket- and satellite-borne xuv spectroheliographs," Applied Optics, vol. 12, no. 8, p. 1874, 1973.

[101] F. Eriksson, G. A. Johansson, H. M. Hertz, E. M. Gullikson, U. Kreissig, and J. Birch, "14.5mirrors for the water window," Optics Letters, vol. 28, no. 24, pp. 2494–2496, 2003.